Zehra DURMUŞ

M.S. Thesis In Chemistry

July 2009

SYNTHESIS AND CHARACTERIZATION OF COATED MAGNETIC SPINEL NANOPARTICLES

by

Zehra DURMUŞ

July 2009

SYNTHESIS AND CHARACTERIZATION OF COATED MAGNETIC SPINEL NANOPARTICLES

by

Zehra Durmuş

A thesis submitted to

the Graduate Institute of Science and Engineering

of

Fatih University

in partial fulfillment of the requirements for the degree of

Master of Science

in

Chemistry

July 2009
Istanbul, Turkey

APPROVAL PAGE

I certify that this thesis satisfies all the requirements as a thesis for the degree of Master of Science.

_____
Assoc. Prof. Metin TÜLÜ
Head of Department

This is to certify that I have read this thesis and that in my opinion it is fully adequate, in scope and quality, as a thesis for the degree of Master of Science.

_____
Assoc. Prof. Abdülhadi BAYKAL
Supervisor

Examining Committee Members

Assoc. Prof. Ayhan BOZKURT _____

Assoc. Prof. Abdülhadi BAYKAL _____

Assoc. Prof. Muhammet S.TOPRAK _____

It is approved that this thesis has been written in compliance with the formatting rules laid down by the Graduate Institute of Sciences and Engineering.

_____
Assoc. Prof. Nurullah ARSLAN
Director

SYNTHESIS AND CHARACTERIZATION OF COATED MAGNETIC SPINEL NANOPARTICLES

Zehra Durmuş

M. S. Thesis - Chemistry
July 2009

Supervisor: Assoc. Prof. Abdülhadi BAYKAL

ABSTRACT

In this thesis, M_3O_4 (M = Fe, Co, Mn) type of coated magnetic spinel nanoparticles (NPs) were synthesized by various solution based processes including hydrothermal, surfactant-assisted (CTAB, TMAOH, PVP, L-lysine, ascorbic acid, salicylic acid, egg white, and alginic acid) hydrothermal, sonochemical, gel-to crystalline, thermal decomposition and co-precipitation methods. Structural, morphological, spectroscopic, magnetic and electrical characterizations of all samples were done using XRD, TEM, SEM, FTIR, EPR, TGA, and conductivity measurements. Crystallite size of the magnetic NPs was determined by Zeta Potential Particle Size Analyzer, XRD (Scherrer equation and line profile fitting route), and TEM micrographs. In addition to TEM analysis, for the morphological investigation of some samples, SEM was also used.

Superparamagnetic iron oxide (Fe_3O_4, magnetite) NPs were synthesized successfully by three different routes. Fe_3O_4 NPs were synthesized by surfactant-assisted hydrothermal route using TMAOH as alkalizing agent and surfactant to prevent the agglomeration. L-lysine, alginic acid and salicylic acid type of surfactants were used for the first time in this study to synthesize the Fe_3O_4 spinel NPs by surfactant assisted-co precipition route. Sonochemical synthesis of magnetite was also performed for the first time in this study without pH adjustment and magnetite (Fe_3O_4) - Poly(1-vinyl-1,2,4-triazole) (PVTri) nanocomposites were prepared with as-synthesized magnetite NPs. The average crystallite size was determined in the range of 8 - 20 nm for all magnetite NPs.

Magnetic Co_3O_4 NPs were synthesized by two different routes. These routes are sol-gel process and surfactant assisted-hydrothermal route which are simple and cost effective. PVP (polyvinylpyrrolidone) as type of surfactant and egg white were used for the first time in

this study to synthesize the Co_3O_4 spinel NPs. By using diffraction profile fitting route, the average crystallite size was calculated in the range of 19 - 45 nm.

Magnetic Mn_3O_4 NPs were synthesized by three different routes. Mn_3O_4 NPs were successfully prepared by a novel ionic liquid assisted route (green chemistry) based on ionic liquid (1-n-butyl- 3-methylimidazolium hydroxide) [BMIM]OH as reaction media. Mn_3O_4 NPs were synthesized by hydrothermal route using TMAOH/NaOH to compare the effect of neutralizing agent, H_2O_2, and PVP respectively. Egg-white (ovalbumin) assisted route was used for the first time in this study to synthesize the Mn_3O_4 spinel NPs. The average crystallite size was determined in the range of 13 -41.5 nm for all Mn_3O_4 NPs.

Keywords: Spinels, Magnetic nanomaterials, AC/DC Conductivity, TEM, EPR**.**

YÜZEYİ KAPLANMIŞ MANYETİK SPİNEL NANOPARÇACIKLARIN SENTEZİ VE KARAKTERİZASYONU

Zehra Durmuş

Yüksek Lisans Tezi - Kimya
Temmuz 2009

Tez yöneticisi: Doç. Dr. Abdülhadi BAYKAL

ÖZ

Bu çalışmada M_3O_4 (M = Fe, Co, Mn) tipi spinel bileşikler hidrotermal, surfaktant (CTAB, TMAOH, PVP, L-lisin, askorbik asit, salisilik asit, yumurta akı ve aljinik asit) yardımıyla hidrotermal, sonokimyasal, yükseltgenme- indirgenme, jel kristal dönüşümü, birlikte çöktürme ve yüksek sıcaklıkta bozunma gibi metodlar kullanılarak sentezlenmiştir. Sentezlenen maddelerin yapısal, morfolojik, spektroskopik ve magnetik karakterizasyonu XRD, TEM, SEM, FTIR, EPR, TGA ve iletkenlik ölçüm metotları kullanılarak analiz edilmiştir. Manyetik nanoparçacıkların kristal boyutu Zeta Potansiyel, XRD (Scherrer denklemi ve profil çizgi eğri uydurma metodu) ve TEM kullanılarak ölçülmüştür. Ek olarak, maddelerin morfolojik özelliklerinin araştırılması için SEM kullanılmıştır.

Süper paramanyetik demir oksit Fe_3O_4 nanoparçacıkları üç farklı metodla başarılı bir şekilde sentezlenmiştir. Fe_3O_4 nanoparçacıkları surfaktant yardımıyla hidrotermal metodla bazikleştirici ve topaklaşma önleyici surfaktant olarak TMAOH kullanılarak sentezlenmiştir. L-lisin, aljinik asit ve salisilik asit tipi surfaktantlar ile Fe_3O_4 spinel nanoparçacık sentezi ilk defa bu çalışmada surfaktant yardımıyla birlikte çöktürme yöntemiyle başarılı bir şekilde gerçekleştirilmiştir. Magnetit nanoparçacıklarının sonokimyasal sentezi yine ilk defa bu çalışmada herhangibir pH ayarlaması yapılmaksızın gerçekleştirilmiş olup sentezlenen demir oksit nanoparçacıkları (Fe_3O_4) – Poliviniltriazol (PVTri) nanokompoziti hazırlamakta kullanılmıştır. Bütün magnetit nanoparçacıkların ortalama kristal boyutu ise 8 - 20 nm olarak belirlenmiştir.

Magnetik Co_3O_4 nanoparçacıkları iki değişik metotla sentezlenmiştir. Bu metotlar jel kristal dönüşümü ve surfaktant yardımıyla hidrotermal metodları olup basit ve düşük maliyetlidirler. PVP (polivinilpirolidon) ve yumurta akı gibi surfaktant malzemeler ilk kez bu çalışmada Co_3O_4 spinel nano malzemelerin sentezinde kullanılmıştır. XRD ve profil çizgi eğri uydurma metodu kullanılarak ortalama kristal boyutu 19 – 45 nm olarak hesaplanmıştır.

Mn_3O_4, nanoparçacıkları üç değişik metotla sentezlenmiştir. İyonik likit (yeşil kimya) metoduna uygun olarak reaksiyon ortamı olarak seçilen [BMIM]OH (1-n-butil- 3-

metilimidazolium hidroksit) iyonik likiti kullanılarak ilk defa bu çalışmada sentezlenmiştir. Mn_3O_4, nanoparçacıkları; TMAOH/NaOH ile nötralleştirme etkisinin karşılaştırması yapılarak, H_2O_2 ile ve surfaktant olarak PVP kullanılarak hidrotermal metotla birbirinden farklı üç örnek olarak sentezlenmiştir. Sonuncu yöntem olarak yumurta akı (ovalbümin) yardımıyla jel kristal dönüşümü metodu ile yine ilk defa bu çalışmada sentezlenmiştir. Bütün Mn_3O_4 nanoparçacıkların ortalama kristal boyutu ise 13 - 41.5 nm olarak belirlenmiştir.

Anahtar Kelimeler: Spinel bileşikler, Manyetik nanoparçacıklar, AC/DC iletkenlik, TEM, EPR.

This dissertation is dedicated to my lovely son

Ahmet Burak

ACKNOWLEDGMENT

I would like to express my sincere gratitude to my advisor, Assoc. Prof. Dr. Abdülhadi BAYKAL, for providing valuable guidance to research and constant supports to my study. I highly appreciate Prof. BAYKAL for introducing me to scientific research, giving me a chance to accelerate my research skills, and encouraging me to work in the field of nanotechnology. His expertise in nanostructured materials along with his vision of nanotechnology has been the source of inspiration to me for further research in the field.

I specially thank to Asst. Prof. Dr. Muhammed S. TOPRAK for his generous assistance and insightful discussions during my study.

I express my thanks to Dr. Hüseyin KAVAS for his helpful assistance and his advices to my research endevaors. In addition his valuable times of consultation and editing that went into the completion of this dissertation were unbelievably helpful.

I am also very grateful to my colleagues Ms. Aslıhan Sezgin, Ms. Ayşe Aslan and Ms. Merve Tomaş. I highly appreciate their friendship and support.

I would like to thank Professors BOZKURT and TOPRAK for serving on my thesis supervisory committee. I am grateful to them for their careful and critical reading of my thesis and invaluable suggestions.

I would also like to thank to The Graduate Institute of Sciences and Engineering of Fatih University for funding my thesis with the AFP contract no: P50020803-2.

I would like to thank my parents for their love, patience and encouragement.

Finally, there can be no adequate acknowledgement for the loving encouragement I have received from my husband Assist. Prof. Dr. Ali Durmuş. Without his constant support and inspiration all this would never have been possible. And of course my little lovely son Ahmet Burak who was together with me during all search period. This dissertation is dedicated to him.

TABLE OF CONTENTS

LIST OF FIGURES

FIGURE

CHAPTER 1

INTRODUCTION

1.1 General Introduction

Nanotechnology is the technology embedded and determined by the world of atoms, molecules, and clusters at the nanometer scale. The nanometer level is already state of the art for in this ultra small world. Because at this scale, materials can behave very differently from when they are in larger form.

In 1959 Laureate Richard P. Feynman, entitled "There's Plenty of Room at the Bottom" [1] presented a vision of extreme miniaturization. A miniaturization that would require the ability to manipulate and control materials on a scale smaller than was ever imagined at that time. Feynman discussed his vision of building objects atom by atom, or molecule by molecule, and with this was born the idea of "nanotechnology." Professor Neal Lane defines nanotechnology as "the ability to manipulate individual atoms and molecules to produce nanostructured materials and sub-micron objects that have applications in the real world" [2].

During the final decade of the 20th century, nanomaterials were the focus of research in the field of materials science, which is driven by the expectations concerning the application of nanomaterials as a forthcoming generation of functional materials for the new century. A large amount of knowledge about the synthesis and properties of various NPs and nanocomposites was accumulated within such a short period, with numerous new insights and techniques emerging with each passing day. The physical and chemical properties of substances can be significantly altered when they are exhibited on a nanometer-length scale, and this phenomenon opens up a completely new perspective for materials design that benefits from the introduction of not only particle size, but also particle morphology as new, powerful parameters [3].

Within the last decade, nanoscience and nanotechnology [4-7] have reached the status of leading sciences with fundamental and applied research in all basic physical, life, and earth

sciences as well as engineering and materials science [8–14]. An important feature of nanoscience is that it bridges the crucial dimensional gap between the atomic and molecular scale of fundamental sciences and the microstructural scale of engineering and manufacturing [15]. Accordingly, a vast amount of true multidisciplinary fundamental knowledge is to be explored and linked [16,17]. It shall lead to a tremendous amount of in-depth understanding as well as to the fabrication of novel high technological devices in many fields of applications from electronics to medicine [18–20]. Therefore, it should improve tremendously the level of technological advance to a much greater rate than human history has ever experienced. As a result, the technological, educational, and societal implications of nanoscience [21] and nanotechnology are of immense importance, which are attested to by the tremendous interests, the major economic efforts, and the national initiatives of many countries around the world [22].

1.2 General Background of Nanomaterials

The substances with at least in the size region of one dimension **1–100 nm** can be called **nanoscale** substances. A nanometre (nm) is one thousand millionth of a meter. If it has to be compared, a single human hair is about 50,000 nm wide, a red blood cell is approximately 5,000 nm wide and a DNA molecule is almost 2.5 nm across (Fig. 1.1).

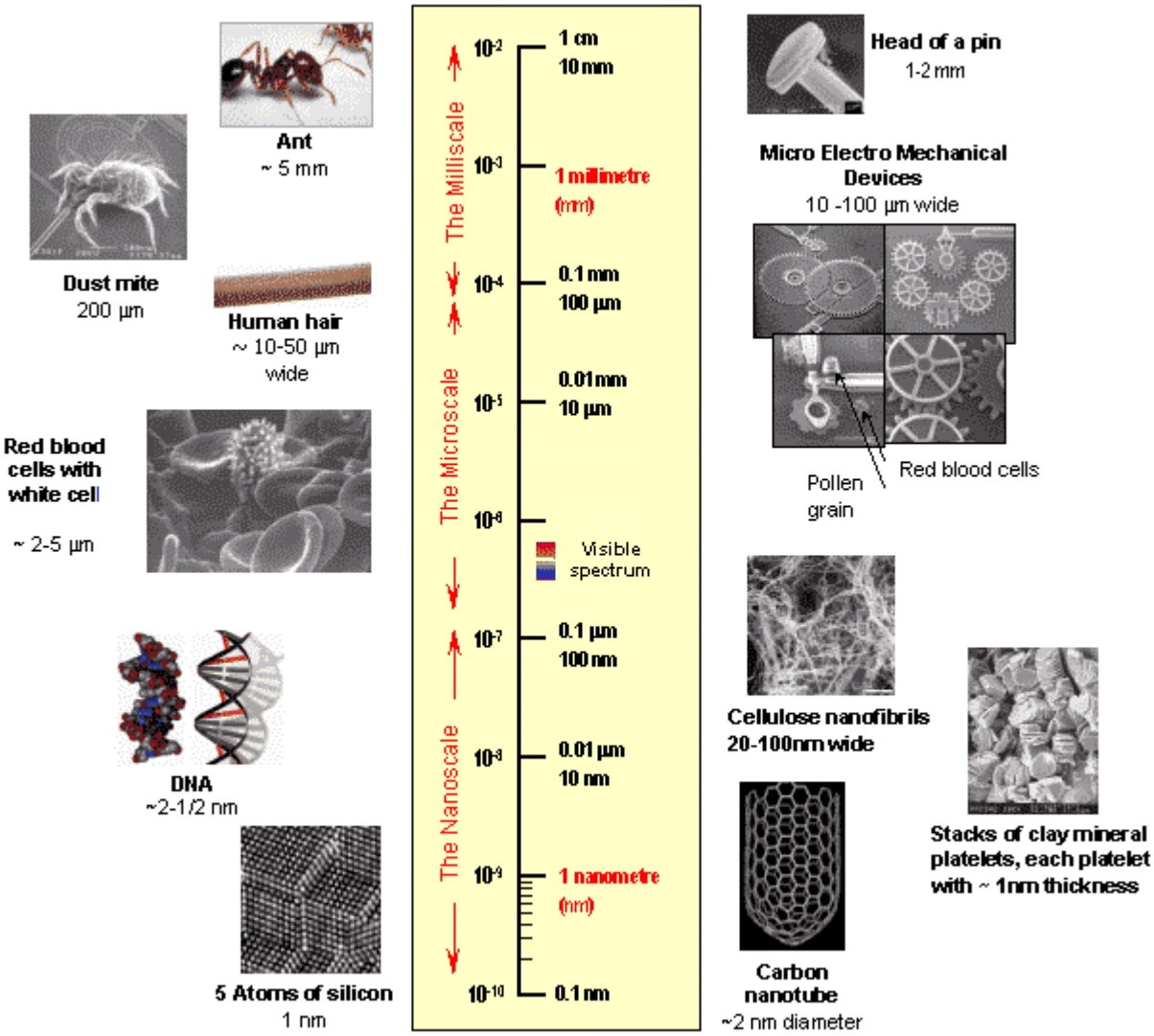

Figure 1.1 Comparison of nanometer in context [23].

Classification of Nanomaterials

In the nanostructured materials field, many names and labels have been used. It is significant that some terms are explained in the nanoscale materials**:**

Cluster A collection of units (atoms or reactive molecules) of up to about 50 units. Cluster compounds (Fig.1.2) are such moieties surrounded by a ligand shell that allows isolation of a molecular species (stable, isolable, soluble).

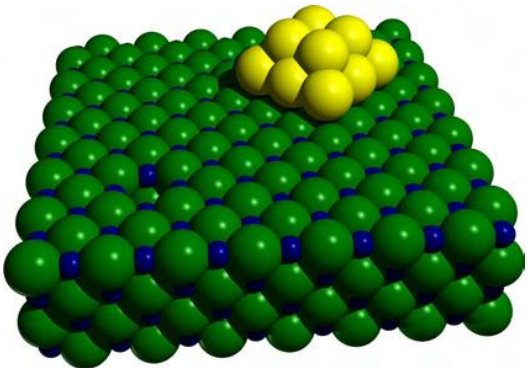

Figure 1.2 Schematic representation of a Pd nano cluster deposited on the (100) surface of magnesium oxide, MgO [24].

Colloid A stable liquid phase containing particles in the 1-1000 nm range. A colloidal particle is one such 1-1000 nm sized particle.

Nanoparticle A solid particle in the 1-1000 nm range that could be nanocrystalline, an aggregarate (Fig.1.3) of crystallites, or a single crystalline.

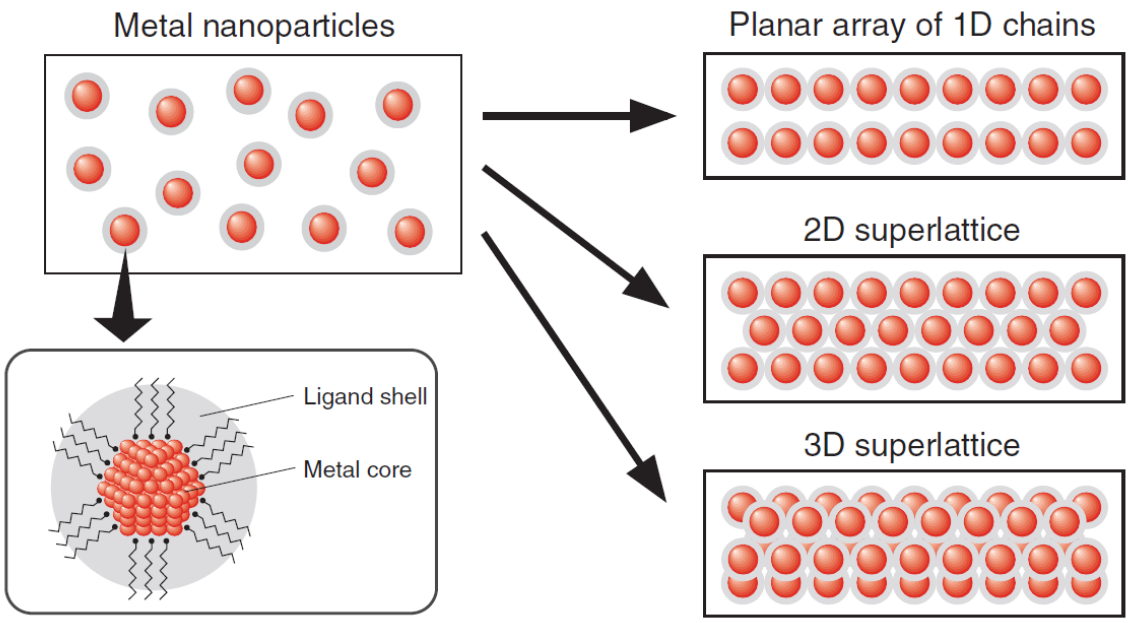

Figure 1.3 Schematic illustration of metal nanoparticle superlattices [25].

Nanocrystal A solid particle that is a single crystal in the nanometer size range.

Nanostructured or nanoscale material Any solid material that has at least one of its dimensions in 1-100 nm (Fig.1.1).

Nanophase material The same as nanostructured materials.

Quantum dot A particle that reveals a size quantization effect in at least one dimension. (Fig. 1.4) exhibits an example of quantum dots.

1.3 Magnetic NPs (MNPs)

Magnetic NPs (MNPs) have been the focus of an increasing amount of the recent literature, which was chronicled research into both the fabrication and applications of MNPs. The explosion of research in this area is driven by the extensive technological applications of MNPs which includes single-bit elements in high-density magnetic data storage arrays, magneto-optical switches, and novel photoluminescent materials. In biomedicine, MNPs serve as contrast enhancement agents for Magnetic Resonance Imaging, selective probes for biomolecular interactions, and cell sorters. NPs of magnetic metals are also finding applications as catalysts, nucleators for the growth of high-aspect- ratio nanomaterials, and toxic waste remediation. Methodologies for the synthesis of MNPs are being developed by scientists working in the fields spanning Biology, Chemistry, and Materials Science.

1.4 Methods For Categorizing Synthesis of NPs

There are many synthetic methods for the preparation of NPs [26,27]. The challenge is to control the nanoparticle size, size distribution, morphology, crystallinity, shape, and properties, to assemble the NPs for a given purpose, and to make them from a variety of materials. The synthetic methods reported can be classified according to synthesis strategies, the branches of science involved in the process, sources of energy input, and the media in which NPs are formed.

1.4.1 By Synthesis approach

Approaches are important for the synthesis of NPs. There are two basic approaches used in the syntheses of NPs: bottom up and top down [28-30].

1.4.1.1 Bottom-Up approaches

This approach is more in line with the basic strategy of nanoscience and technology. NPs are built up atom by atom, or molecule by molecule. Most nanoparticle syntheses belong to this category. A simple example of this approach is the flame synthesis of TiO_2 from gaseous $TiCl_4$ and oxygen according to

$$TiCl_4 + O_2 \rightarrow TiO_2 + 2Cl_2\bullet$$

It has been shown that nucleation and surface growth determine the primary particle size of titania [31-33].

1.4.1.2 Top-Down approaches

This approach is most applied in the traditional particle making process. Mechanical breakdown, such as high-energy ball milling, is a simple case of the top-down strategy. High energy ball milling is useful for deriving nanocrystalline materials of high-temperature phases without going to extreme heat treatment, which would promote significant grain growth and surface area loss. For example, nanocrystalline α–Al_2O_3 with a high surface area has been obtained through ball milling [34].

1.4.2 By Nature of the Process

1.4.2.1 Physical Methods

A physical process involves only changes in physical state, such as size, shape, and phase of the matter. Mechanical size reduction is a physical process. Condensing gaseous metal vapor into NPs is another example. The formation of NPs in the gas phase is accomplished by a rapid quenching of supersaturated metal vapors with room temperature or cold inert gas [35].

1.4.2.2 Chemical Methods

Most nanoparticle syntheses involve chemical changes. For instance, a sol–gel process converts metal alkoxides into oxide particles [36]. A hydrothermal process converts titanium isopropoxide and barium hydroxide into $BaTiO_3$ [37].

1.4.2.3 Biological Methods

Nanostructured materials are synthesized in nature by a process known as biomineralization (the *in vivo* formation of inorganic crystals and/or amorphous particles in biological systems [38,39]). In nearly all cases, the growth of the inorganic phases is controlled by biologically produced membranes or templates, which are usually composed of proteins and/or polysaccharides [40].

1.4.3 By Media of the Process

NPs are always formed in a medium of either gas phase, liquid phase, or solid phase. The classifications based on the media where NPs are formed are perhaps the most important and most widely used classification [41]. The media for nanoparticle syntheses are usually classified as

- gas phases
- liquid phases
- solid phases

The detailed discussion in this chapter is arranged according to this medium classification.

1.5 General Synthesis Methods By Media

1.5.1. Gas-Phase Synthesis

Gas-phase syntheses where particles are formed as a result of reactions among gaseous molecules, gas molecule condensation and/or decomposition, nucleation, growth, and possibly agglomeration. In general, gas-phase syntheses using gases as reactants involve low concentration because of the low density of gases [42]. This has an advantage for producing NPs because nucleating particles in such low concentrations tend to be less agglomerated. Gas-phase syntheses can be divided into three broad types: vapor condensation, vapor reaction (the latter includes vapor decomposition), and aerosol.

Vapor condensation synthesis includes many different methodologies like inert gas evaporation technique, matrix isolation method, gas flow/cold trap method, and gas flow/solution trap method. Vapor reaction synthesis can be further divided into two types; flame synthesis and chemical vapor reaction. Aerosol synthesis is classified into two broad types: aerosol pyrolysis (spray pyrolysis) and flame–aerosol pyrolysis. Fumed silica is synthesized by feeding gaseous $SiCl_4$ together with air and hydrogen into the burner to form a silica aerosol [43,44].

1.5.2 Liquid-Phase Synthesis

Liquid-phase syntheses are the most common and diverse methods for nanoparticle synthesis. The most common solvent is water, but more and more organic solvents are also used in an effort to reduce the agglomeration of NPs.

The liquid-phase synthesis methods can be mainly classified as chemical precipitation and coprecipitation, hydrothermal synthesis, synthesis in microemulsion or reverse micelles, solvothermal synthesis, microwave heating-assisted synthesis, sonochemical synthesis, and electrochemical synthesis.

1.5.2.1 Chemical Precipitation and Coprecipitation

One of the oldest techniques for the synthesis of NPs is the precipitation of products from bulk solutions. In precipitation reactions, the metal precursors are dissolved in a common solvent (such as water) and a precipitating agent is added to form an insoluble solid. Many magnetic NPs can be synthesized using these classical aqueous precipitation reactions to yield NPs that have broad size distribution and irregular morphology. These reactions can generate a wide range of magnetic materials including spinel ferrites, perovskites, metals, and alloys. The major advantage ofprecipitation reactions is that large quantities of particles can be synthesized. However, it is difficult to tailor the particle size as only kinetic factors are available to control growth. Chelating agents (or ligands with multiple binding sites) may be used to help control the particle size, decomposing as the precursor is heated. The size and morphology of precipitated NPs can be tailored with limited success through the tight control of synthesis parameters such as pH, metal cation concentration, and the type of the precipitating agent [45]. Firstly Massart [46] synthesized, Fe_3O_4 NPs were precipitated from $FeCl_3$ and $FeCl_2$ at a slightly basic pH of 8.2. Massart later expanded the synthesis of alkaline precipitation to include mixed ferrites (MFe_2O_4, where M = Co [47], Mn [47,48], MnZn [49], and NiZn [50]).

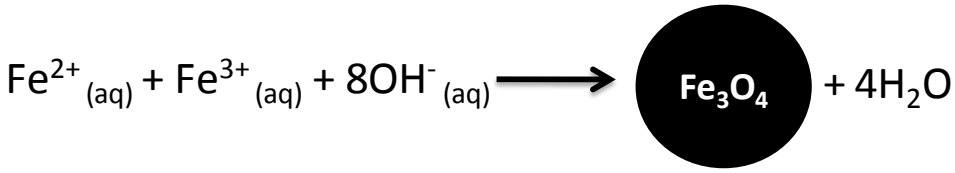

Figure 1.4 Schematic of synthesis of Fe_3O_4 by using ferric salts [51].

1.5.2.2 Hydrothermal Synthesis

Hydrothermal synthesis involves the exploitation of the properties of water under high pressure and temperature for the preparation of fine powders. The typical values of the reaction temperatures are between the boiling point of water and the critical temperature of 374^{o}C and pressures up to 15 MPa. The advantage of the hydrothermal method over other solution routes is that the final product readily forms at a low temperature without calcination. The precursor sol is prepared from oxides, hydroxides, nitrates, or halides of the corresponding metallic elements. The prepared sol is subjected to hydrothermal synthesis, which is carried out in a high-pressure apparatus or hydrothermal bomb (autoclave). The basis of the technique is the enhanced solubility of the precursor in water under hydrothermal conditions, which ensures the formation of the product with very good composition control and uniformity [52].

1.5.2.3 Solvothermal Synthesis

Solvothermal synthesis is a similar process to hydrothermal except that the reaction is done in a solvent such as alcohol. Crystalline $BaTiO_3$ nanopowders have been produced using a solvothermal process. This process had the advantages that stoichiometric powder can be obtained, the process was run under milder conditions than in an aqueous hydrothermal process, and the nanosized particles had a narrower size distribution and exhibited less agglomeration [53].

1.5.2.4 Microwave Assisted Synthesis

Microwave-assisted synthesis for the production of inorganic compounds has been studied since 1986. As compared to conventional oven heating (with a slow heating rate and heat transfer), microwave “volumetric” heating of liquids is an alternative heating approach with specific advantages. Microwave heating of the hydrothermal reactor was found in some cases to cut the reaction time significantly, to generate remarkable size uniformity, and to produce some new phases [54]. Using nitrates of nickel, cobalt, and iron in combination with glycine, fine nickel-doped cobalt ferrite powders have been successfully synthesized by microwave-induced combustion [55].

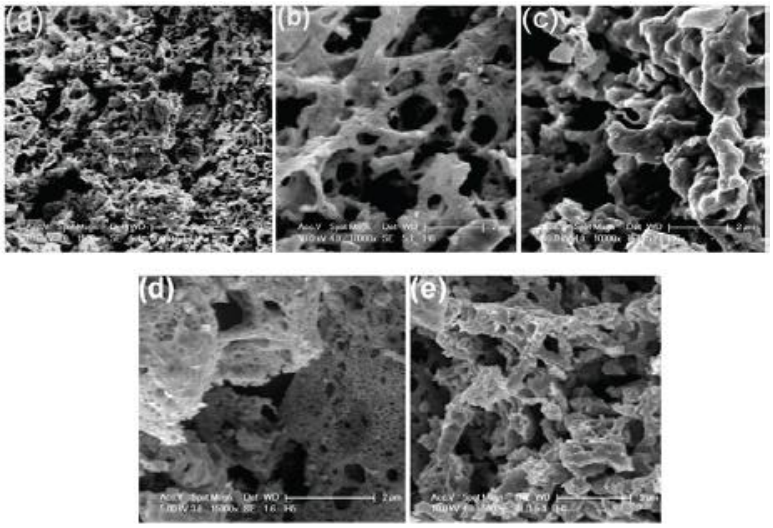

Figure 1.5 SEM micrographs of $Ni_xCo_{1-x}Fe_2O_4$ where x is **a)** 0, **b)** 0.4, **c)** 0.6, **d)** 0.8, **e)** 1.0 [55].

1.5.2.5 Synthesis in Microemulsions or Reverse Micelles

Microemulsion can be defined as an isotropic, thermodynamically stable system constituting the micrometer-sized droplets (micelle) dispersed in an immiscible solvent and an amphiphilic surfactant species on the surface of the micelle. The crucial aspect of the microemulsion route is the control of the nanoparticle size through suitable selection and addition of a surfactant prior to the hydrolysis of the metal alkoxide sol (reverse micelle or water-in-oil emulsion). The addition of the surfactant molecules creates aqueous domains (nanoreactors) in the range of 0.5–10 nm. By properly tuning the water/surfactant ratio, which is critical in deciding the final particle size, the diameter of the aqueous droplets can be tuned. The difference between the conventional sol–gel method and emulsion-mediated synthesis is that the rate of hydrolysis is controlled by the diffusion of the precursors from the oil phase to the aqueous droplets. The method has been recognized as the most appropriate for the synthesis of ultra-fine magnetic NPs for potential applications in magnetic recording media, biomedical, and related fields [56,57].

1.5.2.6 Sonochemical Synthesis

Application of ultrasound in chemical synthesis has initiated a new fascinating field in processing technology. As the name of the route suggests, the sound waves act as the energy source, when the respective sol of the material to be prepared is exposed to high-intensity ultra sound. The underlying mechanism of sonochemical processing route consists of the formation, growth, and collapse of the bubbles of the sol upon exposure to acoustic waves to

form the product phase [58]. An acoustic cavitation process can generate a transient localized hot zone with extremely high temperature gradient and pressure. The sudden changes in temperature and pressure destroy the precursor material which enables the formation of NPs. A simple sonochemical route by modifying the different parameters has been used to successfully synthesize the sphere-like Co_3O_4 nanocrystals which are indexed as the cubic spinel structure and Mn_3O_4 nanostructures [59].

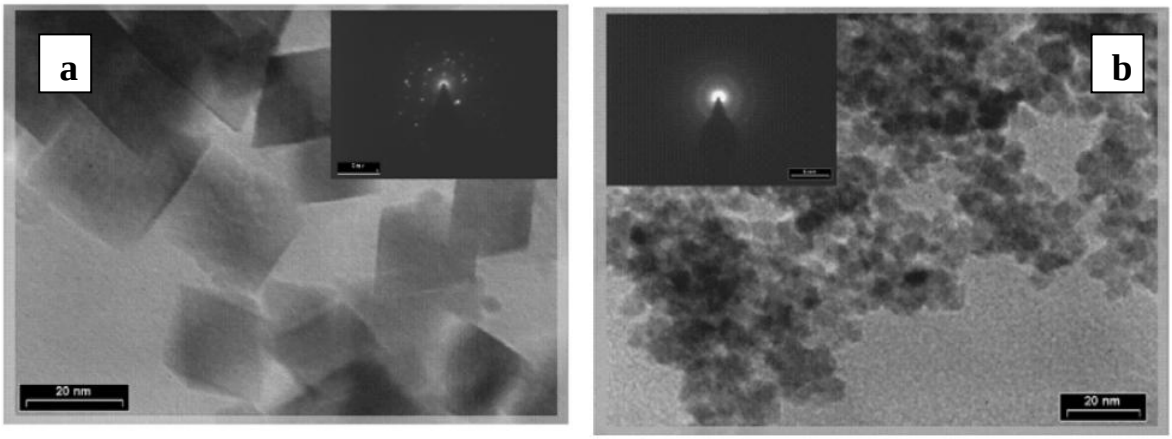

Figure 1.6 TEM images and ED patterns (inset) of **(a)** Co_3O_4 and **(b)** Mn_3O_4 [59].

1.5.2.7 Electrochemical Synthesis

Reetz and coworkers developed this very versatile method to synthesize for nanostructured mono- and bimetallic colloids by since 1994 [60,61]. The overall process of electrochemical synthesis can be occured according to equation (1).

$$\begin{array}{lll} \text{Anode:} & M_{bulk} \rightarrow M^{n+} + ne^- & \\ \text{Cathode:} & M^{n+} + ne^- + \text{stabilizer} \rightarrow M_{coll}/\text{stabilizer} & (1) \\ \hline \text{Sum} & M_{bulk} + \text{stabilizer} \rightarrow M_{coll}/\text{stabilizer} & \end{array}$$

Advantages of the electrochemical pathway are that contamination with by products resulting from chemical reduction agents are avoided, and that the products are easy to isolate from the precipitate. The electrochemical method has been successfully applied to prepare Pd [62] on a scale of several hundred milligrams (yields >95%).

1.5.3 Solid-Phase Synthesis

Solid-phase syntheses are those methods in which NPs are formed directly from solids or semisolids (such as viscous liquids). Most of these types of syntheses belong to the top-down approach, which includes;

- Mechanical Milling
- Mechanochemical Processing
- Cryochemical Processing
- Self-Combustion Method
- Solid-State Synthesis
- Colloidal Assembly Method
- Selective Leaching of a Single-Phase Solid-Solution Method

1.6 Applications of MNP's

Magnetic NPs have a wide range focuses in many diverse applications. These applications make use of magnetic NPs in a variety of forms; as surface functionalized particles for biomedical applications, as tracers and alternatives to radioactive materials, as particle arrays in magnetic storage media, as powder compacts for power generation, conditioning and conversion; in solution and as ferrofluids for audio speakers.

1.6.1 Biomedical Applications

Superparamagnetic NPs have a high potential for several biomedical applications based on their physical and chemical properties. They are a potential candidate to be used in (a) drug delivery, (b) tissue repair, (c) detoxification of biological fluids, (d) hyperthermia (e) magnetic resonance imaging (MRI) [63-66]. The particles must show a high magnetic saturation, biocompatibility and a functional surface in order to be considered a good candidate for above applications. The surfaces of these particles could be modified through organic or non-organic molecules. It is also been reported that the surface of magnetic NPs have been modified through oxide layers (e.g. silica or alumina) in some cases [67]. These modifications are suitable to further be functionalized by the attachment of various bioactive molecules such as peptides, antibodies, drugs, etc.

1.6.1.1 Drug delivery

Surface modified magnetic NPs can be employed as a drug carrier for site-specific delivery of drugs (Fig 1.11) [68]. As the magnetic particles traverse the target organ capillaries, an applied external magnetic field may retain these particles at the desired site. Retained particles may undergo extravasation, which could ultimately lead to intracellular (i.e., tumor cell) drug uptake. Several studies demonstrated that biodegradable polymers are ideal candidates for drug carriers since they show minimum toxicity and immunological response [69,70] . The potential advantage of a magnetically guided drug delivery system is reduced drug doses and potential side effects to healthy tissues. It has also been reported that PEG-coated superparamagnetic NPs did not affect cell adhesion behavior or morphology after incubation with immortalized fibroblasts [63]. Particle size and charge along with surface must be modified to enhance their blood circulation time as well as bioavailability of the particles within the body [71]. In addition, magnetic properties and cellular internalization of particles strongly depends on the size and size distribution of the magnetic NPs [72].

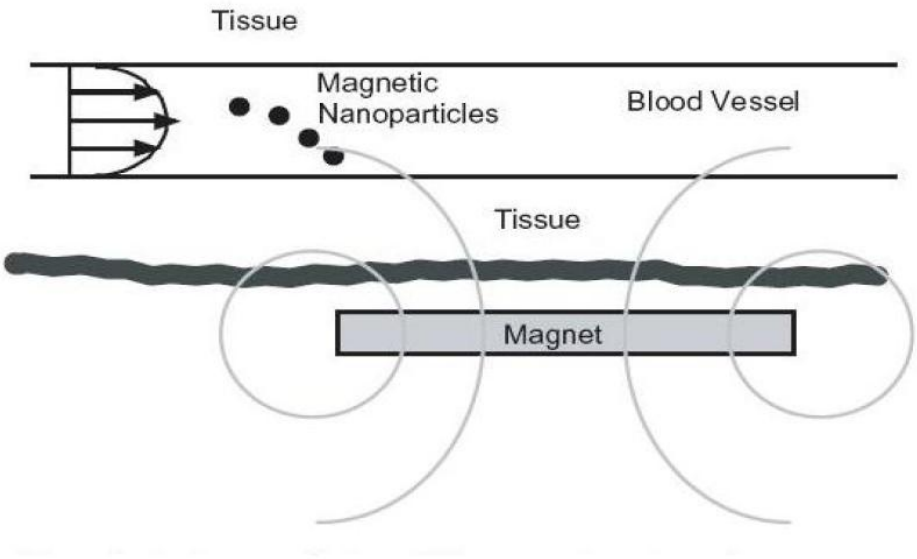

Figure 1.7 Magnetic NPs as drug carrier vehicles [68].

1.6.1.2 Magnetic resonance imaging

MRI is a medical imaging method used to obtain images of the body in thin slices [73]. When a strong external magnetic field is applied to the body, a hydrogen nucleus in water aligns itself in the applied field direction. MRI then measures the characteristics of hydrogen nuclei of water after a radio wave is applied to push some of these protons out of alignment. Since protons in different tissues of the body (fat, muscle, etc.) re-align at different

speeds, the different structures of the body can be revealed [74]. MRI gives spatial distribution of the intensity of water proton signals in the volume of the body. The signal intensity in MRI depends on the amount of water in the given place and on the magnetic relaxation times T_1 (longitudinal relaxation time) and T_2 (transverse relaxation time).

Longitudinal relaxation time T_1 and transverse relaxation time T_2 show remarkably different behavior in the presence of paramagnetic species. The resulting effects seen in NMR spectroscopy have proven the shortening of both T_1 and T_2 in the presence of paramagnetic species used as contrast agents. Studies have also shown that complexation of the metal ion with organic ligand, might alter paramagnetic properties of the metal while significantly decreasing the toxicity effect.

The two most widely used contrast agents for MRI scanning are gadolinium-based agents, which are T_1 contrast agents that cause positive contrast enhancement and provide brighter images upon accumulation in the target site, and superparamagnetic iron oxide particles, which are T_2 contrast agents that give negative contrast enhancement and thus darker images in areas of accumulation.

Superparamagnetic iron oxide-based contrast agents

Superparamagnetic iron oxide NPs are known to have a much larger effect on relaxation time compared with paramagnetic materials. Because of their single domain structure, the entire moments within the crystal structure align in the direction of the magnetic field when placed in an external field and enhance the magnetic flux. These particles do not retain any magnetization after the removal of the external field. This ability to disturb the local magnetic field through large magnetic moments leads to a rapid change in coherence of surrounding protons called dephasing, hence resulting in a detectable change in the MR signal through altering longitudinal and transverse relaxation of the surrounding water nuclei. In research of C. Sun et al.,Chlorotoxin, a short peptide found in scorpion venom, has been combined with iron oxide NPs that act both as an MRI contrast agent and to increase the effectiveness of the venom in killing cancer cells [75].

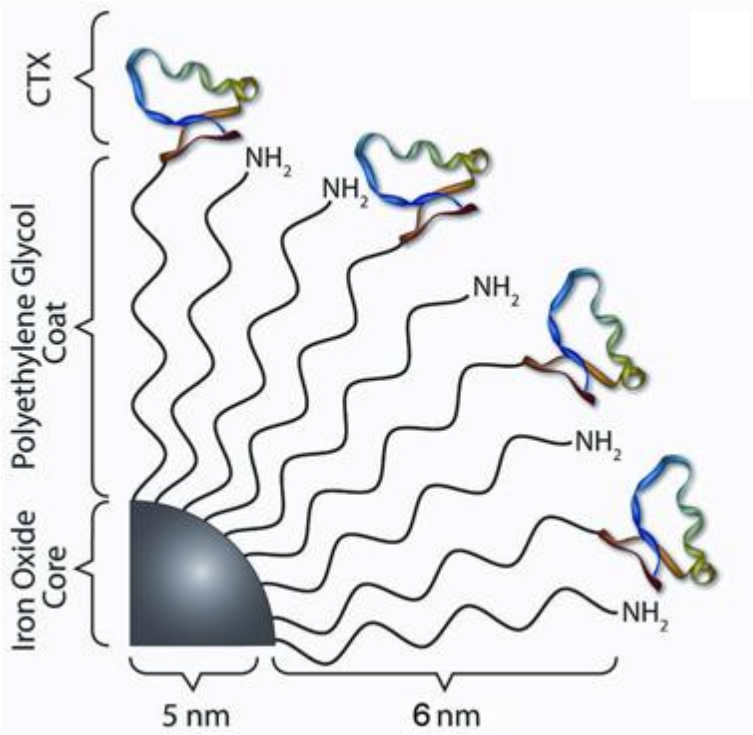

Figure 1.8 Diagram of the nanoprobe - the chlorotoxin (CTX) is held onto the iron oxide nanoparticle by a short polymer linker [75].

1.6.2 Magnetic Recording Media

Synthesis and assembly of magnetic NPs have attracted great attention because of their potential application in ultrahigh-density magnetic recording [76]. Continue increase in the areal density of hard disk drive will be limited by thin film media in which each bit of information is stored over hundreds of grains. Extensive researches are being done on $CoFe_2O_4$ and FePt NPs for high density recording media [77,78]. $CoFe_2O_4$ NPs are well-known material with very high cubic magnetocrystalline anisotropy, good coercivity, and moderate saturation magnetization [77-80]. These properties make $CoFe_2O_4$ NPs a promising material for high-density magnetic recording devices.

1.6.3 Exchange-Coupled Nanocomposite Magnets

Exchange-coupled nanocomposite magnet consists of a uniform mixture of exchange coupled magnetically hard and soft phases. This type of magnets are promising for advanced permanent magnetic applications as high energy products $(BH)_{max}$ and relatively high coercivities can be developed in these nanocomposite magnets. A small grain size (less than 20 nm) and a uniform mixture of the hard and soft phases are required for effective exchange coupling between the hard and the soft phases. Zeng *et al.* in 2002 demonstrated that

exchange-coupled nanocomposite magnet such as FePt-Fe_3Pt can be made using monodisperse NPs of FePt and Fe_3O_4 as precursors by self assembly technique [81]. In exchange-coupled isotropic FePt- Fe_3Pt nanocomposite the energy product of 20.1 MGOe was achieved, which is 50% higher than that expected theoretically from a single phase, non-exchange-coupled isotropic FePt.

Recently, the same group prepared an exchange-coupled bimagnetic core/shell NPs system with ferromagnetic FePt core and ferrimagnetic MFe_2O_4 (M=Fe, Co) shell [82].

1.6.4 Ferrofluids

A ferrofluid is a special solution of magnetic NPs in a colloidal suspension whose flow can be controlled by magnets or magnetic fields [83]. Particles are coated with a surfactant that disperse the particles and prevents agglomeration by overcoming the van der Waals forces that exists between the particles [84]. As a result when fluid is not in presence of external magnetic field it has zero net magnetization. When a strong magnet is brought close to the ferrofluid, several spikes will appear, as the fluid arranges itself along the magnetic field lines of the magnet. When the field is removed, the particles again disperse randomizing their orientation and establishing no net magnetization [84,85]. These unique properties make ferrofluids have applications in numerous fields of technology. The most common application of ferrofluids is the cooling of loudspeakers [83]. Some of the other technological applications of ferrofluid include bearing, dampers, stepping motors, and sensors [83,84,86].

1.7 Magnetism of MNPs

Magnetism is a group of phenomena associated with magnetic fields which exist around a magnetic body or a current-carrying conductor. Whenever an electric current flows a magnetic field is produced. As the orbital motion and the spin of atomic electrons are equivalent to tiny current loops, individual atoms create magnetic fields around them. The magnetic moment of an atom is the vector sum of the magnetic moments of the orbital motions and the spins of all the electrons in the atom. This vector sum of magnetic moments can be either strong or weak depending on their alignment which is dominated by the magnetic interactions.

1.7.1 Type of Magnetism

All materials exhibit unique magnetization behavior and from the magnetization profiles can be categorized. Among the categories, diamagnetic and paramagnetic materials are considered as “weak magnetic” materials because the magnetization is relatively small. Ferromagnetic and ferrimagnetic materials exhibit large magnetization with applied field. The magnetic behavior of materials can be classified into the following five major groups [87]:

1.7.1.1 Diamagnetism

All materials exhibit diamagnetism; however, the effect of diamagnetism is small and often shadowed by other magnetic effects. A diamagnetic material has the ability to “repel” magnetic fields, with the flux density in diamagnetic materials actually being less than in vacuum. Classically, diamagnetism is explained by the reduction of the electron velocity due to an external magnetic field. To understand diamagnetism, first consider an atom with an electron moving clockwise in an orbit perpendicular to an applied field. Since the electron carries an electrical charge, the orbital motion of the electron is equivalent to a current on a conductor loop. By Faraday’s law, the increase in the applied field generates an induction current on the loop to produce an opposing field. For an orbiting electron the opposing field is generated by decreasing the electron velocity. Now consider another electron orbit adjacent to this orbit, with its plane parallel to the first one but the electron moving counterclockwise. In the absence of an external applied field, the moments of these two electrons cancel each other, yielding zero net moment. As the applied field increases, both orbits produce a magnetic moment opposing the applied field.

Examples of diamagnetic materials are noble gases such as helium, neon, and argon, diatomic gases such as hydrogen and nitrogen, ionic solids such as sodium chloride (NaCl), and almost all organic compounds. Many metals also exhibit diamagnetic properties, for example, copper, zinc, silver, cadmium, gold, mercury, lead, and bismuth.

1.7.1.2 Paramagnetism

Paramagnetic materials are composed of atoms or molecules that have a net magnetic moment because the spin and orbital moments of electrons do not completely cancel out. In the absence of applied fields, the magnetic moments are oriented randomly and thus macroscopically the net moment of a paramagnetic material is zero. When a magnetic field is applied on the material, the magnetic moments tend to align with the field. However, thermal agitation in the atoms or molecules opposes this tendency and tries to keep the moments in

random states. This will result in a partial alignment of the magnetic moments; thus a small positive susceptibility is observed in paramagnetic materials. Increasing temperature increases the thermal energy in the atoms or molecules and therefore reduces the susceptibility.

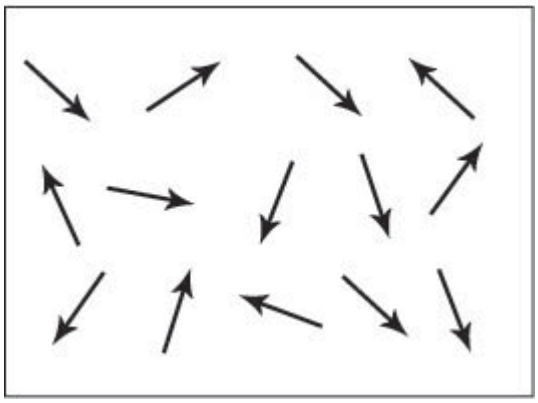

Figure 1.9 Schematic showing the magnetic dipole moments randomly aligned in a paramagnetic sample in the absence of magnetic field [87].

1.7.1.3 Ferromagnetism and Ferrimagnetism

Ferromagnetic and ferrimagnetic materials are perhaps the most useful materials for technical applications. Like paramagnetic materials, each molecule in the ferro- and ferrimagnetic materials contains a net magnetic moment. However, because of the existence of a strong molecular field that aids the applied field in the magnetization process, the susceptibility of ferro- and ferrimagnetic materials is much larger than paramagnetic materials, ranging from 10^2 to 10^6. Even under zero applied field, the atomic moments of ferromagnetic materials are oriented in parallel due to the strong molecular field (in quantum magnetism, it is the Exchange energy that causes the alignment of the moments), causing a large spontaneous magnetization. Ferrimagnetic materials are composed of antiparallel atomic moments that do not completely cancel out.

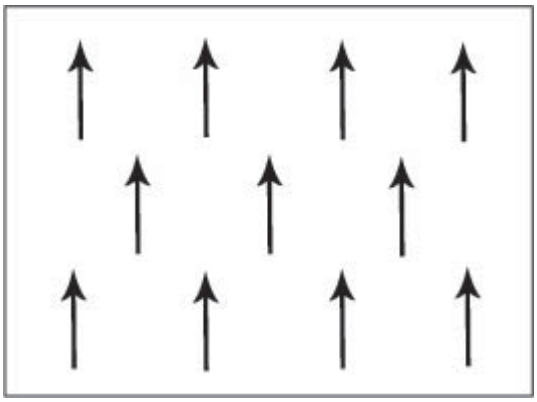

Figure 1.10 Schematic showing the magnetic dipole moments aligned parallel in a ferromagnetic material [87].

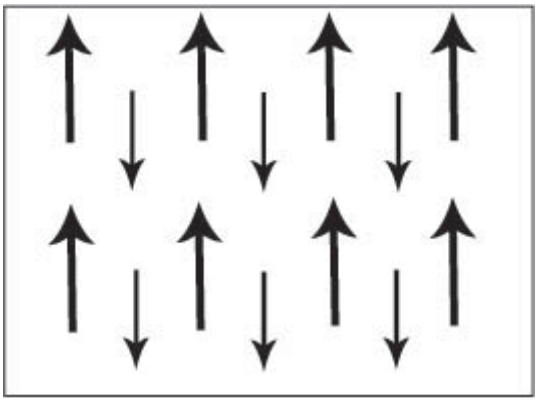

Figure 1.11 Schematic showing adjacent magnetic moments of different magnitudes aligned anti-parallel in a ferrimagnetic material [87].

Three distinct characteristics of ferromagnetic materials are their; 1) Spontaneous Magnetization, 2) Curie Temperature, 3) Hysteresis.

Spontaneous magnetization

Spontaneous magnetization is the term used to describe the appearance of an ordered spin state (magnetization) at zero applied magnetic field in a ferromagnetic or ferrimagnetic material below a critical point called the Curie temperature or T_C. the transition of a material from ferromagnetism to paramagnetism with increasing temperature. At low temperature, the material exhibits strong ferromagnetism with a large magnetization M_{S0}. As the temperature

increases, the saturation magnetization decreases and becomes zero at T_C. Above T_C, the susceptibility of the material decreases with temperature.

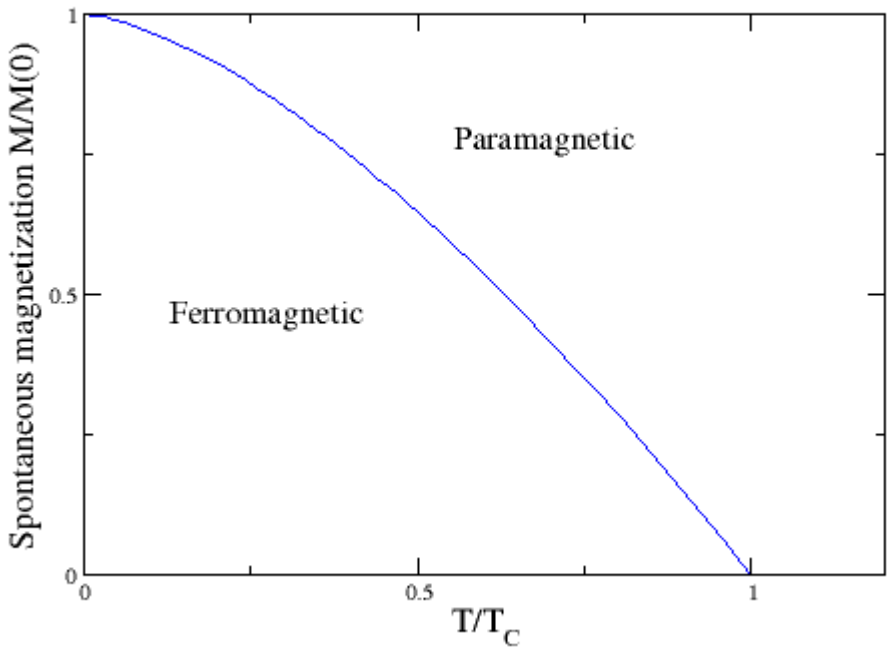

Figure 1.12 The transition of a material from ferromagnetic state to paramagnetic. The material is ferromagnetic below T_C, but becomes paramagnetic above T_C according to the Curie–Weiss law [88].

Curie Temperature

Above a critical temperature T_C, the Curie temperature, all ferromagnetic materials become paramagnetic. This is because thermal energy is large enough to overcome the cooperative ordering of the magnetic moments.

The susceptibility of a material, χ, indicates how dramatically a material responds to an applied magnetic field, and is defined as the ratio of the magnetisation of the material, M, and the applied magnetic field, H.

$$X = \frac{M}{H} \qquad (1)$$

The magnetisation of a material, *M*, is defined as the magnetic moment per unit volume or per unit mass of a material and is dependent on the individual magnetic dipole moments of the atoms in the material and on the interactions of these dipoles with each other.
Above the Curie Temperature there will be a change in the susceptibility as the material becomes paramagnetic, therefore giving the equation:

$$X = \frac{C}{T - T_C} = \frac{M}{H} \qquad (2)$$

where *C* is a constant.

The Fig. 1.18 shows the saturation magnetisation (i.e. that obtained in a high magnetic field) of a ferromagnetic element, nickel, as a function of temperature [88]. The saturation magnetisation decreases with increasing temperature until it falls to zero at the Curie temperature where the material becomes paramagnetic:

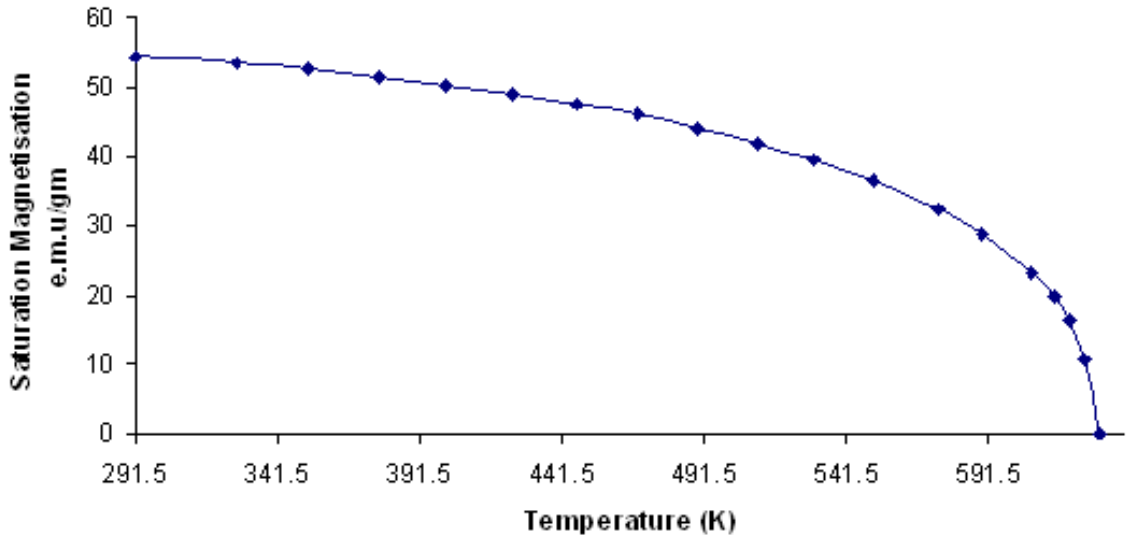

Figure 1.13 Variation of saturation magnetisation with temperature for Nickel [89].

Hysteresis Loop

When a ferromagnetic material is magnetized in one direction, it will not relax back to zero magnetization when the imposed magnetizing field is removed. It must be driven back to zero by a field in the opposite direction. If an alternating magnetic field is applied to the material, its magnetization will trace out a loop called a hysteresis loop. The lack of retraceability of the magnetization curve is the property called hysteresis. If the external applied field is removed the single domain will rotate back to the easy direction in the crystal. A demagnetising field will be set up due to the single domain, and this field initiates the formation of reverse magnetic domains as these will lower the magnetostatic energy of the sample by reducing the demagnetising field. However the demagnetising field is not strong enough for the domain walls to be able to grow past crystal defects so they can never fully reverse back to their original positions when there is no external applied field. This results in the *hysteresis* curve as some magnetisation will remain when there is no external applied field. This magnetisation is called the remanent magnetisation, B_r. The field required to reduce the magnetisation of the sample to zero is called the coercive field H_c. And the saturation magnetisation B_s is the magnetisation when all the domains are aligned parallel to the external field. These are shown on the schematic below:

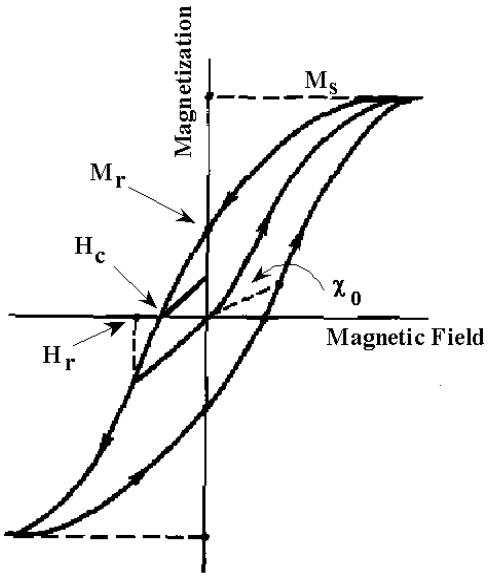

Figure 1.14 Schematic showing the general shape of the hysteresis curve with some relevant points marked; M_S, the saturation magnetisation; M_r, the remanentmagnetisation; H_C, the coercive field [87].

1.7.1.4 Antiferromagnetism

This spontaneous antiparallel coupling of atomic magnets is disrupted by heating and disappears entirely above a certain temperature, called the Néel temperature, characteristic of each antiferromagnetic material. (The Néel temperature is named for Louis Néel, French physicist, who in 1936 gave one of the first explanations of antiferromagnetism.) Some antiferromagnetic materials have Néel temperatures at, or even several hundred degrees above, room temperature, but usually these temperatures are lower. The Néel temperature for manganese oxide, for example, is 122 K (−151° C).

Antiferromagnetic solids exhibit special behaviour in an applied magnetic field depending upon the temperature. At very low temperatures, the solid exhibits no response to the external field, because the antiparallel ordering of atomic magnets is rigidly maintained. At higher temperatures, some atoms break free of the orderly arrangement and align with the external field. This alignment and the weak magnetism it produces in the solid reach their peak at the Néel temperature. Above this temperature, thermal agitation progressively prevents alignment of the atoms with the magnetic field, so that the weak magnetism produced in the solid by the alignment of its atoms continuously decreases as temperature is increased.

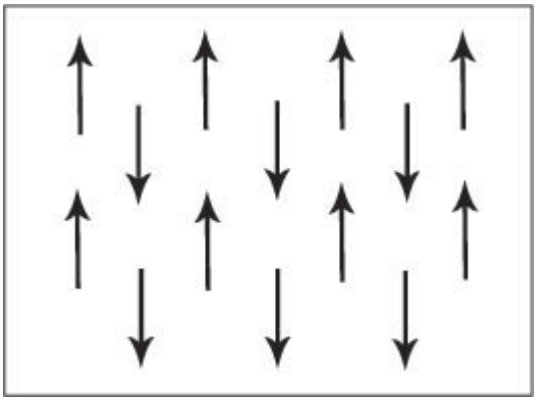

Figure 1.15 Schematic showing adjacent magnetic dipole moments with equal magnitude aligned anti-parallel in an antiferromagnetic material [87].

1.8 Crystal Structure

1.8.1 Spinels

Several of the commercially important magnetic oxides have the spinel structure (AB_2O_4) (Fig.1.19). The parent spinel is $MgAl_2O_4$. It has an essentially cubic closed packed

array of oxide ions with Mg^{2+}, Al^{3+} in tetrahedral and octahedral interstices, respectively. There are well over a hundred compounds with the spinel structure such as oxides, sulphides and tellurides. The other divalent cation can be many different transition metal species including Fe^{2+}, Co^{2+}, Ni^{2+} and Zn^{2+} among others. The structure as illustrated in Fig.1.19 can be thought of as a face centered cubic lattice of oxygen anions with metal cations distributed on the tetrahedral and octahedral sites, sometimes denoted as the A and B sites respectively.

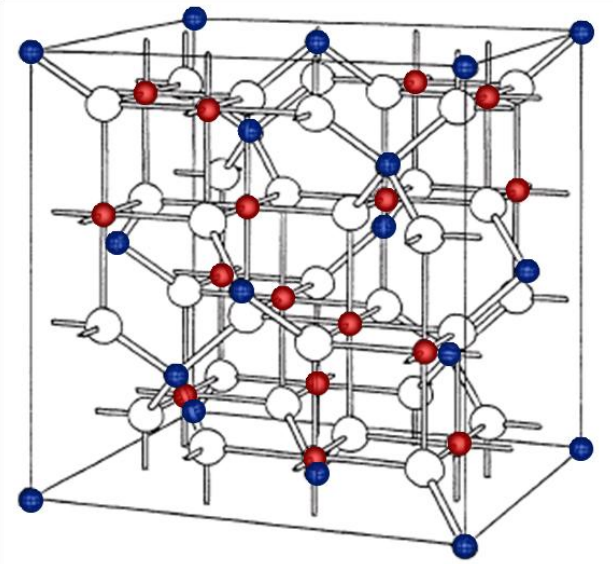

Figure 1.16 Crystal structures of magnetite (Fe_3O_4). Blue atoms are tetrahedrally coordinated Fe^{2+}; red atoms are octahedrally coordinated, 50/50 Fe^{2+}/Fe^{3+}; white atoms are oxygen [90].

Normal spinel: $(Me^{2+})[Fe^{3+}{}_2]O_4$ (Me^{2+} = Fe^{2+}, Zn^{2+}, Mn^{2+}, Ni^{2+}, Co^{2+}, etc.)

Inverse spinel: $(Fe^{3+})[Me^{2+}{}_xFe^{3+}]O_4$

General formula: $(Me^{2+}{}_{1-x}Fe^{3+}{}_x)[Me^{2+}{}_xFe^{3+}{}_{2-x}]O_4$

(x degree of inversion - proportion of 3-valent cation (Fe^{3+}) at tetrahedral lattice sites).

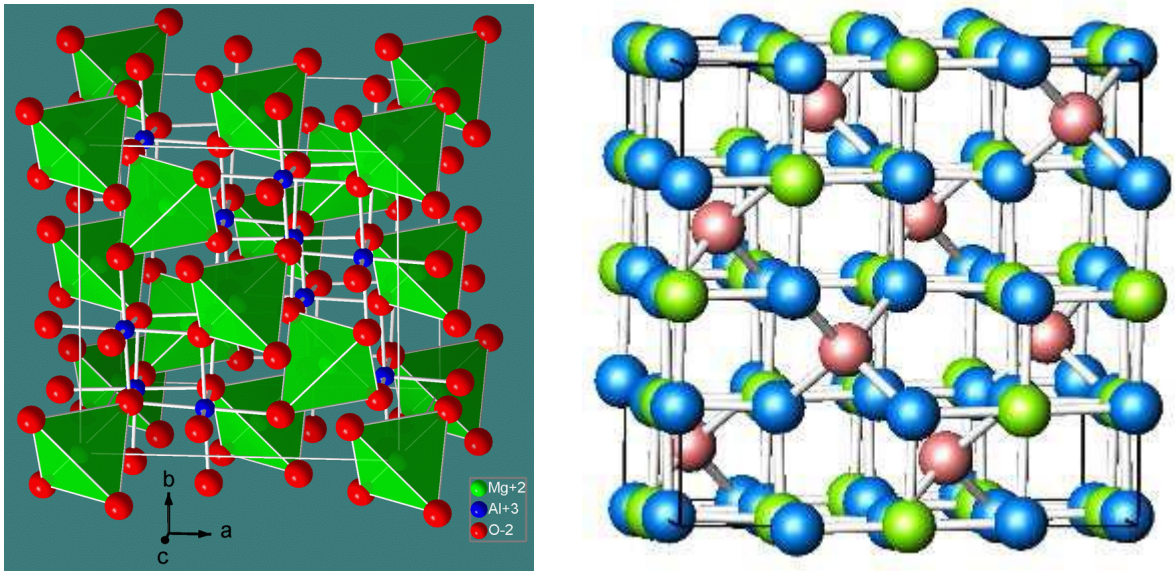

Figure 1.17 Spinel structure of **a)** $MgAl_2O_4$ [91a], **b)** $CoFe_2O_4$. The green atoms are Co, pink atoms are Fe, and blue atoms are O [91b].

CHAPTER 2

EXPERIMENTAL

2.1 Instrumentation

2.1.1 X-ray Powder Diffraction (XRD)

Huber JSO-DEBYEFLEX 1001 Diffractometer in GYTE, Philips diffractometer with PW 3020 goniometer and Rigaku diffractometer with D/max RINT-2200 with Cu K_α radiation were used for the characterization of crystalline products.

The lattice parameter "*a*" for the synthesized iron oxide NPs using TREOR 90 program and the mean size of the crystallites was estimated from the diffraction pattern by line profile fitting method using the equation (1) given in ref [92,93].

2.1.2 Electron Microscopy

2.1.2.1 Scanning Electron Microscopy (SEM)

Scanning Electron Microscopy (SEM) analysis was performed, using FEI XL40 Sirion FEG Digital Scanning Microscope (Samples were coated with gold at 10 mA for 2 min prior to SEM analysis) to investigate the microstructure of the nanocrystalline products.

2.1.2.2 Transmission Electron Microscopy (TEM)

Transmission Electron Microscopy (TEM), analysis was performed using a FEI Tecnai G^2 Sphera Microscope. A drop of diluted sample in ethanol was deposited on a TEM grid and alcohol was evaporated. Particle size distribution was obtained from several micrographs, counting a minimum of 150 particles.

2.1.3 Fourier Transform Infrared Spectroscopy (FTIR)

Fourier transform infrared (FT-IR) spectra were recorded in transmission mode with a Perkin Elmer BX FT-IR infrared spectrometer. The powder samples were ground with KBr /

sample weight ratio of 100/3 mg. and compressed into a pellet. FTIR spectra in the range 4000–400 cm^{-1} were recorded in order to investigate the nature of the chemical bonds formed.

2.1.4 Zeta Potential

Zeta potential and particle size measurements (DLS) were performed using a Brookhaven Instruments 90 Plus Nano Particle Size Analyzer in folded capillary zeta potential cells, and pH titrations were performed using 0.05 M NaOH and 0.05 M HCl.

2.1.5 Electron Spin Resonance (EPR)

A conventional X-band (f = 9.8 GHz) Bruker EMX model EPR spectrometer equipped with a cylindrical TE011 cavity employing an ac magnetic field (modulation frequency: 100 kHz) modulation technique was used for magnetic characterization. Operating conditions were 20.07 mW microwave power, 15 G modulation amplitude, center field 8000 G, time constant 40.96 ms and sweep time 41.94 s with multiple accumulations to enhance the signal-to-noise ratio. The sample (about 2mmx3mm) was placed onto a quartz sample holder, put into the cavity and held in either parallel or perpendicular orientation to the sample plane of the applied magnetic field. EPR spectra were obtained by sweeping the magnetic field from 0 to 16 kOe. The magnetic field was calibrated using a α, α-diphenil-β-picryl hydrazyl (DPPH) sample (g= 2.0036). The field derivative of microwave power absorption, dP/dH, was registered as a function of DC magnetic field H. To obtain the intensity of microwave power absorption, P, digital integration of the EPR curves was performed by using Bruker WinEPR software.

2.1.6 Impedance Spectrometer

The proton conductivity studies of the samples were performed using a Novocontrol impedance spectrometer. The films were sandwiched between gold blocking electrodes and the conductivities were measured in the frequency range 0.1 Hz to 1 MHz at 10 ^{o}C intervals. The temperature was controlled with a Novocontrol cryosystem, which is applicable between -100 and 250 ^{o}C.

2.1.7 Thermal Gravimetric Analyzer (TGA)

The thermal stability was determined by thermogravimetric analysis (TGA, Perkin Elmer Instruments model, STA 6000). The TGA thermograms were recorded for 5-10 mg of

powder sample at a heating rate of 10 ^{o}C min. in the temperature range of 30 ^{o}C-900 ^{o}C under nitrogen atmosphere**.**

2.1.8 Differantial Scanning Calorimetry (DSC)

DSC measurements were carried out on a Perkin Elmer Jade model DSC under nitrogen atmosphere and heating-cooling curves were recorded at a rate of 10 ^{o}C/min.

2.1.9 Ultrasonic Horn

Bandelin SONOPULS HD 2200 ultrasonic homogenizer was used with ultrasonic horn with in a range of 10 to 100 % amplitude which produces 20 kHz uniform sonic waves.

2.1.10 GPC

GPC measurements were carried out using a UV S-3702 (SOMA) detector. The eluent, 0.1 M $NaNO_3$–H_2O solution was used with a flow rate of 1 ml/min. Calibration was carried out using a series of poly(ethylene oxide) (PEO) standards.

2.1.11 NMR

NMR studies of the samples were performed using a Bruker Avance spectrometer at a Larmor frequency of 176.06 MHz. All spectra were recorded with 1ms CP contact time, 15 kHz MAS frequency and 2 s relaxation delay time. NMR spectra of the samples were recorded at ~305 K.

2.2 Procedures

2.2.1 Synthesis of Fe_3O_4 NP's

All chemicals were obtained from Sigma-Aldrich, Merck and Fluka as analytical grade and used without any further purification.

2.2.1.1 Hydrothermal route

Iron acetate, $Fe(CH_3COO)_2$, (0.5g) was dissolved in a 20 ml. of deionized water and pH was adjusted at 10.5 by adding 1 M aqueous TMAOH (tetramethyl ammonium hydroxide) under vigorous stirring. This process resulted in the formation of a gel, i.e. $Fe(OH)_2$ gel. Then the reaction mixture was loaded and sealed into a 50 ml capacity Teflon lined autoclave (Figure 2.1) followed by a uniform heating at 180 °C for 8 h. Afterwards the autoclave was

cooled to room temperature in air. Precipitates were filtered and washed with distilled water and ethanol three times, followed by drying at 80 ^{o}C for 4h.

Figure 2.1 Autoclaves used for hydrothermal synthesis.

2.2.1.2 Surfactant-assisted co-precipitation route

2.2.1.2.1 Coating by L-lysine as aminoacid

To an aqueous solution of of Fe(III), $FeCl_3.2H_2O$, and Fe(II) salts, $FeCl_2.4H_2O$, with the molar ratio of 2Fe(III):1Fe(II), L-lysine solution, L-lysine chloride salt, (with the molar ratio of 4) was added and final solution was mixed at 40 ^{o}C for 15 min. Then 4 M ammonium hydroxide, NH_4OH, solution was added till the pH of the solution raised to ~11 at which a black suspension was formed. This suspension was then refluxed at 80 ^{o}C for 6 h, under vigorous stirring and Ar gas. L-lysine coated magnetic particles, LCM, were separated from the aqueous solution by magnetic decantation, washed with distilled water several times and then dried in an oven overnight. This synthesis procedure was represented schematically in Fig.2.2.

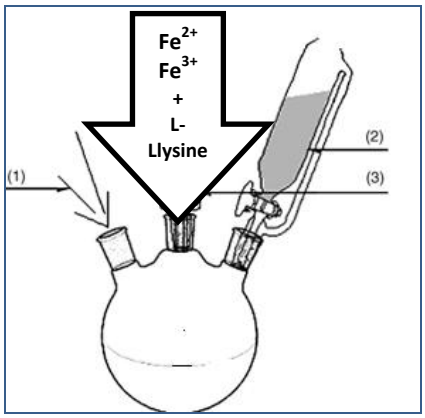

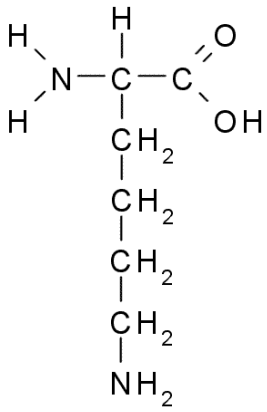

1) Ar gas 2) NH_4OH as precipitator
3) iron salts

a) **b)**

Figure 2.2 a) Scheme of synthesizing Fe_3O_4 NPs by co-precipitation method **b)** L-lysine open structure.

2.2.1.2.2 Coating by salicylic acid

All chemicals ($FeCl_3.2H_2O$, $FeCl_2.4H_2O$, salicylic acid) were used without further purification. To an aqueous solution of a mixture of Fe(III) and Fe(II) salts, salicylic acid solution in the molar ratio 2Fe(III):1Fe(II):4 salicylic acid was added with under vigorous stirring. Then a solution of ammonium hydroxide was added till the pH was raised to ~11 at which a black suspension was formed. This suspension was then refluxed at 90 ^oC for 12 h, under vigorous stirring and Ar gas. Magnetic particles were separated from the aqueous solution by magnetic decantation, washed with distilled water several times and then dried in an oven overnight.

2.2.1.2.3 Coating by alginic acid

To an aqueous solution of a mixture of Fe(III) and Fe(II) salts, alginic acid $(C_6H_8O_6)_n$ (molar mass 10,000 - 600,000) solution in the molar ratio $2FeCl_3.2H_2O$:$1FeCl_2.4H_2O$:4 alginic acid were mixed under vigorous stirring. Then 2M NaOH solution was added to this mixture untill the pH of the mixture raised to ~11 at which a black suspension was formed. This suspension was then refluxed at 90 ^oC for 12 h, under vigorous stirring and Ar gas. Magnetic particles were separated from the aqueous solution by magnetic decantation, washed with distilled water several times and then dried in an oven overnight.

2.2.1.3 Direct ultrasonic-assisted route

The 50/50 (v/v) ethanol and water solution was prepared and bubbled for 30 min with Ar gas. $Fe(OH)_2$ precipitate was obtained by mixing a 0.01mol/L $Fe(ac)_2$ and ethanol-water solution (200 ml) without pH adjustment. The $Fe(OH)_2$ precipitate was irradiated by an ultrasonic horn with 50 % amplitude (Fig.2.3) in an open air at 50ºC. After the synthesis, the precipitated magnetite was centrifugally separated and washed by deionized water for two times, then dried at 50ºC for 2h.

Figure 2.3 The ultrasonic homogenizer for used sonochemical synthesis.

2.2.1.4 Preparation of magnetite (Fe_3O_4) - Poly(1-vinyl-1,2,4-triazole) (PVTri) nanocomposite

Sonochemically synthesized 0.1 g Fe_3O_4 NPs (Section 2.2.1.3) and 0.2 g PVTri (which was synthesized in our laboratory) were added into 50 ml water and stirred at room temperature for 8 h under Ar gas to disperse Fe_3O_4 NPs. Then the reaction mixture was filtered and rinsed with distilled water for several times and ethanol for once. Finally, the obtained brown-black powder was dried in vacuum at 40 °C for 6 h.

2.2.2 Synthesis of Mn_3O_4 NP's

2.2.2.1 Ionic liquid assisted route (Green Chemistry)

Ionic liquid (1-n-butyl- 3-methylimidazolium hydroxide), [BMIM]OH was prepared according to literature [94]. $Mn(NO_3)_2 \cdot 4H_2O$ was added into 2.0 g of [BMIM]OH at room

temperature. Then 4 ml 2M NaOH solution was added to this final solution, and 5 ml H_2O_2 (70% v/v) was dropped within 30 min. The brown product was separated by centrifugation, washed with deionized water and absolute ethanol thereafter dried in vacuum overnight.

2.2.2.2. Hydrothermal route

2.2.2.2.1 Hydrothermal route with TMAOH/NaOH

Manganese acetate, $Mn(CH_3COO)_2$, (0.5g) was dissolved in a 20 ml of deionized water and pH was adjusted to 10.5 by adding either 1 M NaOH solution or 1 M aqueous TMAOH (tetramethyl ammonium hydroxide) under vigorous stirring. This process resulted in the formation of a gel, i.e. $Mn(OH)_2$ gel. Then the reaction mixture was loaded and sealed into a 50 ml capacity Teflon lined autoclave followed by a uniform heating at 180 °C for 8 h. Afterwards the autoclave was cooled to room temperature in air. Precipitates were filtered and washed with distilled water and ethanol three times, followed by drying at 80 ^oC for 4h. The flow chart of this synthesis was presented in Fig.2.4.

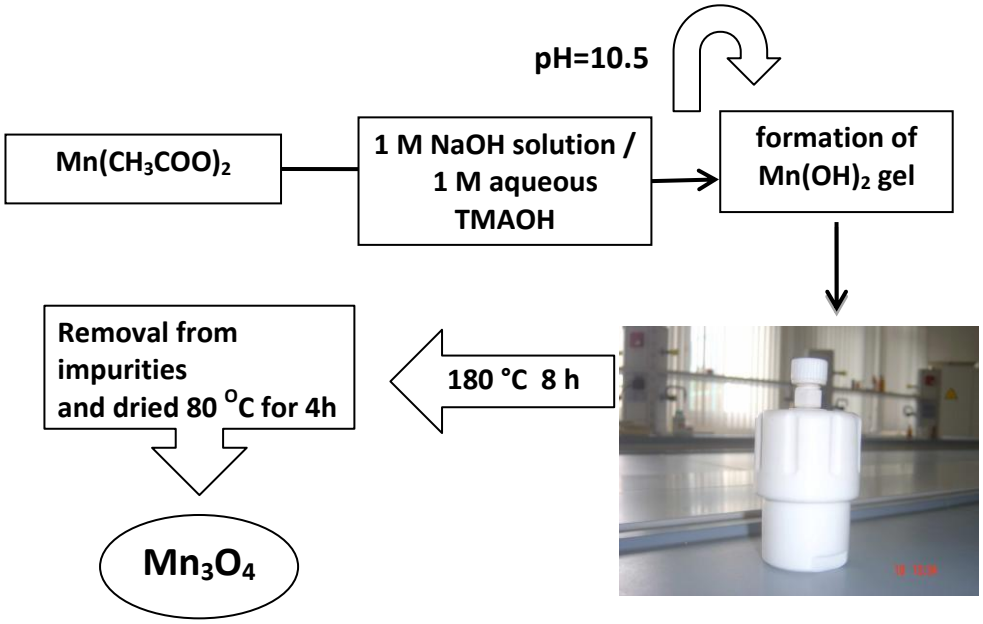

Figure 2.4 Flow chart of experimental procedure for Hydrothermal synthesis of Mn_3O_4.

2.2.2.2.2 Hydrothermal route with H_2O_2

The synthesis consists of two steps: **(1)** preparation of $Mn(OH)_2$ gel by conventional process; **(2)** gel oxidation by H_2O_2 under hydrothermal treatment. In a typical synthesis, 0.04 mol $MnSO_4 \cdot H_2O$ was dissolved in 100 ml distilled water, then, excessive amounts of amonia solution was added and stirred during the formation of $Mn(OH)_2$ gel. The gel was filtered using vacuum filtration and washed by distilled water for several times. Then the fresh wet gel particles were moved into a Teflon-lined stainless steel autoclave, finally a certain volume of H_2O_2 solution (volume ratio of H_2O_2 and H_2O was 1:1) was added into the autoclave very slowly until 80% of the total capacity (25 ml). The sealed autoclave was heated to 180 ^oC in 2h and maintained for 24 h, then cooled to room temperature in air naturally. Precipitates were filtered and washed with distilled water and absolute ethanol for five times respectively, and lastly dried in vacuum at 70 ^oC for 6 h.

2.2.2.2.3 Hydrothermal route with PVP

$MnSO_4.H_2O$ (2mmol), Na_2SO_3 (4 mmol), and polyvinylpyrrolidone (PVP) (0.2g) were dissolved in 20 ml distilled water, and 2 M NaOH solution (20mL) was added with dropwise into the above solution to obtain black colloids. Then the black colloids were transferred into a Teflon-lined stainless steel autoclave, which was degassed with N_2 gas for half an hour, and then sealed, and heated at 140 ^oC for 12 h. After cooling to room temperature, the black products were filtered off, washed with distilled water and absolute ethanol several times, and dried at 50 ^oC for 4 h in vacuum.

2.2.2.3 Egg-white (ovalbumin) assisted route

Experimental procedure for egg-white (ovalbumin) assisted Mn_3O_4 is given in Fig.2.5. Firstly, water–egg white mixture was prepared (3:2 volume ratio). 60 ml of egg white was stirred with 40 ml deionized water with vigorously at room temperature until a homogeneous solution was obtained. Subsequently, stoichiometric amount of $Mn(ac)_2$ and $Mn(acac)_3$ (with the molar ratio of 1:2) were added slowly into egg white–water solution. During addition of Mn salts the solution was stirred magnetically at room temperature for 2 h to obtain a clear solution. Throughout the whole process, no pH adjustment was necessary as the pH of the solution was measured as _9. Then the yellow–orange mixed solution was evaporated by heating at 80 ^oC for several hours until a dried gel precursor was obtained. The dried mass was crushed into powder using a mortar and pestle and then calcined in a box-furnace at 800 ^oC 3 h in air.

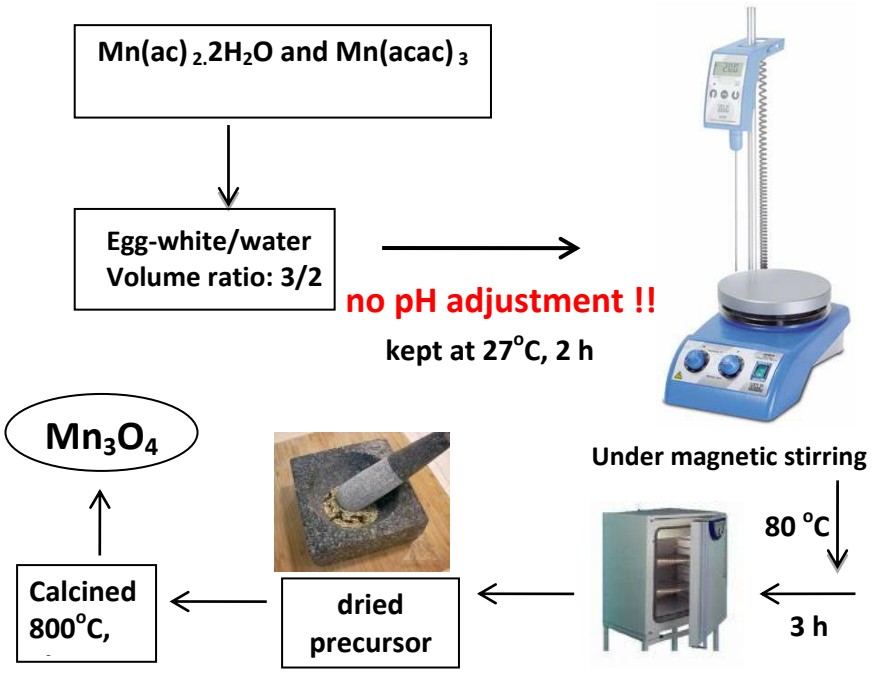

Figure 2.5 Flow chart of experimental procedure for egg-white (ovalbumin) assisted Mn_3O_4.

2.2.2.4 Direct ultrasound-assisted route and capping with CTAB

The mixed solvents of anhydrous ethanol and distilled water were prepared at 20/80 by volume and bubbled for 30 min with Ar gas. $Mn(OH)_2$ precipitate was obtained by mixing a 0.01mol/L $Mn(ac)_2$ ethanol-water solution (200 ml) without pH adjustment. The $Mn(OH)_2$ precipitate was irradiated by an ultrasonic horn (50% amplitude) in an open air. After the synthesis, the wet precipitate was centrifugally separated and washed by deionized water for two times, then dried at 50ºC for 2h.

0,5 g sonochemically as-synthesized sample of Mn_3O_4 in 150 ml distilled water was placed in a 250 ml beaker and the pH was adjusted to about 9.0 with 1M NaOH. To prepare the CTAB coated Mn_3O_4 mixed hemimicelles assemblies, 1 g CTAB were added into the sample solution. The mixture was sonically agitated for 15 min to thoroughly suspend the NPs, then allowed to stand for 10 min. The Mn_3O_4 NPs were filtered and washed with ethanol, then dried 50ºC in vacuum.

2.2.2.5 Synthesis of PANI/Mn_3O_4 nanocomposites

In a typical synthesis experiment, 0.1 g Mn_3O_4 NPs and 0.2 g CTAB were added into 50 ml water and sonicated at room temperature for about 3 h to disperse Mn_3O_4 NPs. 1 g aniline monomer was then dissolved in above suspension and stirred for 1 h. After the temperature of the suspension was adjusted to 0–5 °C, a 30 mL precooled KPS solution was

added dropwise into it with constant stirring to initiate the polyreaction. When KPS solution was added, some heavy floccular deposition appeared instantly. The reaction was carried out at 0-5 °C for another 8 h. Then the reaction mixture was filtered and rinsed with distilled water for several times and methanol for once. Finally, the obtained black powder was dried in vacuum at 40 °C for 24 h.

2.2.3 Synthesis of Co_3O_4 NP's

2.2.3.1 Egg-white (ovalbumin) assisted route

$Co(ac)_2 \cdot 4H_2O$ and $Co(acac)_3$ and freshly extracted egg white (ovalbumin) were used as the starting materials. 40 mL of egg white was first mixed with 40 mL deionized water with vigorous stirring at room temperature until a homogeneous solution was obtained. Subsequently, 0.5 g of $Co(ac)_2 \cdot 4H_2O$ and 0.72 g of $Co(acac)_3$ (a mole ratio corresponding to the nominal composition of Co^{2+} : Co^{3+} ratio of 1:2) were added slowly to the egg white solution with vigorous stirring for 2 h to obtain a well-dissolved solution. Throughout the whole process described above, no pH adjustment was made as the pH was measured around ~9.6. Then, the mixed solution was evaporated by heating in an oven at 80 ^oC for 3h until a dried precursor was obtained, crushed into powder and then was calcinated at 800 ^oC for 3 h.

2.2.3.2 Hydrothermal route with PVP

$CoSO_4.7H_2O$ (2 mmol), Na_2SO_3 (4 mmol), and PVP (0.2 g) were first dissolved in 20 ml distilled water, and 0.2 M NaOH solution (20 mL) was added drop-wise to the above solution to obtain black colloids. Then the black colloids were transferred into a Teflon-lined stainless steel autoclave, which was degassed with N_2 gas for half an hour, and then sealed, and heated at 140 ^oC for 12 h. After cooling to room temperature, the black product was filtered off, washed with distilled water and absolute ethanol several times, and dried at 50 ^oC for 4 h in vacuum.

CHAPTER 3

RESULTS AND DISCUSSIONS

3.1 Fe_3O_4 analysis

3.1.1 Fe_3O_4 NPs by hydrothermal route

3.1.1.1 XRD analysis

Phase investigation of the crystallized product was performed by XRD and the diffraction pattern is presented in Figure 3.1. The XRD pattern indicates that the product is magnetite, Fe_3O_4, and the diffraction peaks are broadened owing to very small crystallite size of the product. All of the observed diffraction peaks are indexed by the cubic structure of Fe_3O_4 (JCPDS no. 19-629) revealing a high phase purity of iron oxide.

The lattice parameter "*a*" for the synthesized iron oxide NPs was refined as 8.388 ± 0.001 Å and line profile fitting is shown in Figure 3.1, was fitted for observed eleven peaks with the following miller indices: (220), (311), (222), (400), (422), (333), (440), (620), (533), (444), and (642). The average crystallite size, *D* and σ, was obtained as 20 ± 13 nm as a result of this line profile fitting.

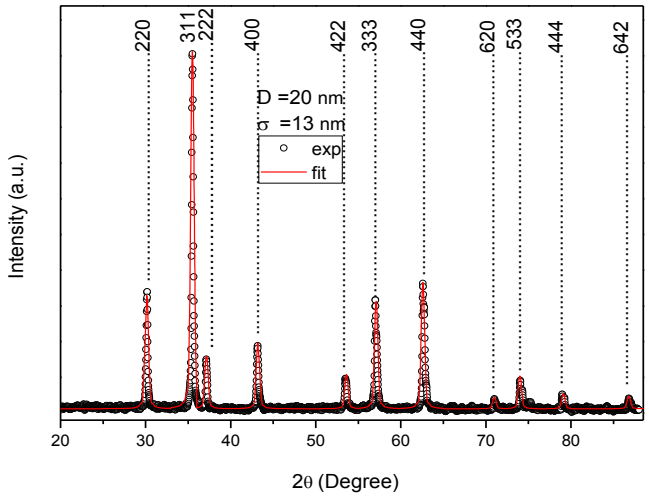

Figure 3.1 XRD powder pattern and line profile fitting of hydrothermally synthesized Fe_3O_4.

3.1.1.2 FTIR analysis

The FTIR spectra of as synthesized Fe_3O_4 nanocrystals are shown in Fig.3.2. As prepared powder presents characteristic peaks that are exhibited by the commercial magnetite powder: metal-oxygen band, υ_1, observed at 580 cm^{-1} corresponds to intrinsic stretching vibrations of the metal at tetrahedral site (Fe_{tetra}↔O), whereas metal-oxygen band, υ_2,observed at 446 cm^{-1}, is assigned to octahedral-metal stretching (Fe_{octa}↔O) [95,96].

Two broad peaks at 3400 and 1650 cm^{-1} are due to the presence of a small amount of adsorbed water and O-H streching. The peak at 1420 cm^{-1} is due to the presence of N-H groups on the surface of the particles which is indicated surfactant effect of TMAOH molecules.

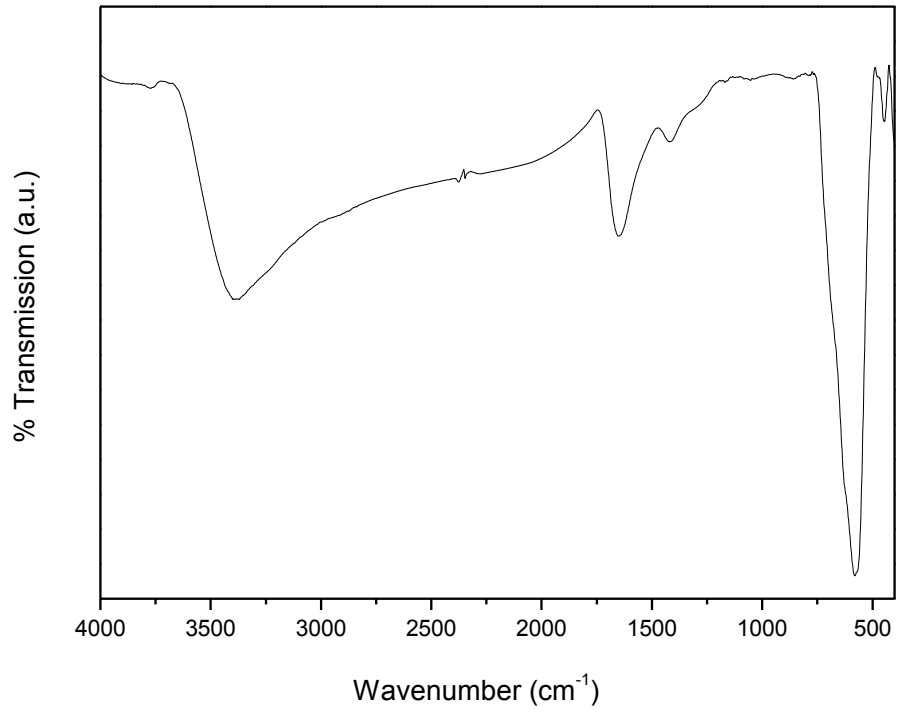

Figure 3.2 FTIR spectra of hydrothermally synthesized Fe_3O_4 NPs.

3.1.1.3 TEM analysis

TEM micrograph of hydrothermally synthesized Fe_3O_4 NPs is given in Fig. 3.3a and the particle size distribution is shown in Fig. 3.3b. Size distribution histogram is obtained by measuring at least 200 NPs and is fitted by using a log-normal function as described in detail in ref 97. An average size, $D_{TEM/log\text{-}normal}$, of 371 nm ± 0,2 was obtained for iron oxide NPs.

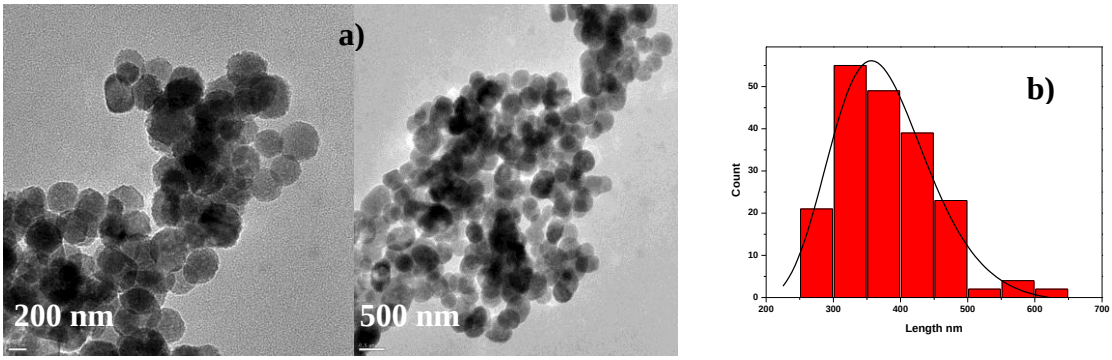

Figure 3.3 a) TEM micrograph of hydrothermally synthesized Fe_3O_4 NPs, and **b)** calculated histogram from several TEM images with log-normal fitting.

3.1.2. Surfactant-assisted co-precipitation route

3.1.2.1 Coating by L-lysine as aminoacid[1]

3.1.2.1.1 XRD analysis

Phase investigation of the crystallized product was performed by XRD and the diffraction pattern is presented in Fig. 3.4. The XRD pattern indicates that the product mostly consists of magnetite, LCIO (L-lysine coated iron oxide) and the diffraction peaks are broadened owing to very small crystallite size. All of the observed diffraction peaks are indexed by the cubic structure of Fe_3O_4 (JCPDS no. 19-629) revealing a high phase purity of magnetite. The following reaction is suggested for the formation of magnetite:

$$Fe^{2+}_{(aq)} + 2Fe^{3+}_{(aq)} + 8\ OH^{-}_{(aq)} \rightarrow Fe_3O_{4\ (s)} + 4\ H_2O$$

The lattice parameter "*a*" for the synthesized iron oxide NPs was refined as 8.391 ± 0.002 Å and the mean size of the crystallites was estimated from the diffraction pattern by line profile fitting method. The line profile, shown in Fig. 3.4. was fitted for observed seven peaks with the following miller indices: (111), (220), (311), (400), (422), (511), (440). The average crystallite size, *D* and σ, was obtained as 8 ± 4 nm as a result of this line profile fitting.

[1]Z. Durmus, H. Kavas, M. S. Toprak, A. Baykal, T.G. Altınçekiç, A. Aslan, A. Bozkurt, S.Cosgun **"L-lysine coated iron oxide nanoparticles: Synthesis, structural and conductivity characterization",** doi:10.1016/j.jallcom.2009.04.103

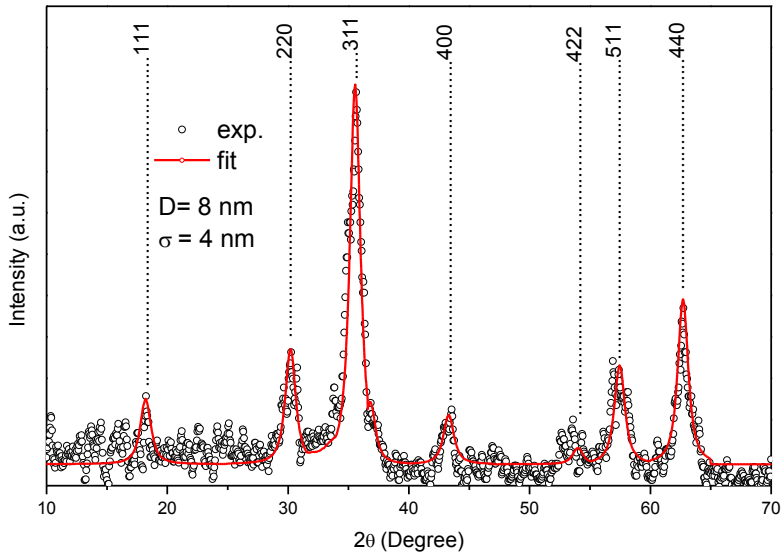

Figure 3.4 XRD powder pattern and line profile fitting of LCIO NPs.

3.1.2.1.2 FTIR analysis

FTIR spectra of iron oxide, L-lysine and LCIO NPs are given in Fig. 3.5. The presence of the iron oxide NPs is evidenced by the strong absorbtion bands at around 570 - 590 cm^{-1} that confirm the metal-oxygen streching, present in Fig. 3.5a and 3.5c [98].

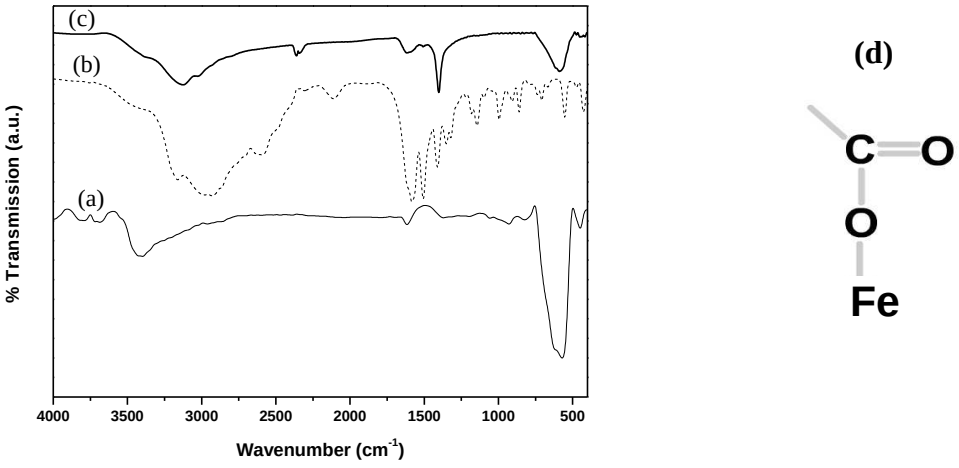

Figure 3.5 FTIR spectra of **(a)** Fe_3O_4 NPs, **(b)** L-lysine and **(c)** LCIO NPs. **(d)** Suggested linkage of L-lysine to Fe_3O_4 NPs surface.

In the spectrum 3.5b the characteristic NH_2 stretching frequencies of L-lysine is observed at ~3400 cm^{-1}, and asymmetric and symmetric stretching frequencies of carboxylate (COO^-) are observed at 1585 cm^{-1} (C=O) and 1402 cm^{-1} (C-O) respectively. In the spectrum for LCIO

(Fig. 3.5c), the vibrations of asymmetric and symmetric stretching of carboxyl anion occurred at 1620 cm^{-1} and 1402 cm^{-1}. The splitting between asymmetric and symmetric stretching of carboxyl group, $\Delta\upsilon(\upsilon_{asymmOCO} - \upsilon_{symOCO})$, is higher than that present in the FTIR spectra of uncoordinated L-lysine (Fig. 3.5b) which indicate the unidentate coordination between the carboxyl anions and the metal ions [99] as schematically depicted in Fig. 3.5d. The peak at ~3400 cm^{-1} is assigned to N-H stretching [100] in agreement with the vibrations of some aminocarboxylates and carboxylates reported earlier [101]. According to these results, FTIR analyses suggest that L-lysine remains chemisorbed on the surface of iron oxide.

3.1.2.1.3 TEM analysis

A typical TEM micrograph of LCIO NPs is shown in Fig. 3.6a and the particle size distribution is presented in Fig. 3.6b. Size distribution histogram is obtained by measuring at least 300 NPs and is fitted by using a log-normal function as described in detail in ref 18. An average size, $D_{TEM/log\text{-}normal}$, of ~114 nm was obtained for iron oxide NPs. Crystallite size obtained from XRD line profile fitting is smaller than the particle size estimated from TEM, revealing the polycrystalline nature of observed NPs.

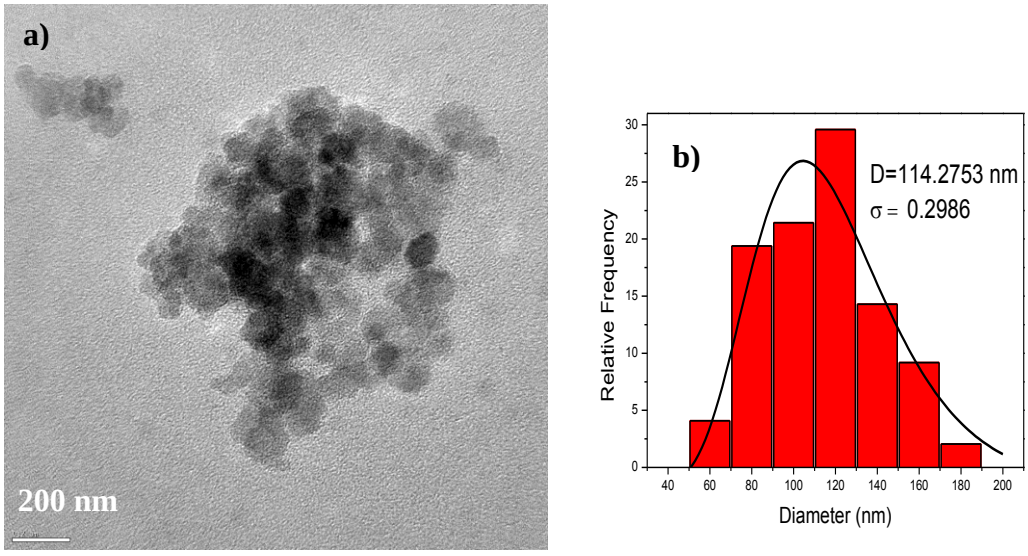

Figure 3.6 (a) TEM micrograph of lysine-coated iron oxide (LCIO) NPs, and **(b)** calculated histogram from several TEM images with log-normal fitting.

3.1.2.1.4 Particle Size and Zeta Potential Analysis

Particle size analysis performed using dynamic light scattering, DLS method revealed bimodal distribution of NPs with 95% of the particles centered around 330 nm as shown in

Fig. 3.7a. This is probably due to the aggregation of three-to-four LCIO NPs during magnetic separation.

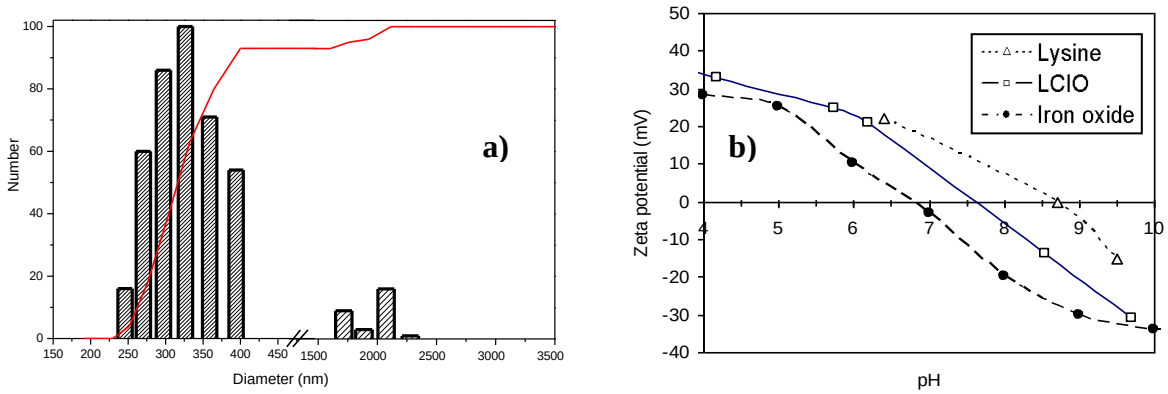

Figure 3.7 (a) Particle size distribution of LCIO NPs using DLS method and **(b)** zeta potential analysis of L-lysine, uncoated Fe_3O_4 NPs and LCIO NPs.

L-Lysine, iron oxide NPs in bare form and after L-lysine coating are also analyzed for their surface charge and results are presented in Fig. 3.7b. Iron oxide NPs exhibit a point of zero charge, pzc, at slightly below pH 7. This value indicates that iron oxide NPs will agglomerate at phsiological pH. L-lysine exhibits a pzc value of 8.7. This is due to the fact that each lysine molecule bears two amine groups and a carboxyl group that are protonated at low pH, rendering the overall charge positive. As the pH increases carboxyl group will loose the attached hydrogen, get negatively charged and thus reduce the overall charge. Afterwards, amines will get deprotonated at various pH values that will cause the surface potential to cross from zero to the negative charge region which takes place at pH 8.8. Upon L-lysine coating pzc value of iron oxide shifts to pH of 7.6, thus making LCIO NPs positively charged at physiological pH due to the positively charged amines groups of L-lysine coating. The fact that the pzc for LCIO NPs is observed at ~1 pH unit lower than that observed for pure L-lysine is most probably due to a partial surface coverage of iron oxide NPs by L-lysine.

3.1.2.1.5 Thermal Analysis

Thermogravimetric analysis curves of iron oxide (Fe_3O_4), L-lysine and LCIO are presented in Fig. 3.8. Weight loss scale allows a quantitative comparison of degradation behavior of samples. Iron oxide shows no weight loss in the temperature range of TG

analysis. On the other hand, the two-stage degradation is seen in the TGA curves of both L-lysine and LCIO samples. L-lysine also yields about 5 wt% residue which indicates coke formation due to pyrolytic conditions under nitrogen. Derivative weight loss (DTG) curves of the L-lysine and LCIO are also illustrated in the inset of Fig. 3.8. It seems in the DTG curves that the degradation steps of these two samples are very similar. LCIO sample shows a slight weight change up to 140-150 ^{o}C which is ascribed to the release of physisorbed water, while L-lysine exhibits a considerable thermal stability up to 250 ^{o}C. Degradation of L-lysine over the iron oxide begins at a much lower temperature. This behavior could be originated from the fact that iron oxide particles behave as catalysts thus reducing the degradation temperature of L-Lysine. Moreover, temperature range between degradation onset and offset points on the DTG curves for L-lysine is wider than that for the LCIO. This result might also be attributed to catalytic effects of NPs for the degradation of L-lysine.

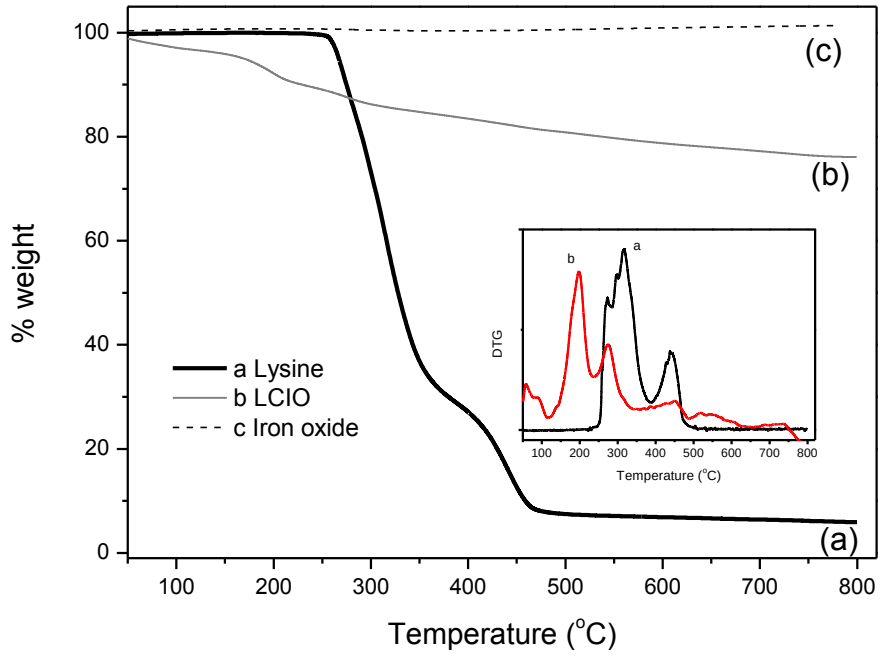

Figure 3.8 TGA thermograms of **(a)** L-lysine, **(b)** LCIO, and **(c)** Fe_3O_4 NPs.

3.1.2.1.6 Electrical properties

3.1.2.1.6.1. AC Conductivity

The effect of L-lysine coating of iron oxide is analyzed in terms of conductivity properties by measuring the frequency dependant permittivity and AC conductivity of L-

lysine, iron oxide and LCIO NPs within 1 Hz - 3 MHz frequency regime in the temperature range of 290 K-420 K [102,103]. Fig. 3.9a shows AC electrical conductivity of iron oxide as a function of frequency. The DC conductivity increases with temperature and reaches to 0.7 mS/cm at 100 ^{o}C. Arrhenius plots (log σ versus $10^4/T$) for iron oxide NPs is shown in Fig. 3.9b. Ferrites' semiconducting nature, the increase of conductivity with increasing temperature, has been observed in 1 Hz- 3 MHz frequency range and reported earlier in Ref 102. The conductivity of iron oxide is independent of temperature at T < 70 ^{o}C above which it linearly increases with temperature. The activation energy can be obtained from the slope of the Arrhenius curves by using the following equation [104]:

$$\tilde{\sigma} = \sigma_o + \exp(E_\sigma / kT) \qquad (1)$$

where σ_o a temperature-dependant is term and E_σ represents the AC activation energy of the conduction mechanism. The AC activation energies for iron oxide were obtained between 0.048-0.041 eV (1Hz-3MHz) which is close to the activation energy of iron oxide reported earlier as 0.052 eV [21]. There is also a magnetic transition region in the temperature range of 70 ^{o}C - 90 ^{o}C for both iron oxide and LCIO NPs.

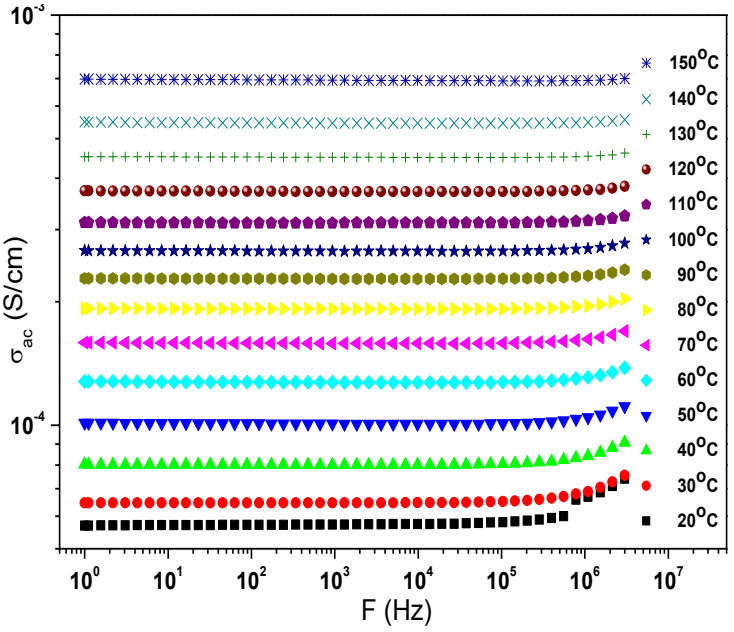

a)

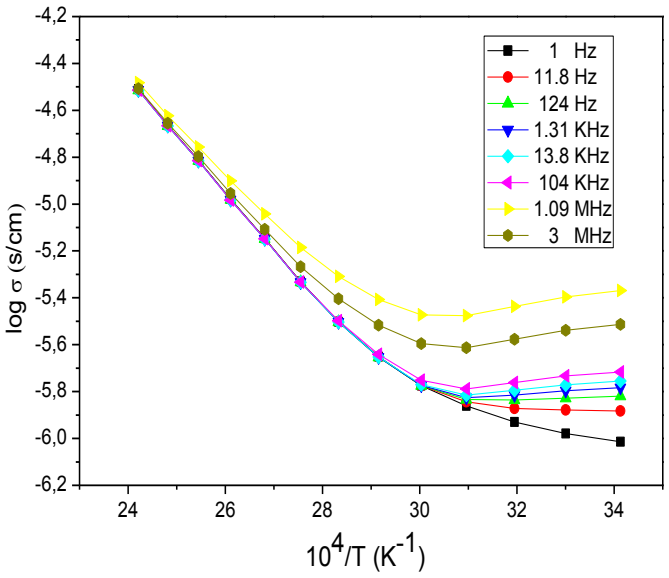

b)

Figure 3.9 AC conductivity of Fe_3O_4 NPs versus **(a)** frequency, and **(b)** 10000/T (K).

The AC conductivity, σ_{ac} (ω), versus frequency for L-lysine at various temperatures is presented in Fig. 3.10. The observed trend is typical for ion conducting organic material. The DC conductivity of the sample was derived from low frequency region by fitting the data.

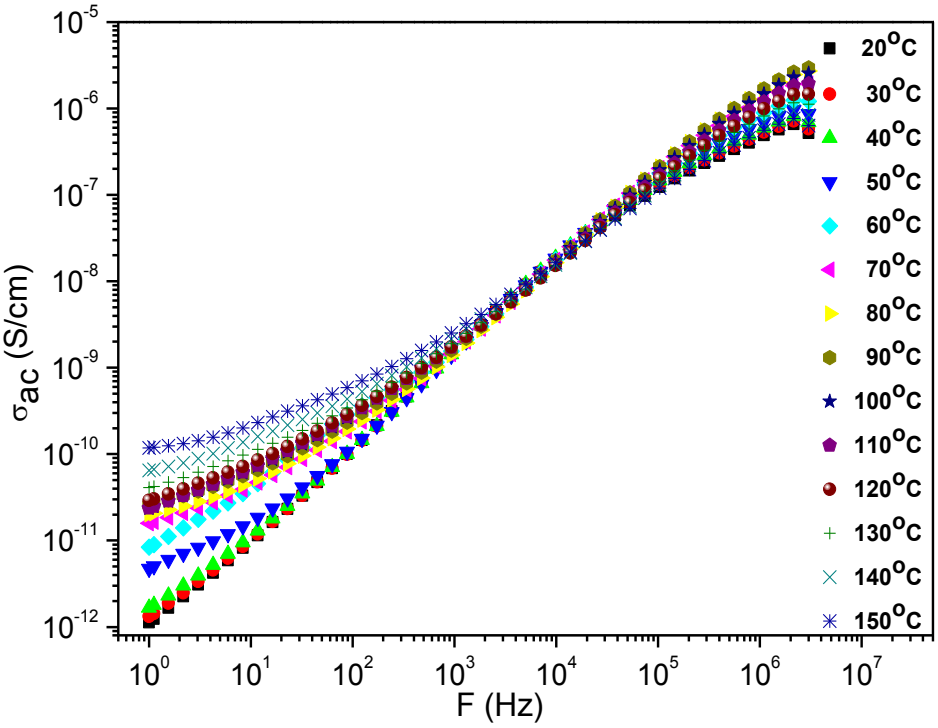

Figure 3.10 AC conductivity of L-lysine as a function of frequency.

The σ_{ac} of LCIO curves with respect to frequency at various temperatures are shown in Fig. 3.11a. Curves consist of the irregularities at lower temperatures and frequencies (i.e., f<100 Hz below 60 ^{o}C) that mainly correspond to electrode polarizations [103]. The conductivity plateau regions, which are well developed at lower frequencies and above 60 ^{o}C, broaden toward higher frequencies at higher temperatures. The σ_{ac} curves as a function of temperature for LCIO NPs have two different regimes as observed for iron oxide (Fig. 3.11b). The temperature for the regime change is also at ~70 ^{o}C for LCIO. The activation energies calculated by using Equation 1 was found between 0.050 and 0.044 eV (1 Hz-3 MHz). The AC activation energy values of LCIO NPs are bigger than that of iron oxide, as expected, due to insulating L-lysine coating.

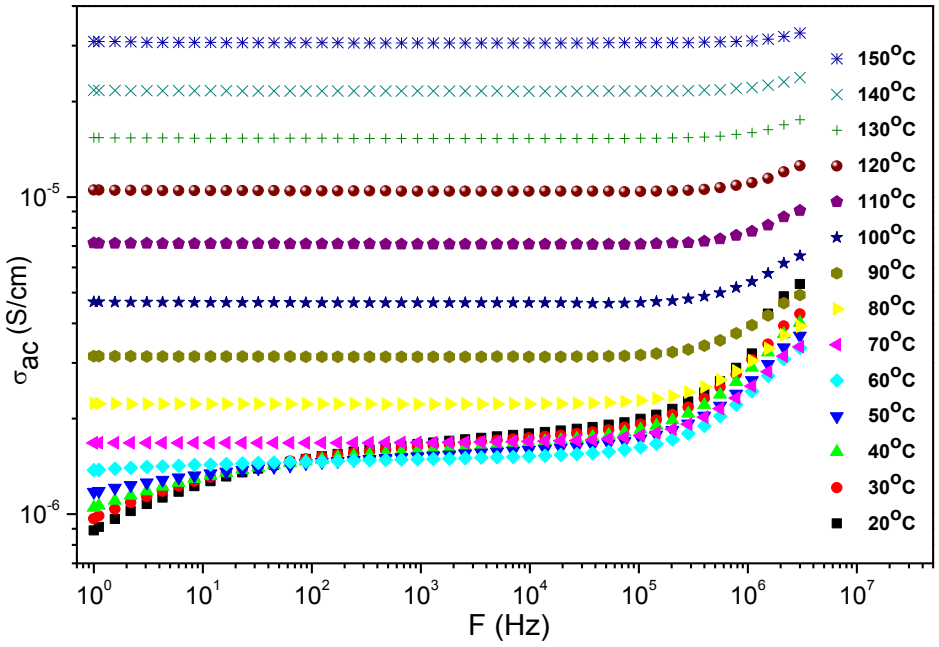

a)

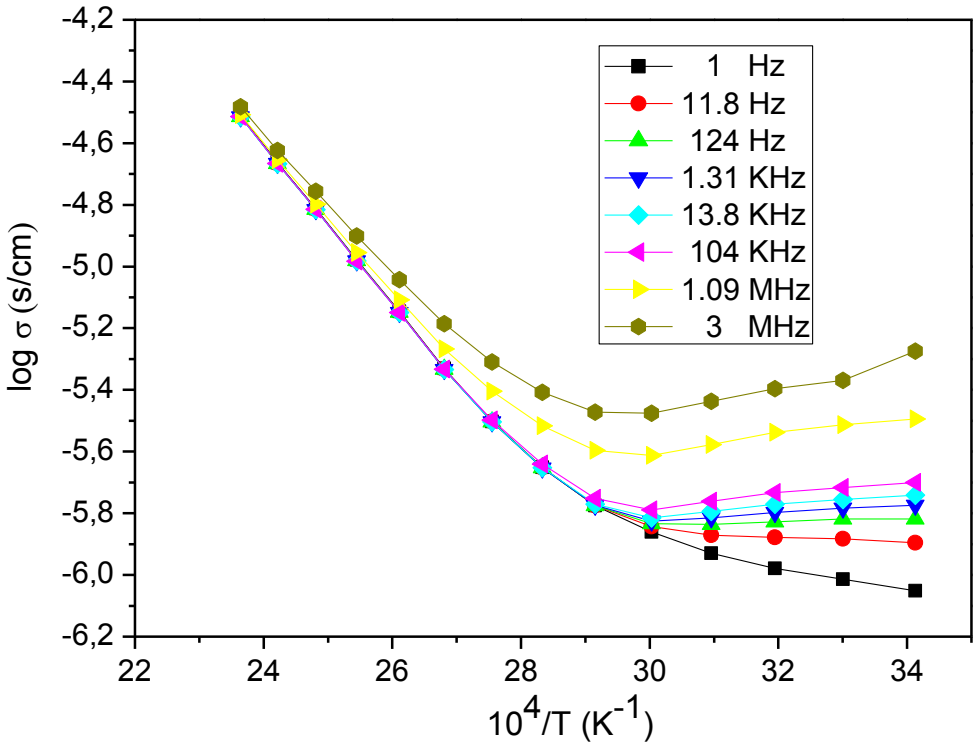

(b)

Figure 3.11 AC conductivity of LCIO versus **(a)** frequency, and **(b)** 10000/T (K).

3.1.2.1.6.2. DC conductivity

The ionic or vacant sites charge carriers give low mobility systems such as ferrites and the hopping process causes the major conduction. Electron hopping takes place between the neighboring iron cations with two and three valence. In this process, drift mobility of charge carriers increases by increasing temperature, and causes a decrease in DC resistivity. The parameters affecting the conductivity in ferrites, porosity, chemical composition, particle size [105,106] and cation distribution [107] have been explained in earlier reports, however the effect of lysine coating on ferrites' conductivity has not been studied yet. In this study, it is found that the resistivity of iron oxide NPs increases with lysine coating. The DC resistivity vs 10^4/T curves are shown in Fig. 3.12. While iron oxide has smooth changes in its resistivity curve, the LCIO has sharp changes in magnetic transformation region at ~70 ^{o}C. Watanabe et al. [103] reported that the single crystals of iron oxide have magnetic transformation in the temperature range of 70-190 ^{o}C. Evaluation of the slope of the curves before and after magnetic transformation showed that the DC activation energies of iron oxide exhibit a little difference while LCIO's activation energies exhibit big differences. The slopes of temperature dependant resistivity curves of iron oxide and LCIO at high temperature give the DC

activation energies as 0.22 eV and 0.43 eV respectively. The coating effect by L-lysine increases the activation energy as a factor of two. These values are in-agreement with DC activation energy of iron oxide reported by Ref 102.

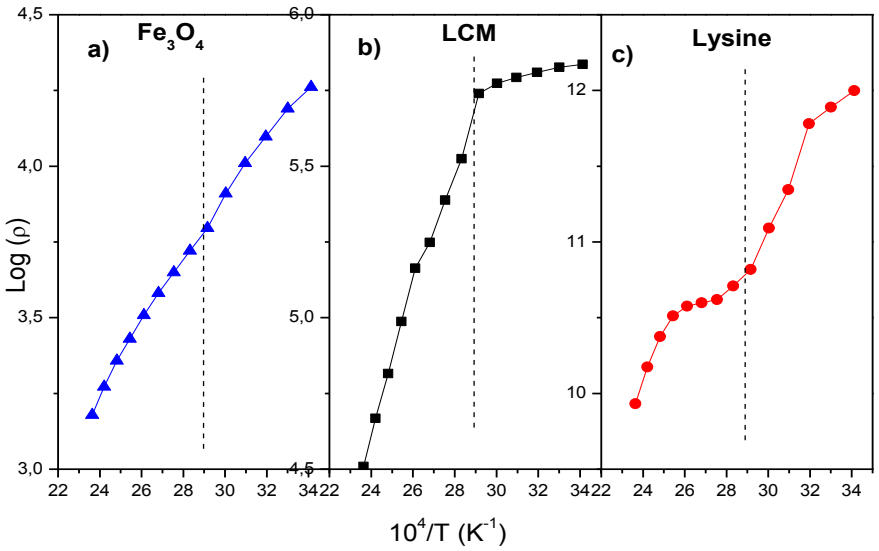

Figure 3.12 Total DC resistivity of **(a)** iron oxide, **(b)** LCIO, and **(c)** L-lysine.

3.1.2.2 Coating by salicylic acid

3.1.2.2.1 XRD Analysis

The XRD pattern given in Fig.1 indicates that the product is magnetite, Fe_3O_4, and the diffraction peaks are broadened owing to very small crystallite size. All of the observed diffraction peaks are indexed by the cubic structure of Fe_3O_4 (JCPDS no. 19-629). The lattice constant for each peak of each sample was calculated by using the formula:

$a = d\,(h^2 + k^2 + l^2)^{1/2}$, where h,k, and l are miller indices of the crystal palnes. To determine the exact lattice parameter for each composition (sample), Nelson-Riley method was used. The Nelson-Riley function $F(\theta)$ is given as $F(\theta) = 1/2[(\cos^2\theta / \sin\theta) + \cos^2\theta / \theta]$. The values of lattice constant a_o of all the peaks for a sample was plotted against $F(\theta)$ (not given). Then using a least square fit method exact lattice constant a_o was determined (Table 1). The point where the least square fit straight line cut the *y*-axis (Where $F(\theta) = 0$) is the actual lattice parameter of the composition. The lattice parameter "*a*" for the synthesized iron oxide NPs was refined as 8.391 ± 0.002 Å.

The line profile, shown in Fig. 3.13 was fitted for observed eight peaks with the following miller indices: (111), (220), (311), (222), (400), (422), (511), (440). The average

crystallite size, *D* and σ, was obtained as 13.1 nm ± 6.2 nm as a result of this line profile fitting.

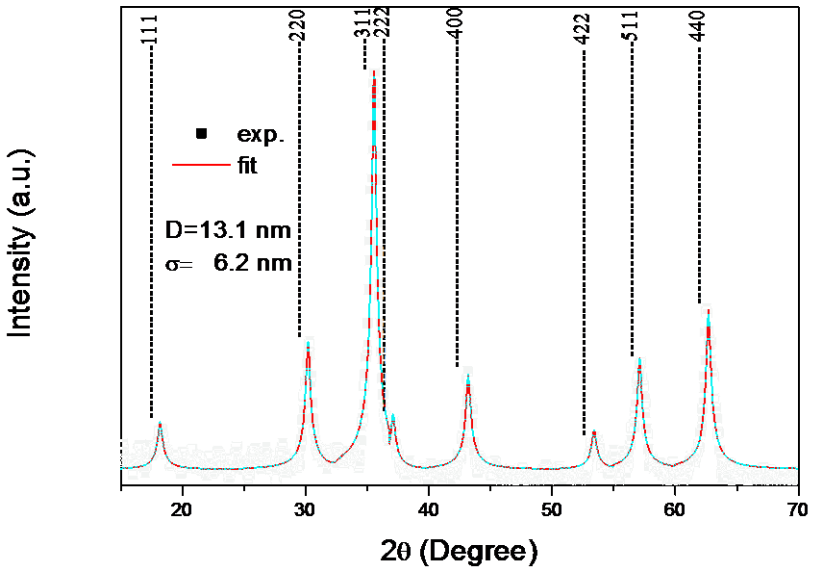

Figure 3.13 X-ray powder diffraction pattern and line profile fitting of salicylic acid coated iron oxide NPs.

3.1.2.2.2 FTIR Analysis

Fig. 3.14 shows the typical FTIR spectrum of **a)** Fe_3O_4 NPs **b)** Salicylic acid coated - Fe_3O_4 nanocomposite **c)** Salicylic acid and **d)** Suggested linkage of salicylic acid to iron oxide surface. In curve (3.14c), two sharp bands at 2924 and 2854 cm^{-1} were attributed to the asymmetric CH_2 stretch and the symmetric CH_2 stretch, respectively. The intense peak at 1662 cm^{-1} was derived from the existence of the C=O stretching band. In the curve (3.14b), the asymmetric CH_2 stretch and the symmetric CH_2 shifted to 2922 and 2852 cm^{-1}, respectively. The surfactant molecules in the adsorbed state were subjected to the field of the solid surface. As a result, the characteristic bands shifted to a lower frequency region which indicated that the hydrocarbon chains in the monolayer surrounding the nanoparticles were in a closed-packed, crystalline state. It is worth to note that the C=O stretch band of the carboxyl group, which was present at 1680 cm^{-1} in the curve (c), spectrum of the pure salycilic acid, was absent in the curve (3.14b), spectrum of the coated nanoparticles. Actually, two binding modes have been suggested for the surface carboxylate bonding [108-110]. In one mode, the carboxylate is connected to the surface through one oxygen atom, and both the symmetric C=O (1441 cm^{-1}) and the asymmetric (1552 cm^{-1}) stretchings were observed [111,112,108].

In the other mode, the carboxylate is bound symmetrically to the surface and only the symmetrical C=O stretching band appears at 1404 cm^{-1} [109,112]. In our case, only one peak at 1415 cm^{-1} which is the symmetric stretching was observed. Therefore, our conclusion is that the both carboxylic acid oxygens are symmetrically bonded to the Fe_3O_4 nanoparticle surface (as shown in Fig.3.14d). These revealed that salycilic acid was chemisorbed onto the Fe_3O_4 nanoparticles as a caboxylate. The presence of the magnetite NPs is evidenced by the strong absorbtion bands at around 570 - 590 cm^{-1} that confirm the metal-oxygen streching [96].

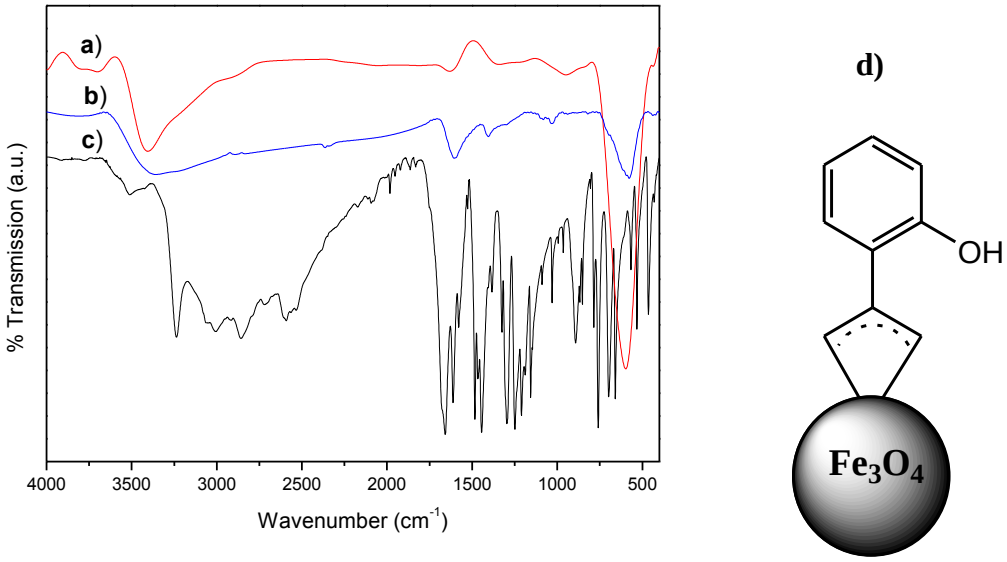

Figure 3.14 FTIR spectra of **a)** Fe_3O_4 NPs **b)** salicylic acid coated - Fe_3O_4 NPs, **c)** salicylic acid and **d)** Suggested linkage of salicylic acid to iron oxide surface.

3.1.2.2.3 TEM Analysis

A typical TEM micrograph of salicylic acid coated -iron oxide NPs is shown in Fig. 3.15a and the particle size distribution is presented in Fig. 3.15b. Size distribution histogram is obtained by measuring at least 300 NPs and is fitted by using a log-normal function. An average size, $D_{TEM/log\text{-}normal}$, of ~20.13 ± 0.23 nm was obtained for iron oxide NPs. Crystallite size obtained from XRD line profile fitting is smaller than the particle size estimated from TEM, revealing the polycrystalline nature of observed NPs.

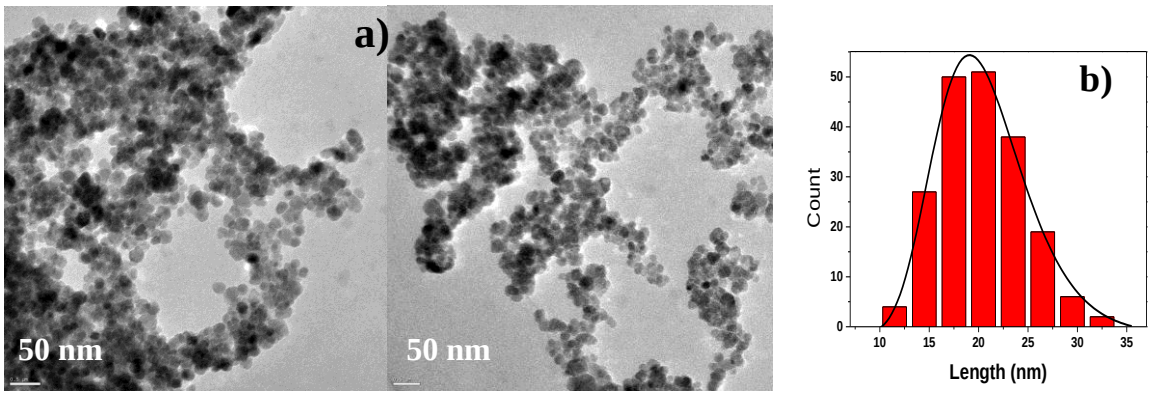

Figure 3.15 (a) TEM micrograph of salicylic acid coated-iron oxide NPs, and **(b)** calculated histogram from several TEM images with log-normal fitting.

3.1.2.2.4 TG Analysis

Thermogravimetric analysis curves of iron oxide (Fe_3O_4), salicylic acid coated-iron oxide and salicylic acid presented in Fig.3.16. Weight loss scale allows a quantitative comparison of degradation behavior of samples. Iron oxide shows no weight loss in the temperature range of TG analysis. For salicylic acid coated-iron oxide (Fig.3.16b), between room temperature and 200 ^{o}C, a weight loss about 2 wt % is attributed to the evaporation of physisorbed water and lossely coordinated water in the interlayer and a weight loss of about 10 wt % in the range of 200-500 ^{o}C is due to the decomposition of salicylic acid.

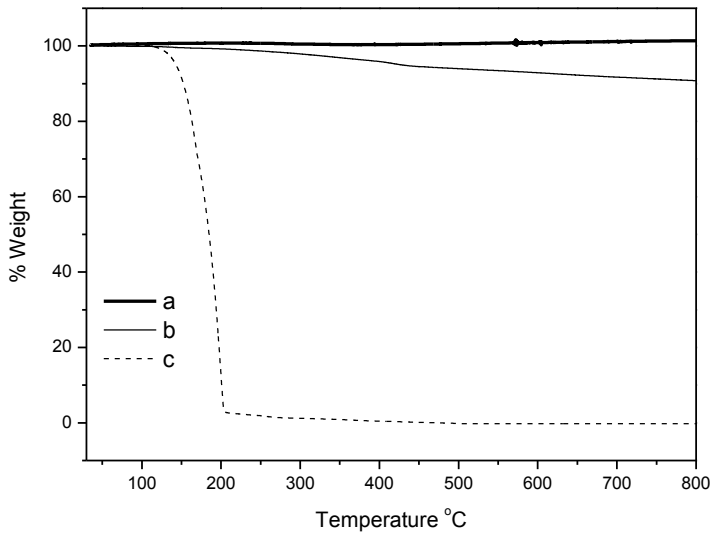

Figure 3.16 TGA thermograms of (**a)** Fe_3O_4 NPs (**b)** salicylic acid coated-iron oxide NPs, and **(c)** salicylic acid.

3.1.2.2.5 Electrical Properties

The σ_{ac} of salicylic acid coated-iron oxide NPs curves with respect to frequency at various temperatures are shown in Fig. 3.17. Curves consist of the irregularities at lower temperatures and frequencies (i.e., f<100 Hz below 60 ^{o}C) that mainly correspond to electrode polarizations [103]. The conductivity plateau regions, which are well developed at lower frequencies and above 60 ^{o}C, broaden toward higher frequencies at higher temperatures.

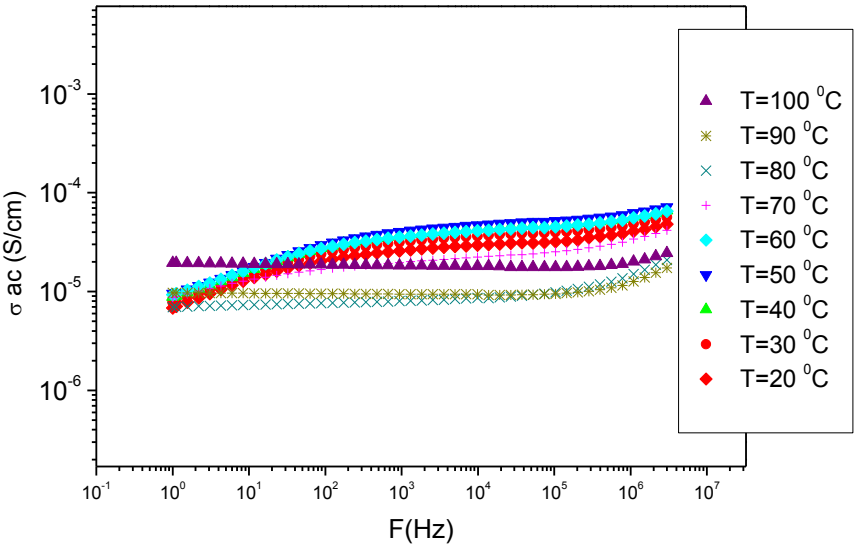

Figure 3.17 AC conductivity of salicylic acid coated-iron oxide NPs versus frequency.

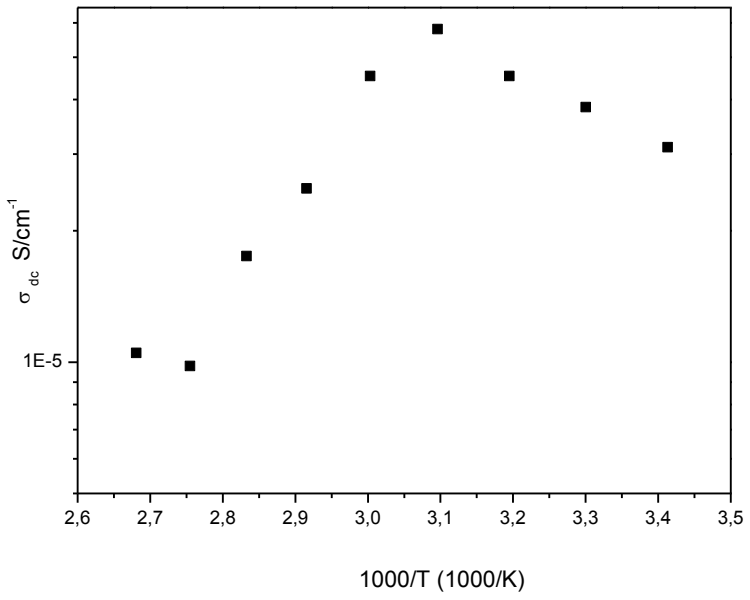

Figure 3.18 DC conductivity of salicylic acid coated-iron oxide NPs versus 1000/T (K).

The complex permittivity parameters of salicylic acid coated-iron oxide NPs ε' and ε'', were presented in Fig. 3.19. The dielectric constants increase with increasing temperature as seen in semiconductors. Thermal energy convert the bound charges to the charge carriers, and increasing charge carrier concentration always gives easy alignment of dipoles in the applied AC electrical field and so increase in dielectric constants. Also by increasing the temperature the mobility of the charge carriers increases.

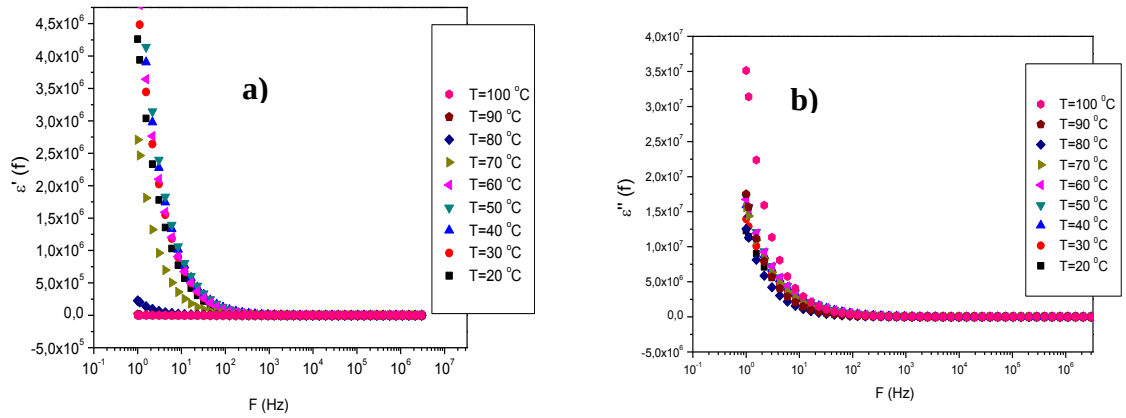

Figure 3.19 a) Real part and **b)** Imaginary part of permitivity as a function of frequency at various temperatures of salicylic acid coated-iron oxide NPs.

3.1.2.3 Coating by using alginic acid

3.1.2.3.1 XRD Analysis

Phase investigation of the crystallized product was performed by XRD and the diffraction pattern is presented in Fig. 3.20. The XRD pattern indicates that the product is magnetite, Fe_3O_4, and the diffraction peaks are broadened owing to very small crystallite size. All of the observed diffraction peaks are indexed by the cubic structure of Fe_3O_4 (JCPDS no. 19-629). The lattice parameter "*a*" for the synthesized iron oxide NPs was refined as 8.366 ± 0.002 Å and was fitted for observed nine peaks with the following miller indices: (111), (022), (311), (400), (224), (333), (044), (026), and (335). The average crystallite size, *D* and σ, was obtained as 9 ± 6 nm as a result of this line profile fitting.

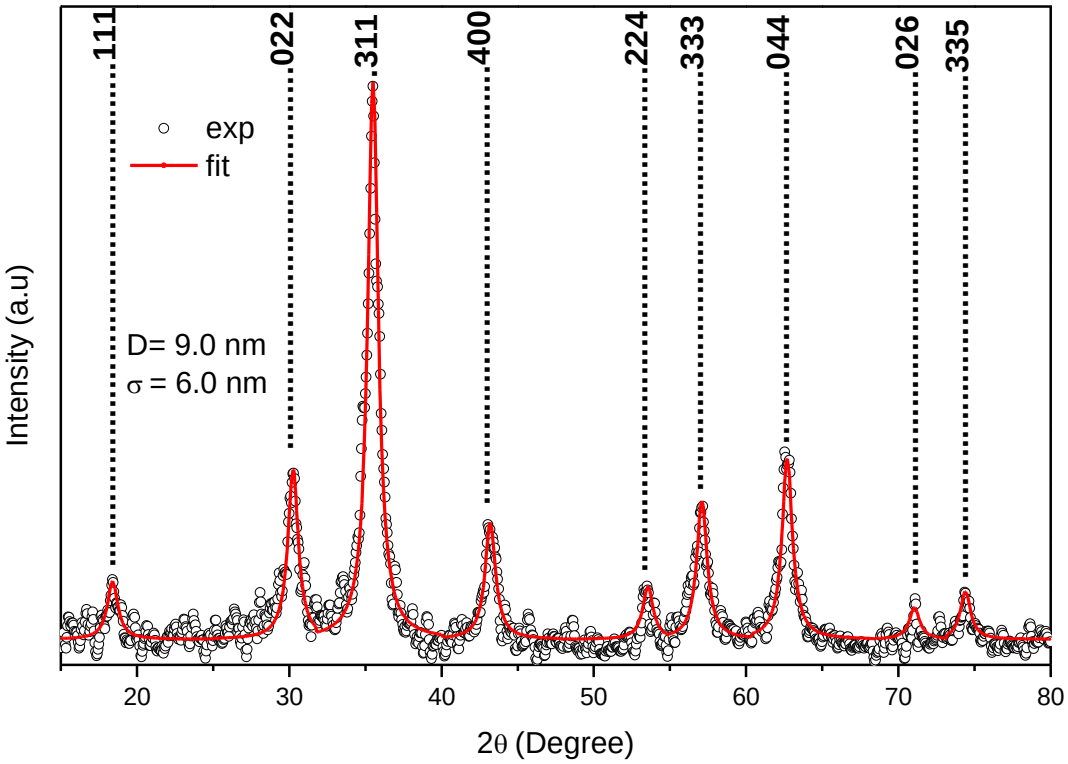

Figure 3.20 XRD powder pattern and line profile fitting of alginic acid coated Fe_3O_4 NPs.

3.1.2.3.2 FTIR Analysis

FTIR spectra of uncoated Fe_3O_4 NPs, alginic acid coated Fe_3O_4 NPs and alginic acid are given in Fig. 3.21. The presence of the iron oxide NPs is evidenced by the strong absorbtion bands at around 570 - 590 cm^{-1} that confirm the metal-oxygen streching, present in Fig. 3.21a and 3.21b [98]. 1247 cm^{-1} and 1419 cm^{-1} represent the C–O–H stretching of carboxylic acid groups of the alginic acid in Fig. 3.21c. A strong absorption appears at 1742 cm^{-1} that belongs to C=O stretching [113], and its shift to lower energies should be due the chemical interaction between the alginic acid molecules and the iron oxide NPs surface. This result represents a strong evidence that this interaction occurs through the C=O groups of the alginic acid [110-112].

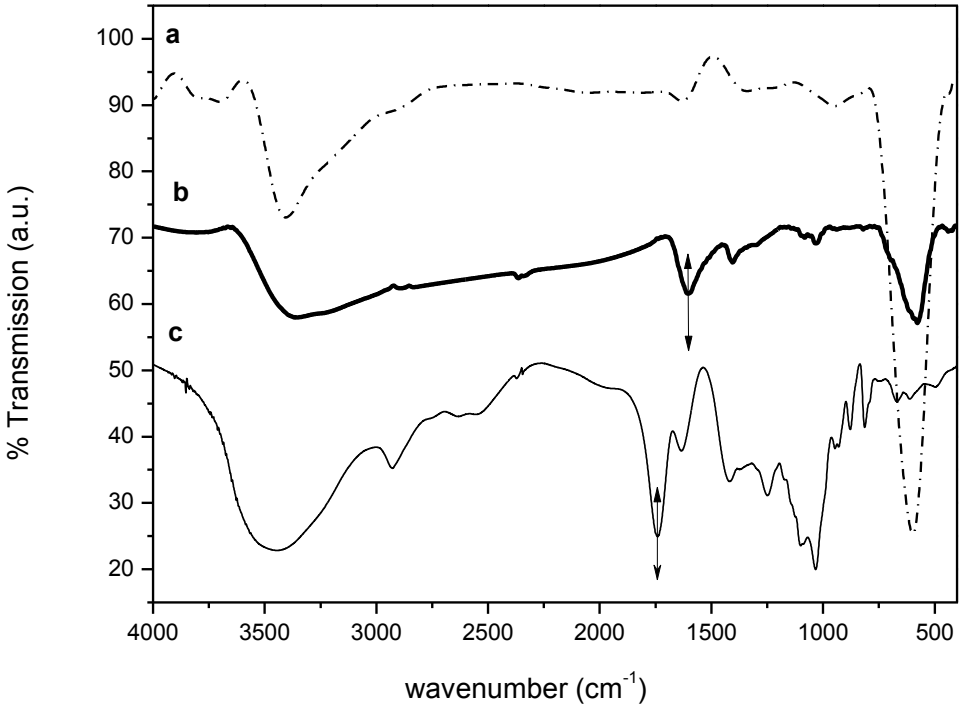

Figure 3.21 FTIR spectra of **(a)** uncoated Fe_3O_4 NPs **(b)** alginic acid coated Fe_3O_4 NPs and **(c)** alginic acid.

3.1.2.3.3 TEM Analysis

Morphology of Fe_3O_4 particles were also investigated by TEM and a micrograph is presented in Fig. 3.22 which shows a strong agglomeration.

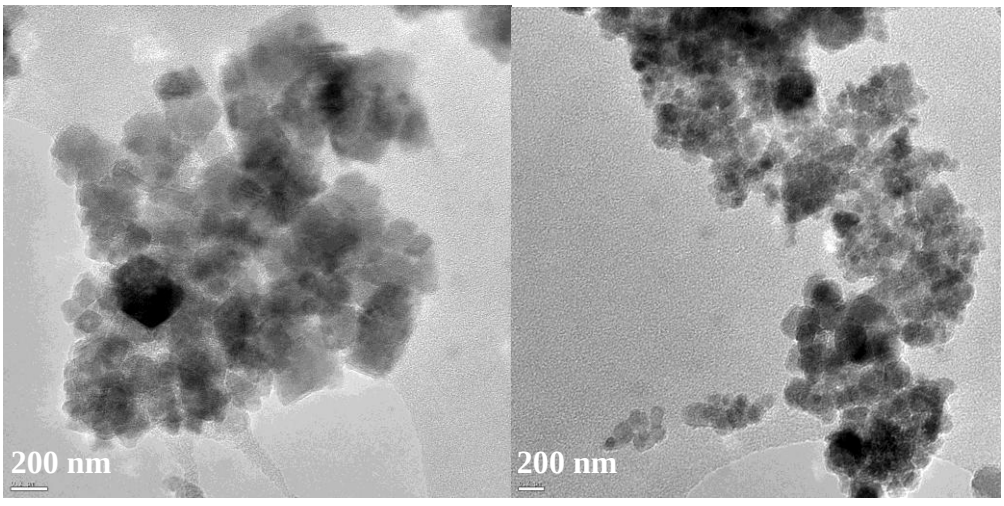

Figure 3.22 TEM micrograph of alginic acid coated -iron oxide NPs.

3.1.2.3.4 Thermal Analysis

Thermogravimetric analysis curves of iron oxide (Fe_3O_4), alginic acid coated -iron oxide NPs and alginic acid are presented in Fig. 3.23. Weight loss scale allows a quantitative comparison of weight loss of samples. Iron oxide shows no significant weight loss in the temperature range of TG analysis. Alginic acid coated Fe_3O_4 shows similar weight loss trend like alginic acid, but its thermal decomposition begins at a much lower temperature. This behavior could be originated from the fact that iron oxide particles behave as catalysts thus reducing the degradation temperature of alginic acid.

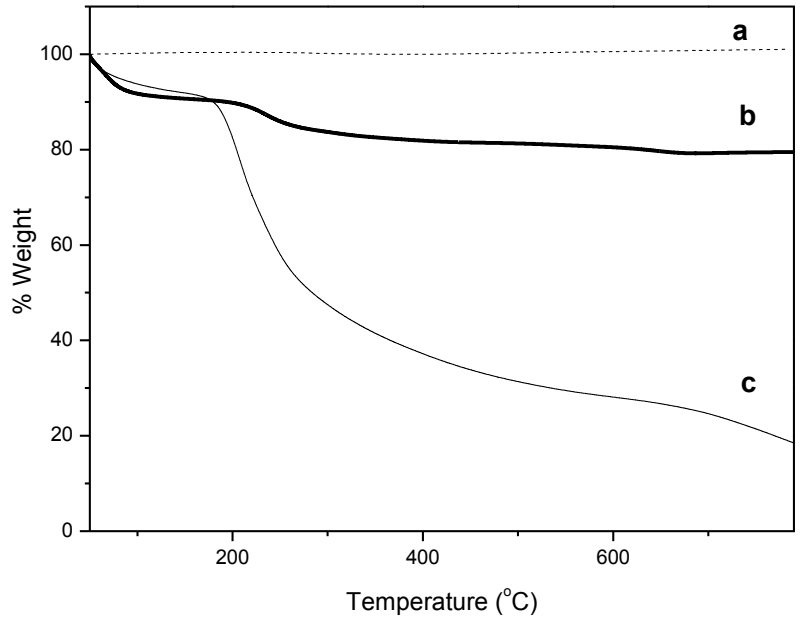

Figure 3.23 TGA diagrams of **(a)** uncoated Fe_3O_4 NPs **(b)** alginic acid coated Fe_3O_4 NPs and **(c)** alginic acid.

3.1.2.3.5 SEM Analysis

Microstructure of alginic acid coated Fe_3O_4 NPs was investigated by SEM and few micrographs are presented in Fig.3.24. Micrographs reveal a high degree of agglomeration, the particle size is much larger compared with the crystallite size obtained from XRD indicating the polycrystalline nature of the observed particle morphologies.

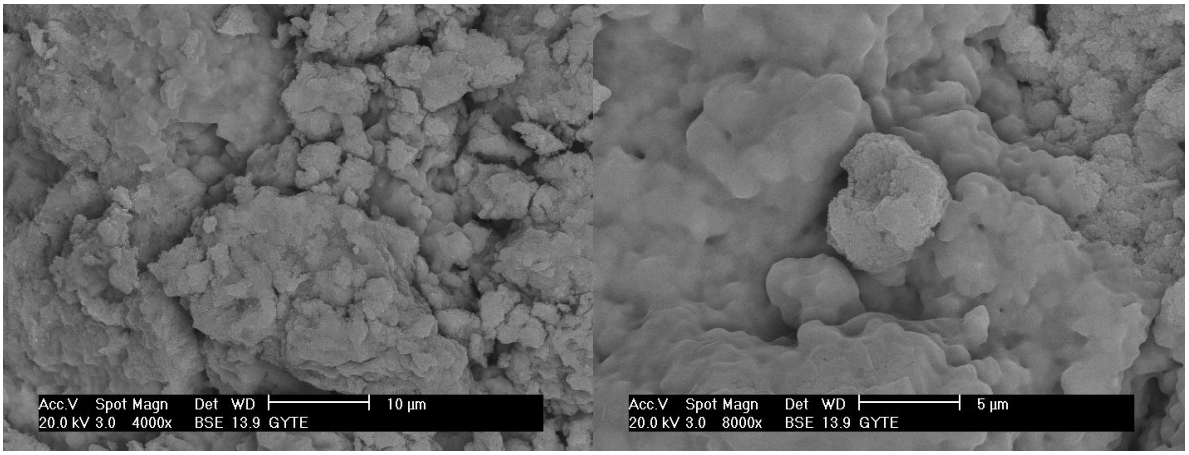

Figure 3.24 SEM micrographs of alginic acid coated Fe_3O_4 NPs.

3.1.2.3.6 Electrical properties

Conductivity characteristics of alginic acid coated Fe_3O_4 NPs. are presented in Fig. 3.25 and 3.26. AC conductivity of alginic acid coated Fe_3O_4 NPs. is found temperature independent in the temperature range of 20-100 ^oC and increasing exponentially with increasing frequency above 0.2 MHz. At lower frequencies, it has non-varying charactersitics at all operated temperatures and frequencies.

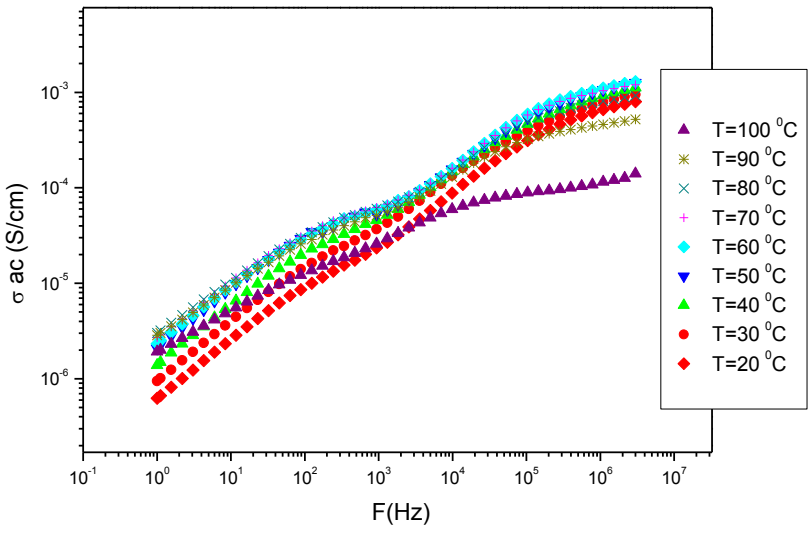

Figure 3.25 AC conductivity of alginic acid coated Fe_3O_4 NPs versus frequency.

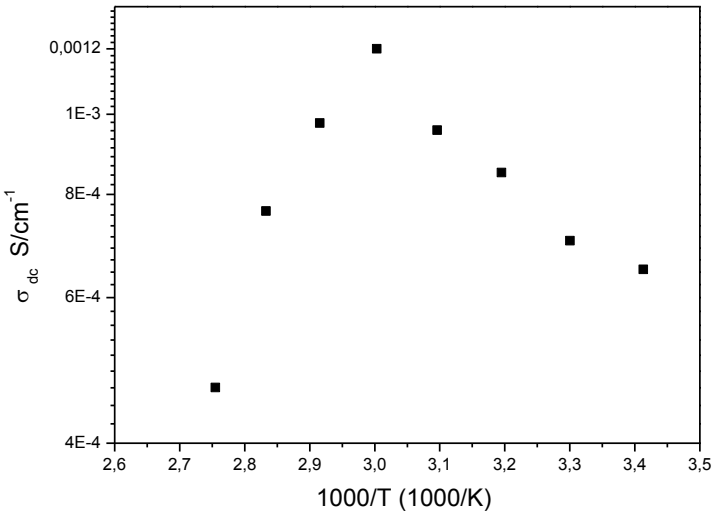

Figure 3.26 DC conductivity of alginic acid coated Fe_3O_4 NPs versus 1000/T (K).

The relation of frequency and temperature sensitive dependency of stored and dissipated energies by PVTri-Fe_3O_4 in the frequency range of 1-10^2 Hz and temperature range of 20-100 ^oC area can be inferred from mesh curves of ε' and ε'' presented in Fig. 3.27a and Fig. 3.27b, respectively. The general trend in both ε' and ε'' is decrease by increasing frequency and decreasing temperature.

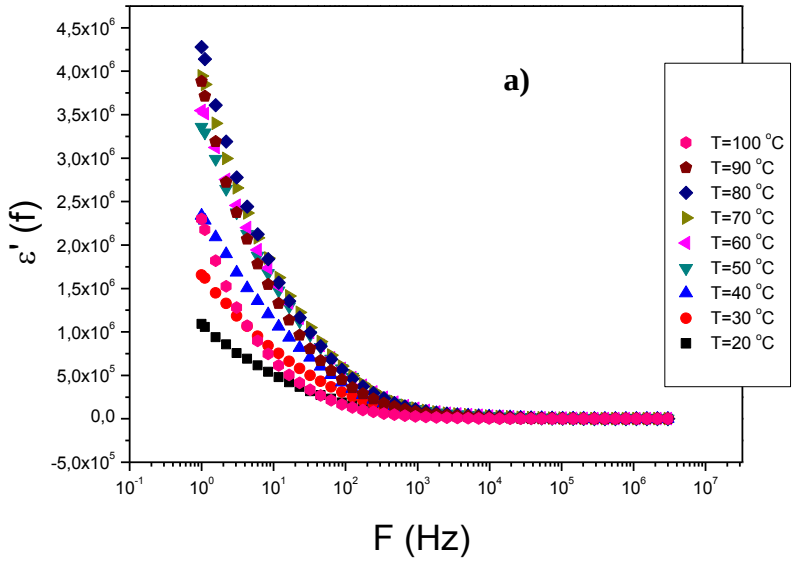

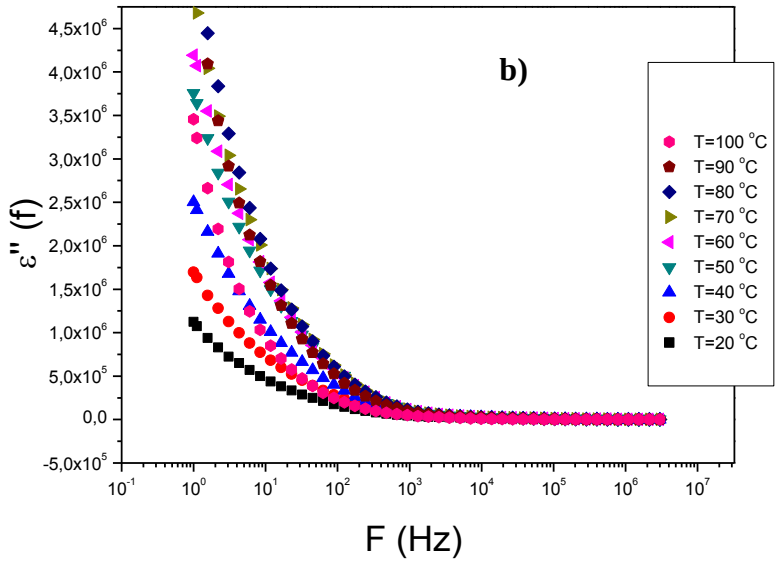

Figure 3.27 a) Real part of permittivity and **b)** Imaginary part of permittivity as a function of frequency at various temperatures of alginic acid coated Fe_3O_4 NPs.

3.1.3 Direct ultrasonic-assisted route

3.1.3.1 XRD Analysis

Phase investigation of the crystallized product was performed by XRD and the diffraction pattern is presented in Figure 3.28. The XRD pattern indicates that the product is magnetite, Fe_3O_4, and the diffraction peaks are broadened owing to very small crystallite size. All of the observed diffraction peaks are indexed by the cubic structure of Fe_3O_4 (JCPDS no. 19-629) revealing a high phase purity of iron oxide. The lattice parameter "*a*" for the synthesized iron oxide NPs was refined as 8.388 ± 0.001 Å and observed eight peaks with the following miller indices: (220), (311), (400), (422), (333), (440), (620), and (533). The average crystallite size, *D* and σ, was obtained as 8 ± 4 nm as a result of this line profile fitting.

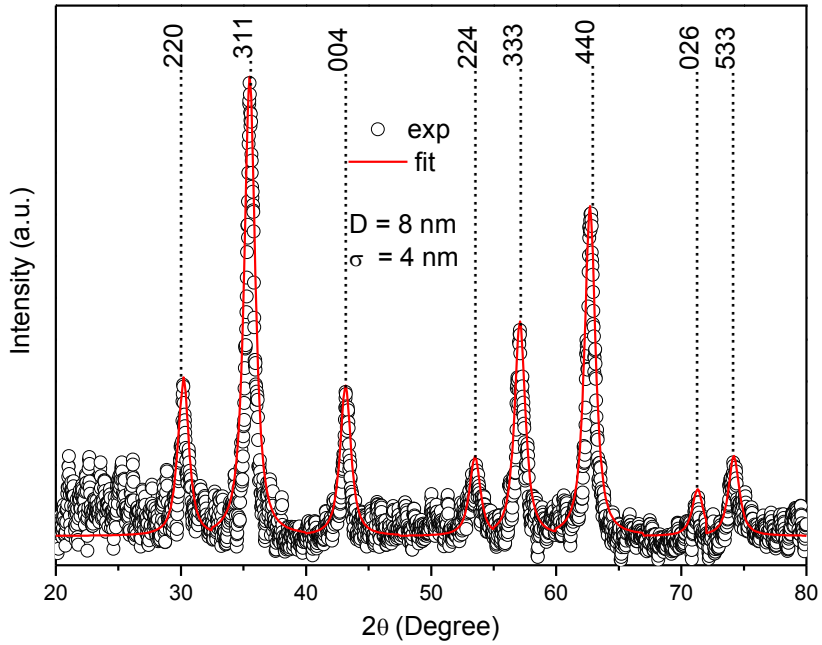

Figure 3.28 XRD powder pattern and line profile fitting of Fe_3O_4 NPs.

3.1.3.2 FTIR Analysis

Fig. shows the FTIR spectra of Fe_3O_4 NPs. At Fig. 3.29 Metal-oxygen band, υ_1, observed at 564 cm^{-1} corresponds to intrinsic stretching vibrations of the metal at tetrahedral site (Fe_{tetra}↔O), whereas metal-oxygen band, υ_2,observed at 447 cm^{-1}, is assigned to octahedral-metal stretching (Fe_{octa}↔O) [95,96]. Two broad peaks at 3424 and 1632 cm^{-1} occur due to presence of a small amount of adsorbed water. The IR bands at 1048 cm^{-1} and 1390 cm^{-1} should be attributed to the absorption of the ethanol molecules on the surface of the magnetite particles.

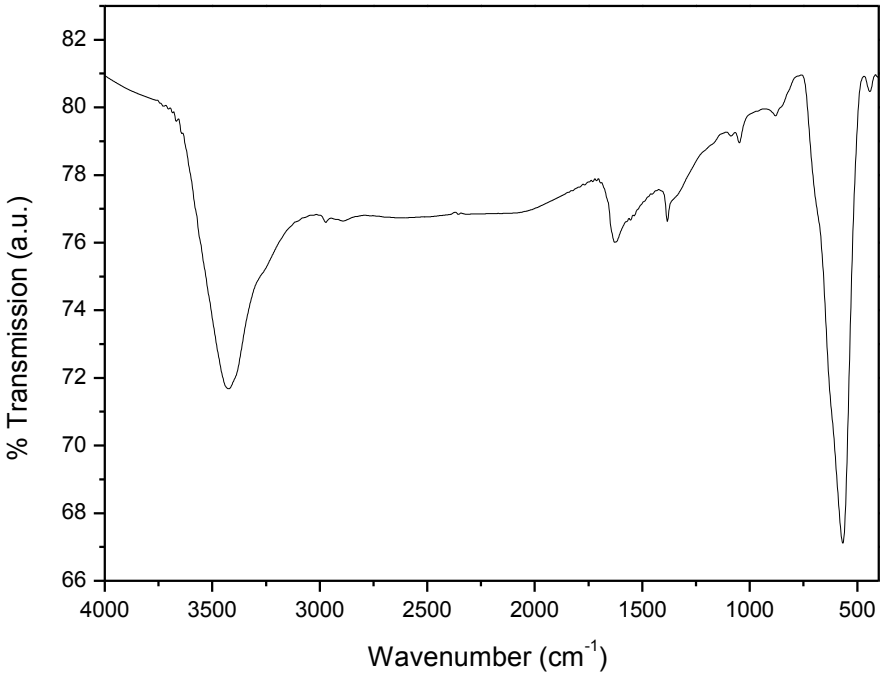

Figure 3.29. FTIR spectra of as-synthesized Fe_3O_4 NPs.

3.1.4 Preparation of Poly(1-vinyl-1,2,4-triazole) (PVTri)-Fe_3O_4 nanocomposites[2]

3.1.4.1 XRD analysis

The XRD powder diffraction pattern of PVTri coated NPs is presented in Fig. 3.30. The XRD pattern indicates that the product is magnetite (although the presence of maghemite γ-Fe_2O_3 can not be excluded), Fe_3O_4, and the diffraction peaks are broadened owing to very small crystallite size. All of the observed diffraction peaks are indexed by the cubic structure of Fe_3O_4 (JCPDS no. 19-629) revealing a high phase purity of the product. The mean size of the crystallites was estimated from the diffraction pattern by line profile fitting method. The line profile, shown in Fig. 3.30 was fitted for observed seven peaks with the following miller indices: (220), (311), (222), (400), (422), (511), and (440). The average crystallite size, D_{XRD}, was obtained as 12 ± 6 nm as a result of this line profile fitting.

[2]H. Kavas, Z. Durmus, A. Baykal, A. Aslan, A. Bozkurt, M. S. Toprak, **"Conducting and Magnetic PVTri-Fe_3O_4 Nanocomposites"**, Journal of Non-Crystalline Solids (under review).

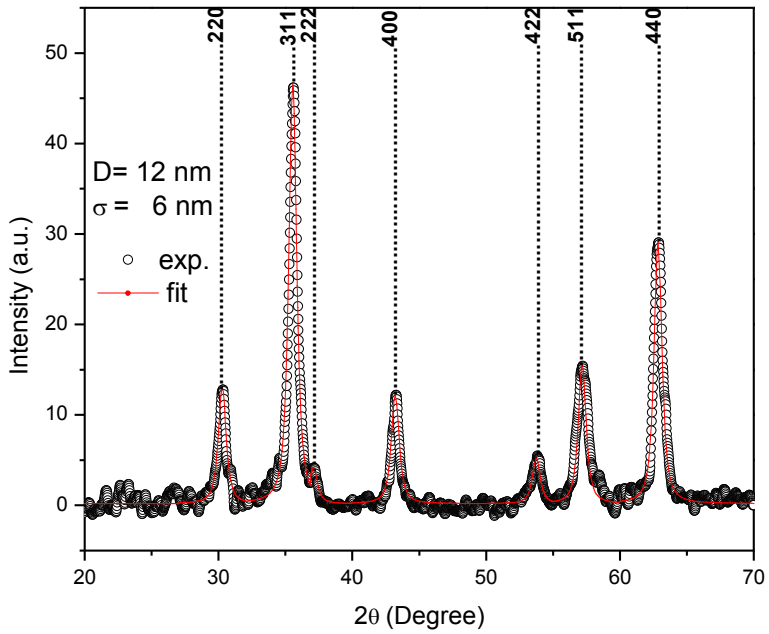

Figure 3.30 XRD powder pattern of PVTri-Fe_3O_4 nanocomposites.

3.1.4.2 Solid State ^{13}C CP-MAS NMR Spectroscopy

Poly(1-vinyl-1,2,4-triazole) (PVTri) was produced by free radical polymerization of 1-vinyl-1,2,4-triazole in toluene using AIBN (1 mol %) as initiator. The solid state ^{13}C CP-MAS NMR spectrum on the as-synthesized polymer revealed the structure of PVTri as presented in Fig. 3.31. The characteristic C peaks of the triazole ring are observed near 145 and 155 ppm and the signals corresponding to the C of the polymer backbone appear at 40 and 55 ppm [114].

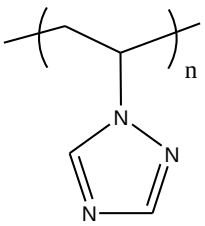

Figure 3.31 Structure of Poly(1-vinyl-1,2,4-triazole) (PVTri).

3.1.4.3 GPC studies

The GPC traces for poly(1-vinyl-1,2,4-triazole) were obtained using poly(ethyleneoxides) standards. The Mn and Mw of the polymer were measured to be 22,515 g/mol and 104,216 g/mol, respectively. The polydispersity index (M_w/M_n) of the homopolymer is 4.6.

3.1.4.4 FTIR analysis

Functional groups exhibited by uncoated Fe_3O_4, PVTri, and PVTri-Fe_3O_4 nanocomposites are investigated by FTIR spectroscopy. The FT-IR spectra of uncoated Fe_3O_4, PVTri, and PVTri-Fe_3O_4 nanocomposites are presented in Fig. 3.32. As prepared powder presents characteristic peaks that are exhibited by the commercial magnetite powder: metal-oxygen band, ν_1, observed at 590 cm^{-1} corresponds to intrinsic stretching vibrations of the metal ions at tetrahedral site ($Fe_{tetra}\leftrightarrow O$), whereas metal-oxygen band observed at 445 cm^{-1}, ν_2 is assigned to octahedral-metal ion stretching ($Fe_{octa}\leftrightarrow O$) [95,96]. The triazole rings of the pristine polymer, PVTri give rise to several medium strong peaks in the 1430-1650 cm^{-1} range due to ring stretching (C-N, C=N) vibrations. The peak at 1270 cm^{-1} is due to the ring N-N stretching. The broad peak centered at 3430 cm^{-1} was assigned to O-H vibration of molecular water interacting with the pristine PVTri. The spectral features of poly(1-vinylimidazole) are observed on PVTri-Fe_3O_4 particles by the presence of vibration bands at 1498 cm^{-1}, 1430 cm^{-1}, and 1270 cm^{-1}, respectively. These bands are absent in the spectrum of uncoated magnetite particles and confirm the presence of poly(1-vinylimidazole) on magnetite [115].

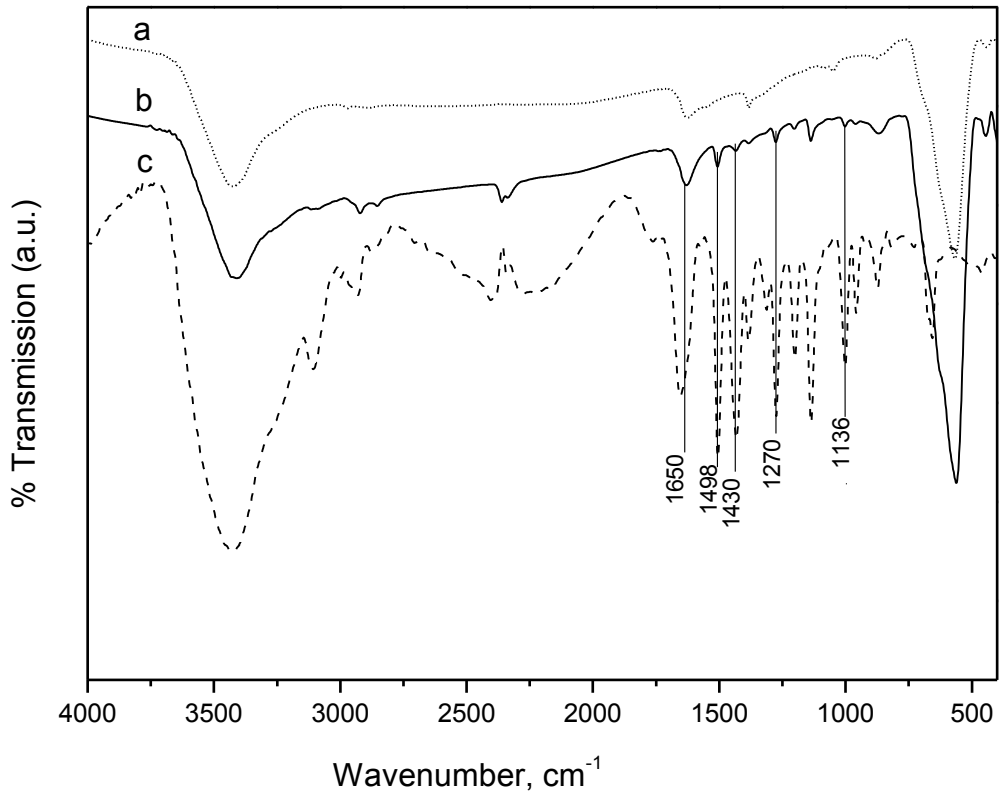

Figure 3.32 FT-IR spectra of **a)** uncoated Fe_3O_4, **b)** PVTri-Fe_3O_4 nanocomposites and **c)** PVTri.

3.1.4.5 SEM Analysis

Microstructure of PVTri-Fe_3O_4 nanocomposites was investigated by SEM and few micrographs are presented in Fig. 4. Micrographs reveal a high degree of agglomeration, however, individual NPs can also be observed by a closer examination with diameterin the range of 15-20 nm, in agreement with the crystallite size estimated from x-ray line profile fitting. This may indicate the single crystalline nature of Fe_3O_4 NPs.

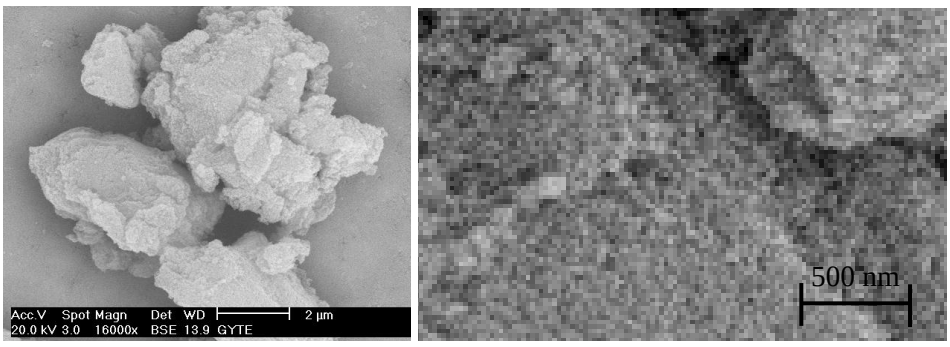

Figure 3.33 SEM micrographs of PVTri-Fe_3O_4 nanocomposites.

3.1.4.6 Thermal Analysis

Thermal characteristics of uncoated Fe_3O_4, PVTri, and PVTri-Fe_3O_4 nanocomposites were investigated by thermal gravimetric analysis and the resultant thermograms are presented in Fig. 3.34a. There is no weight loss in the thermogram of Fe_3O_4 within the measurement range of TGA analysis. PVTri has a considerable thermal stability under inert conditions. For the homopolymer, the exponential weight decay until 200 °C can be attributed to adsorbed humidity. The onset temperature at which weight loss was observed for PVTri-Fe_3O_4 nanocomposites and PVTri is determined as ~350 ^oC. Above 350 °C a remarkable weight loss derives from the thermal decomposition of the side groups and polymer backbone. The magnitude of weight loss for the PVTri-Fe_3O_4 nanocomposites indicates the catalytic effect of iron oxide nanoparticles on the degradation of the polymer PVTri.

The DSC thermograms of both PVTri and nanocomposite are presented in Fig 3.34.b. The pristine polymer exhibits a glass transition temperature of (T_g) near 160 ^oC. However, nanocomposite has two glass transition domains. The onset of the first transition which corresponds to 80 ^oC may due to plastization effect of complexed water with trizole units (see FT-IR part). For the same sample the second transition is near 180 ^oC which belongs to T_g of PVTri-Fe_3O_4 domains.

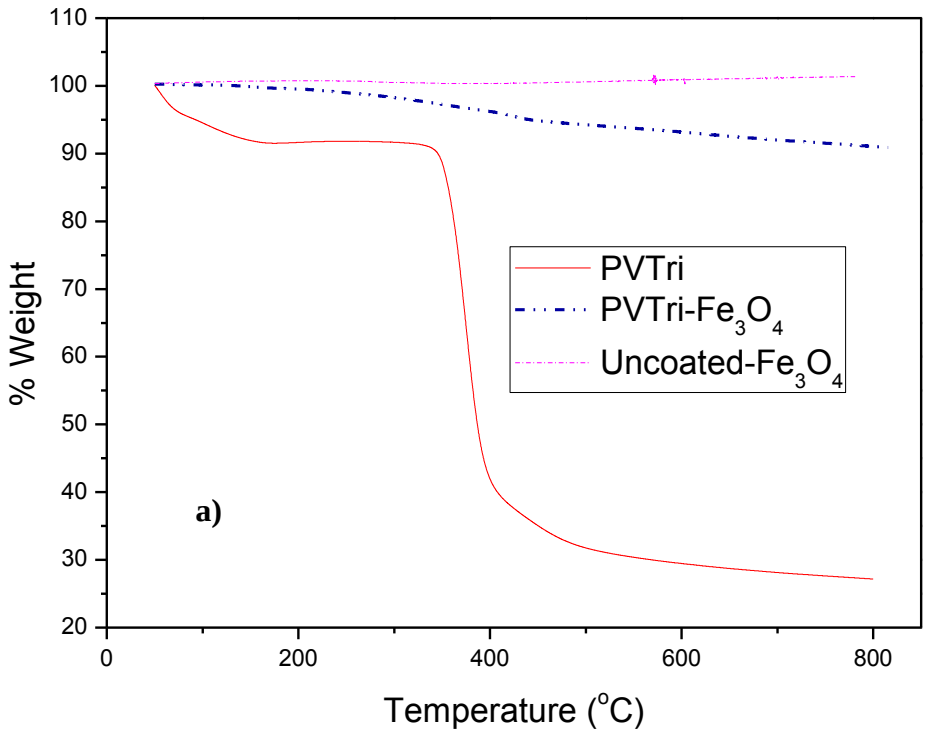

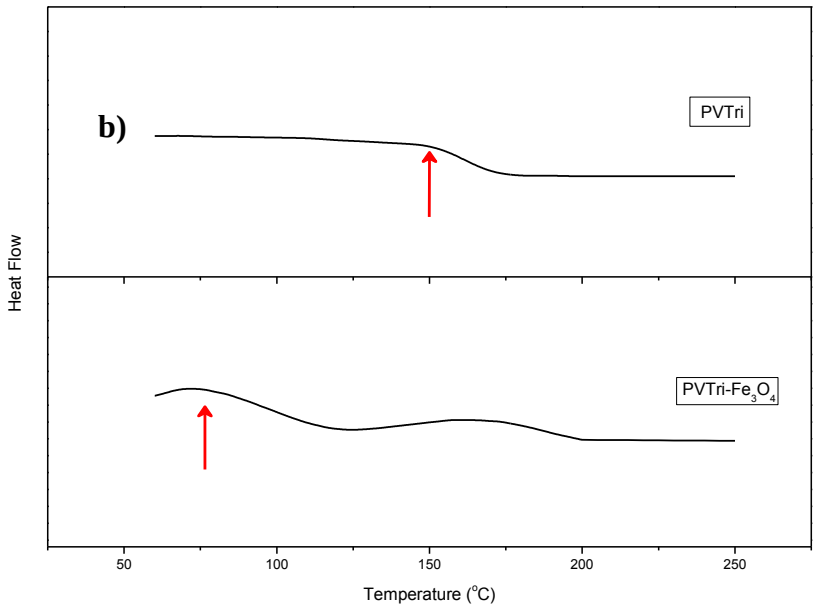

Figure 3.34 **a)** TGA thermograms of the uncoated Fe_3O_4, PVTri, and Fe_3O_4/PVTri nanocomposite, and **b)** DSC curves of PVTri, and Fe_3O_4/PVTri nanocomposite.

3.1.4.7 Electrical properties

3.1.4.7.1 Electrical Conductivity

Alternating current (AC) conductivity, $\sigma_{AC,}$ of the PVTri/Fe_3O_4 was studied as a function of frequency and temperature and results are shown in Fig. 3.35. The σ_{AC} does not change with frequency between 1-10 kHz at all temperatures but it changes at higher frequencies. By decreasing temperature, the σ_{AC} decreases sharply with nearly equivalent slope at elevated temperatures, but its decrease becomes smooth with separated curves below 70 ^{o}C. The observed AC conductivity curves in the order of 10^{-4} -10^{-6} S·cm^{-1} is consistent with that of lysine coated iron oxide nanocomposites reported in our earlier study [116]. The AC conductivity as a funtion of frequency for PVTri at various temperatures is presented in Fig. 6c. The observed trends are same at all temperatures except at 150 ^{o}C, the AC conductivity values enourmously higher at this temperature than at lower temperatures. This temperature corresponds to the onset of glass transition temperature of the pristine PVTri host polymer and conductivity increase at this temperature may be because of contribution of ionic conductvity.

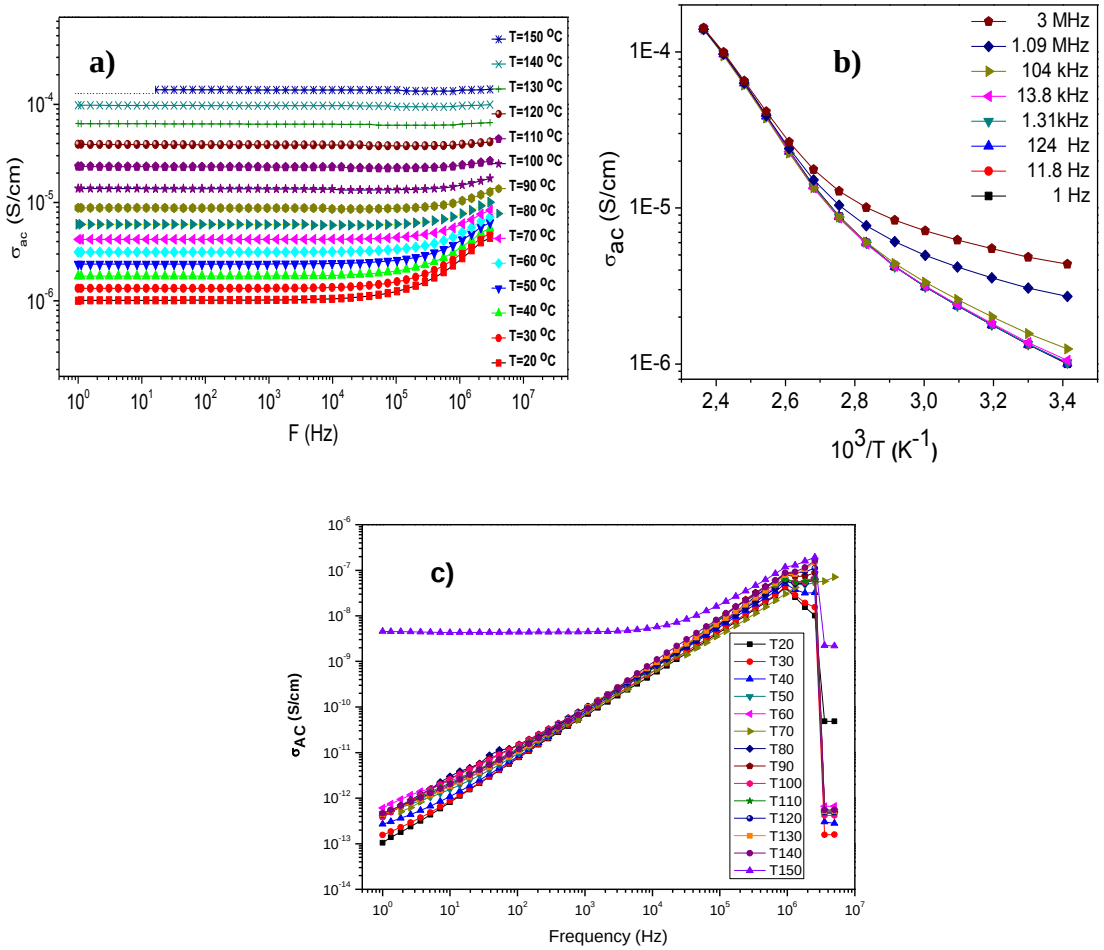

Figure 3.35 AC conductivity vs. (a) frequency, and (b) temperature (1000/T) for Fe_3O_4/PVTri nanocomposites.

The direct current (DC) resistivity was derived from the plateau regions presented in Fig.3.36. The ionic or vacant sites charge carriers give low mobility systems such as ferrites and the hopping process causes the major conduction [117,118]. Electron hopping takes place between the neighboring iron cations with two and three valence [119,120]. In this process, drift mobility of charge carriers increases by increasing temperature, and causes a decrease in DC resistivity. The influence of various parameters such as porosity, chemical composition, particle size [121,122] and cation distribution [123] on the conductivity of ferrites have been explained in earlier reports. It is found that PVTri-Fe_3O_4 NPs have higher resistivity compared to iron oxide NPs in Ref [116] and closer to resistivity of L-lysine-coated one. Fig. 3.36 reveals that the electrical resistivity of the PVTri-Fe_3O_4 system decreases with two different activation energies as the temperature increased0.630 eV and 0.247 eV for above

and below 80 ^{o}C, respectively. The reason of the change in the activation energy at 80 ^{o}C, (0.0028 K^{-1}) can be attributed to onset of glass transition temperature (onset of first transition domain) of the host polymer, PVTri. The minimum conductivity 1.02 μS/cm is obtained at 20 ^{o}C.

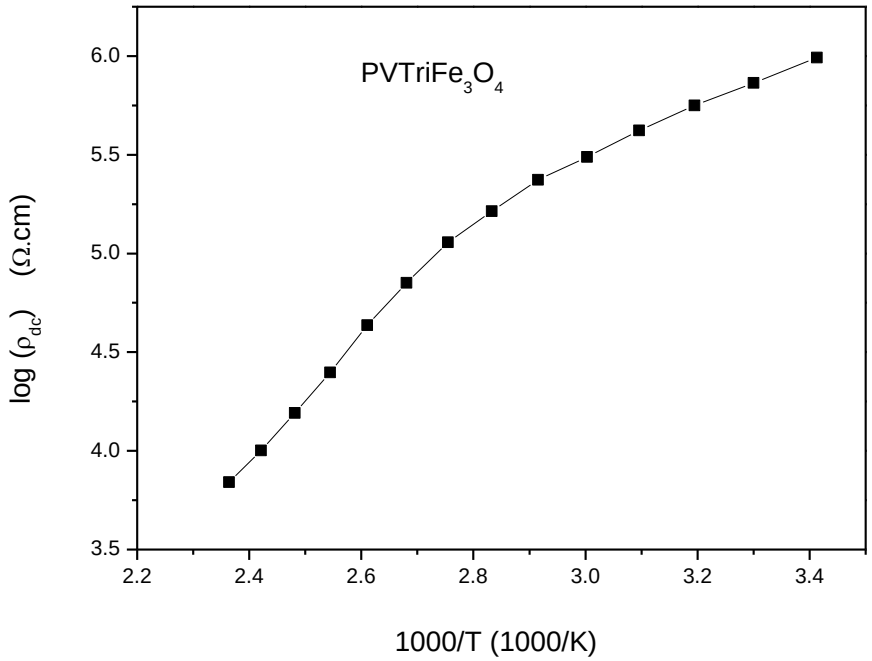

Figure 3.36 The DC resistivity versus reciprocal temperature for the PVTri-Fe_3O_4 nanocomposite.

3.1.4.7.2 Dielectric Permittivity

The relation of frequency and temperature sensitive dependency of stored and dissipated energies by PVTri-Fe_3O_4 in the frequency range of 1-10^2 Hz and temperature range of 50-150 ^{o}C area can be inferred from mesh curves of ε' and ε'' presented in Fig. 3.37 and Fig. 3.38, respectively. The general trend in both ε' and ε'' is decrease by increasing frequency and decreasing temperature.

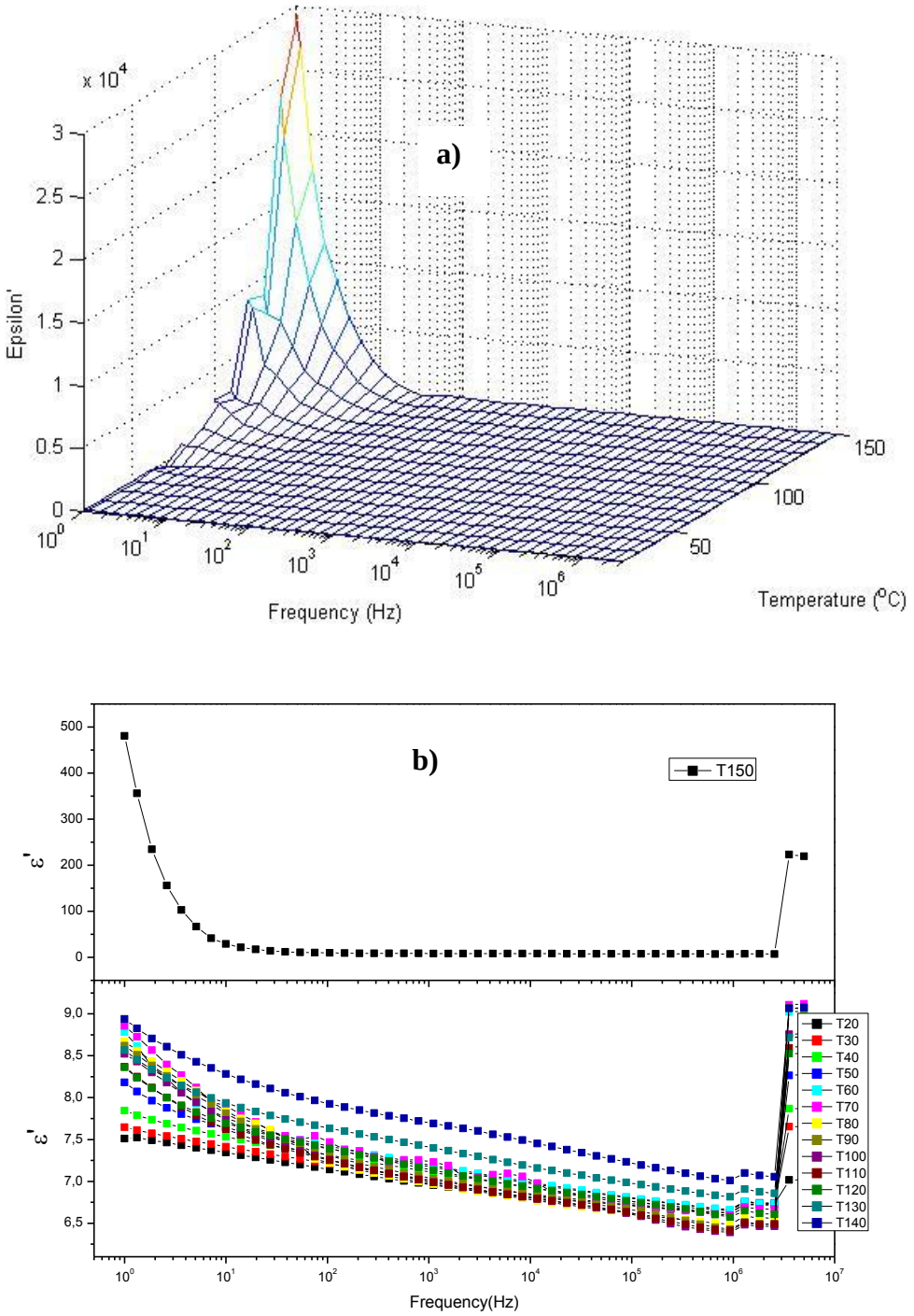

Figure 3.37 Real part of permitivity as a function of frequency at various temperatures of **a)** PVTri-Fe_3O_4 nanocomposite, and **b)** PVTri.

The frequency dependent dielectric dispersion curve can be explained on the basis of Koop's theory, which is based on the Maxwell–Wagner model for the homogeneous double structure [117] in which the highly conducting grains are separated by relatively poor conducting grain boundaries and are found to be more effective at higher frequencies, while

grains are more effective at lower frequencies [124]. The conductivity difference between grains and grain boundaries means different resistance causing the accumulation of charge carriers in separated boundaries and increase in dielectric constants.

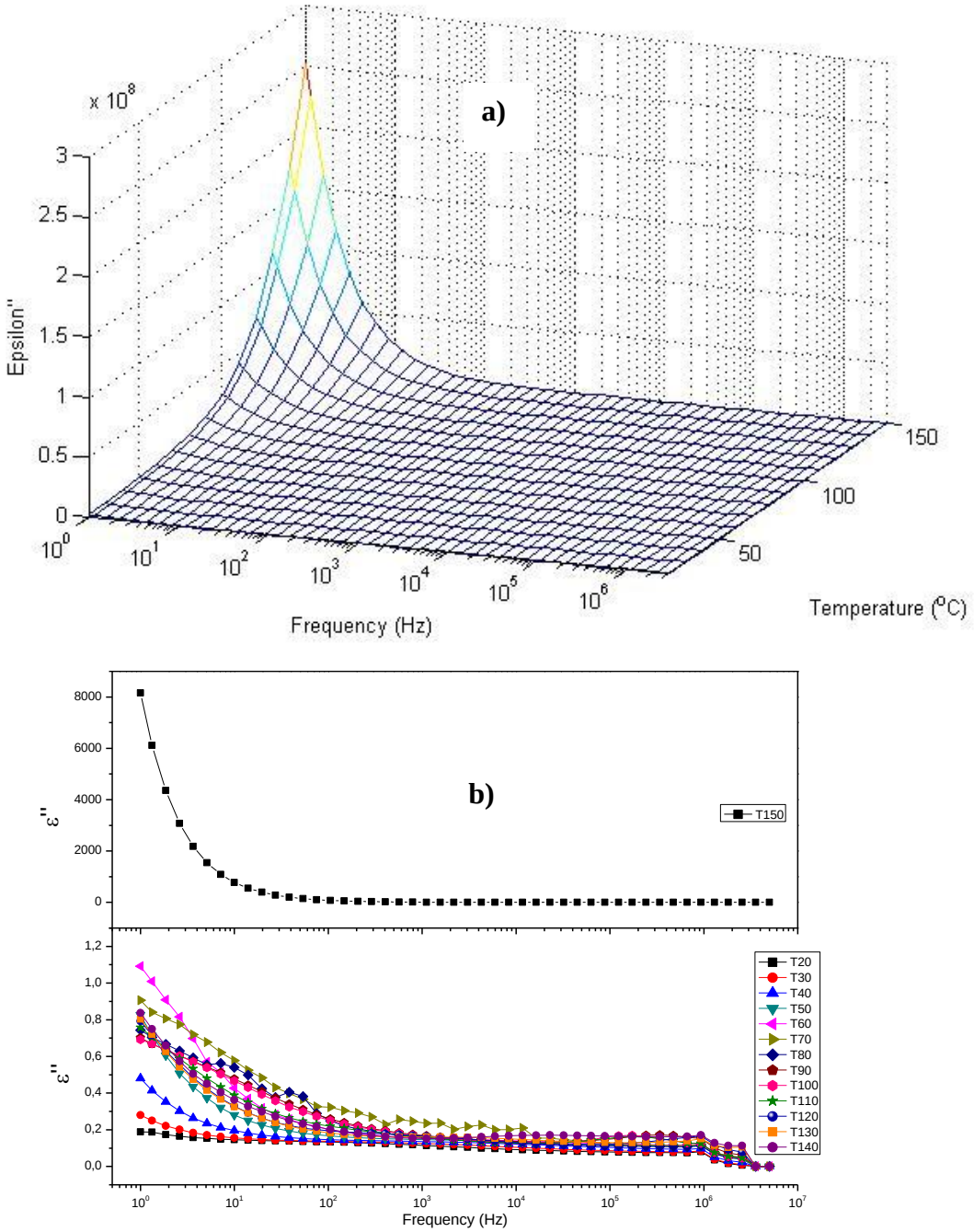

Figure 3.38 Imaginary part of permitivity as a function of frequency at various temperatures of **a)** PVTri-Fe_3O_4 nanocomposite, and **b)** PVTri.

The polarization in ferrites is through a mechanism similar to the conduction process by electron exchange between Fe^{2+} and Fe^{3+}, the local displacement of electrons in the direction of the applied field occurs and these electrons determine the polarization. With increasing frequency, the polarization decreases and reaches to a constant value due to the electron exchange between Fe^{2+} and Fe^{3+} cannot follow the alternating field. Previously, the large value of dielectric constant at lower frequency was attributed to the predominance of species like Fe^{2+} ions, oxygen vacancies, grain boundary defects, etc. [118] The decrease in dielectric constant with frequency is natural because of the fact that any species contributing to polarizability is found to show lagging behind the applied field at higher and higher frequencies [119].

The dielectric constants increase with increasing temperature as seen in semiconductors. Thermal energy convert the bound charges to the charge carriers, and increasing charge carrier concentration always gives easy alignment of dipoles in the applied AC electrical field and so increase in dielectric constants. Also above the onset of first glass transition of PVTri ~80 ^{o}C (2.8 K^{-1} in 1000/T scale), mobility of the charge carriers increases. The combined effect of increasing charge carrier concentration in iron oxide by increasing temperature and phase transition of PVTri at high temperatures can be seen in dielectric mesh curves. The gigantic values of real and imaginary permittivity at higher temperatures can be caused from the second glass transition temperature originated from host polymer's triazole units.

3.2 Mn_3O_4 analysis

3.2.1 Ionic liquid assisted route (Green Chemistry)[3]

In this study, synthesis of Mn_3O_4 nanocrystals were performed at room temperature by using environment friendly [BMIM]OH which was recovered at the end of the synthesis process. As-made NPs were then characterized using XRD for the identification of the crystallographic phases present.

3.2.1.1 XRD Analysis

A typical XRD pattern of the as-synthesized Mn_3O_4 powder is shown in Fig. 3.39. All diffraction peaks were indexed to the tetragonal Mn_3O_4 (which are consistent bulk value

[3]Z. Durmuş; H. Kavas; A. Baykal; M.S. Toprak **"A Green Chemical Route for the Synthesis of Mn_3O_4 Nanocrystals",** Central European Journal of Chemistry 7(3) • 2009 • 555-559.

ICDD Card no. 24-0734). No extra peaks indicating impurities and other forms of manganese oxides were detected. The line profile, shown in Fig.3.39, is fitted for 14 peaks with the following Miller indices: (112), (220), (013), (211), (004), (220), (204), (015), (312), (224), (116), (400), (411) and (304). As a result a *D* of 41.5 ± 11 nm was obtained for as-synthesized Mn_3O_4 nanocrystals.

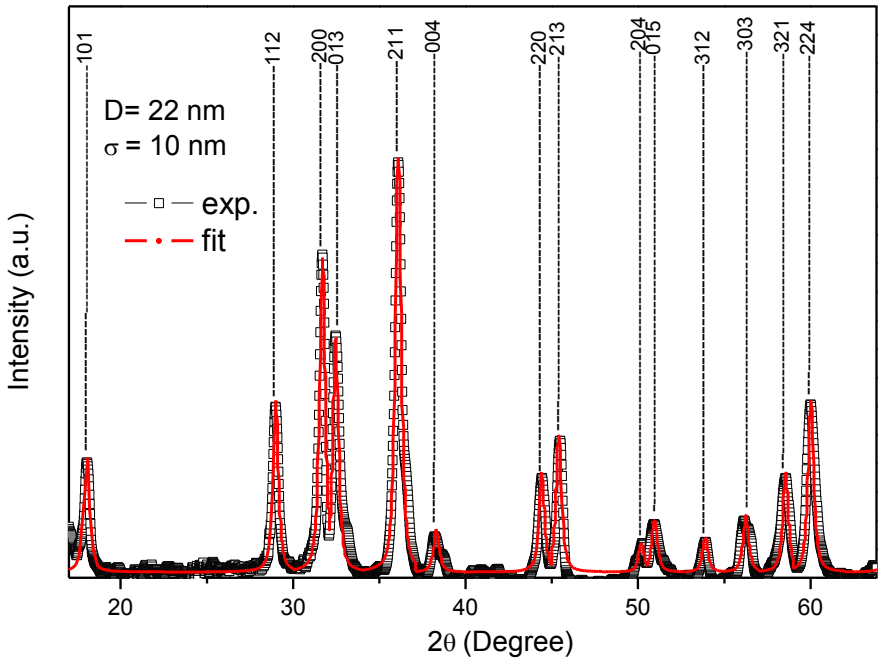

Figure 3.39 X-ray powder diffraction pattern and line profile fitting of as-synthesized Mn_3O_4 NPs.

Zou et al. [125] reported on the possible formation mechanism of Co_3O_4 NPs in the presence of ionic liquid at room temperature. Ionic liquid was suggested to act as both the reaction medium and electrical conductor which resulted in accelerating electron transfer for the following suggested reactions for the formation of Mn_3O_4:

$$Mn^{2+}{}_{(aq)} + 2\,OH^-{}_{(aq)} \longrightarrow Mn(OH)_{2\,(s)} \qquad (1)$$

$$3Mn(OH)_{2\,(s)} + H_2O_{2\,(aq)} \xrightarrow[25\ ^oC]{[BMIM]OH} Mn_3O_{4\,(s)} + 4H_2O \qquad (2)$$

It is also reported that in the absence of ionic liquid, reaction (2) did not take place at room temperature. Thus, here the key point is the presence of the ionic liquid for electron transfer. For the synthesis of Mn_3O_4 nanocrystals in the presence H_2O_2, the usage of ionic liquid is therefore crucial.

3.2.1.2 FTIR Analysis

FTIR analysis performed for the prepared sample and results are presented in Fig. 3.40. Two broad peaks at 3414 and 1620 cm^{-1} are assigned to O-H stretching and bending modes of adsorbed water. Two absorption bands observed at 625 and 515 cm^{-1}, are associated with the coupling between Mn-O stretching modes of tetrahedral A- and octahedral B- sites [126,127] as expected from normal spinel structure. Thus, the FTIR spectrum further confirms that the product is Mn_3O_4.

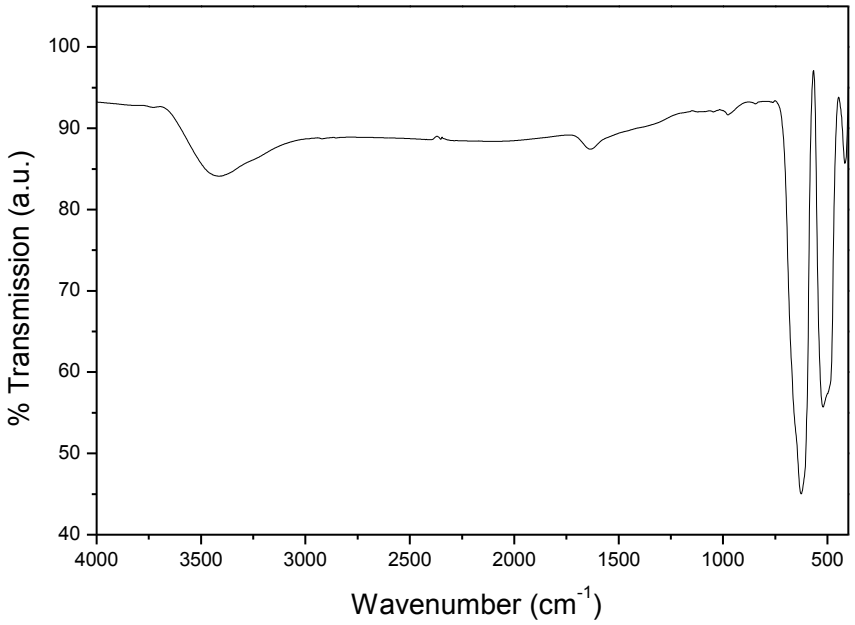

Figure 3.40 FTIR spectrum of as-synthesized Mn_3O_4 NPs.

3.2.1.3 TEM Analysis

Morphology of Mn_3O_4 NPs were investigated by TEM and few micrographs are presented in Fig. 3.41. A wide dispersion of particle size was detected. A variety of morphologies mainly including spheroid, tetragonal and rod shaped have been observed. Particle size calculations, estimated from the TEM micrographs after counting a minimum of 300 NPs, resulted in the following values: 45% of spherical NPs with diameters between 58 and 388 nm; 47% cubic particles with size between 85 and 360 nm; and 8% nanorods with aspect ratios in the range of 98x360 nm to 104x683 nm. A comparison of crystallite size obtained from XRD analysis with the TEM observations reveals the polycrystalline nature of as-synthesized Mn_3O_4 NPs.

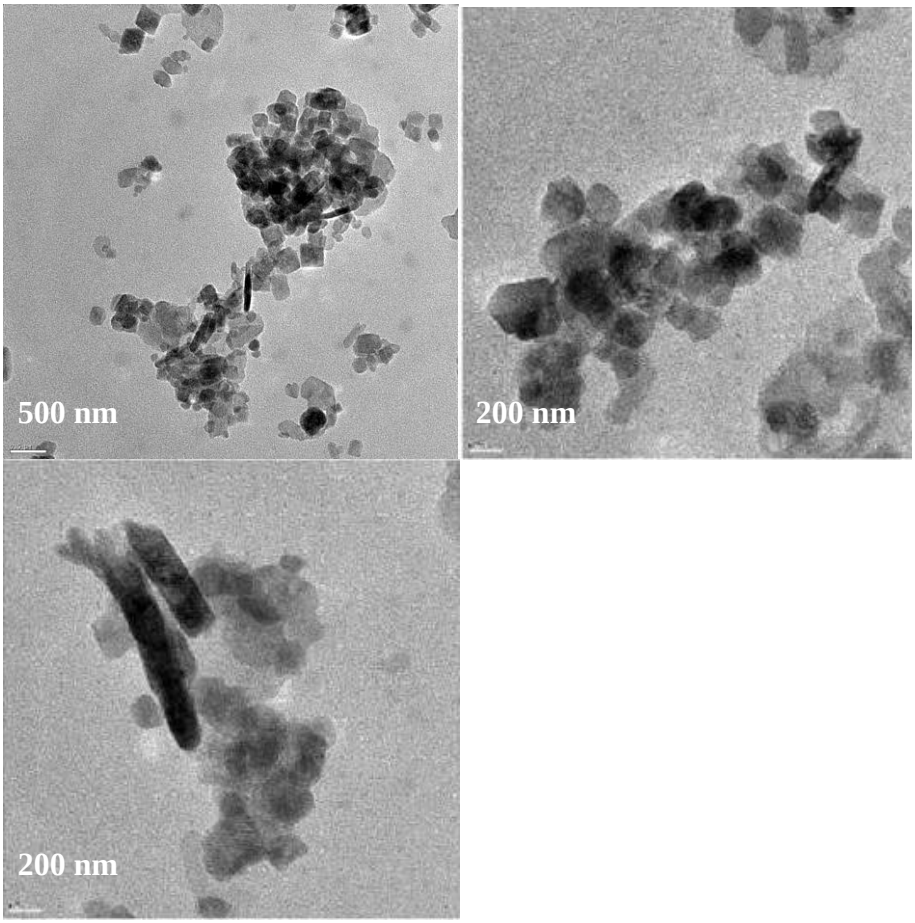

Figure 3.41 TEM micrographs of as-synthesized Mn_3O_4 NPs with various morphologies.

3.2.1.4 EPR Analysis

The magnetic properties of the as-synthesized Mn_3O_4 were measured using a EPR technique in X band and the spectrum is presented in Fig. 3.42. EPR analysis gave some facts about the interactions in nano manganese oxide. The broad EPR lines are observed without hyperfine splitting for Mn^{+2} and Mn^{+4} with linewidth of 2787 Gauss and resonanace field of 4026 Gauss. This symmetric broad line shows the existence of strongly interacting Mn^{+2} ions in Mn_3O_4 and is the result of convolution of different resonance fields due to the distribution of local effective fields during dipolar interactions between particles as suggested by Winkler et al. [128]. Moreover, in our study, the anisotropy resulting from a broad size distribution in the range of 8-680 nm and various morphologies can cause wide range inter-particle and intra-particle interactions. Smaller particles in nano range may have magnetically disordered surface comparable with the total volume. These type of structures can be classified as core-shell structures and they include cluster of free spins located at this disordered surface. In our earlier work we reported on their effects by vibrating sample magnetometry (VSM) for

Mn_3O_4 obtained via different methods [129]. All of the above listed factors may cause broad EPR lines. The g values are obtained as 1.55 which are smaller the literature value of g for Mn_3O_4 (2.01). This might be due to the exchange-coupled system with unlike spins such as canted spin at surface of particles caming from the nature of the core-shell structure.

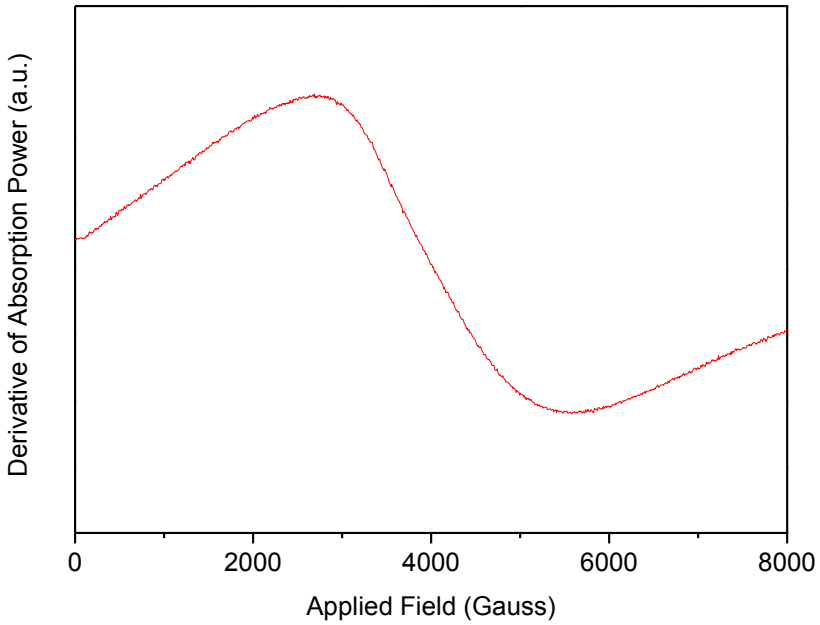

Figure 3.42 EPR absorption spectrum of as-synthesized Mn_3O_4 NPs.

3.2.2 Hydrothermal route

3.2.2.1 Hydrothermal route with TMAOH/NaOH[4]

Mn_3O_4 was prepared by a simple two-step hydrothermal method. The first step was preparation of $Mn(OH)_2$ gel by conventional process and the second step was gel oxidation by hydrothermal treatment. Hydrolysis of manganese acetate provides manganese hydroxide and acetic acid. This acetic acid helps in the partial oxidation of Mn(II) of manganese hydroxide to final phase of Mn_3O_4, detailed reactions are given in Figure 3.43 with respect to the order of occurrence as described above [130]:

[4] Z. Durmus, M. Tomas, A. Baykal, H.Kavas, T. G. Altınçekiç, M. S. Toprak, **"The effect of neutralizing agent on the synthesis and characterization of Mn_3O_4 Nanoparticles"**, Russian Journal of Inorganic Chemistry (under review).

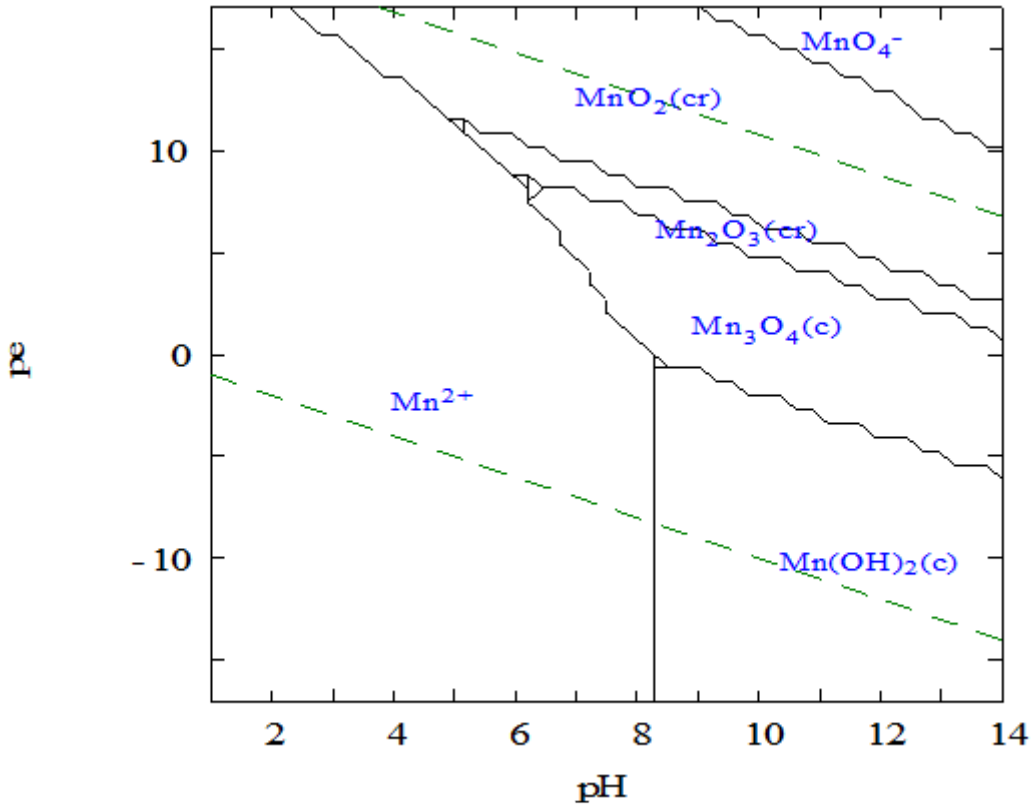

a)

$$3Mn(CH_3COO)_2 + 6H_2O \xrightarrow{NaOH\ /\ TMAOH} 3Mn(OH)_2 + 6CH_3COO^- \xrightarrow{\Delta} Mn_3O_4$$

b)

Figure 3.43 (a) Predominance diagram for Mn^{2+} and **(b)** suggested mechanism for the formation of Mn_3O_4 via two-step hydrothermal method.

3.2.2.1.1 XRD analysis

XRD pattern of the as-synthesized Mn_3O_4 powder is shown in Fig. 3.44. All diffraction peaks were indexed to the tetragonal hausmannite crystal structure model of Mn_3O_4 (which are consistent bulk value—ICDD Card no. 24-0734). No extra peaks of impurities indicating other forms of manganese oxides were detected. The mean size of the NPs was estimated from the diffraction pattern using the line profile fitting. The line profile, shown in Fig.3.44, is fitted for 14 peaks (101), (112), (200), (103), (211), (004), (220), (105), (312), (303), (321), (224), (400), (206). The average crystallite size, D and σ, were estimated as 26 ± 8 nm and 23 ± 8 nm for TMAOH and NaOH hydrolyzed samples respectively.

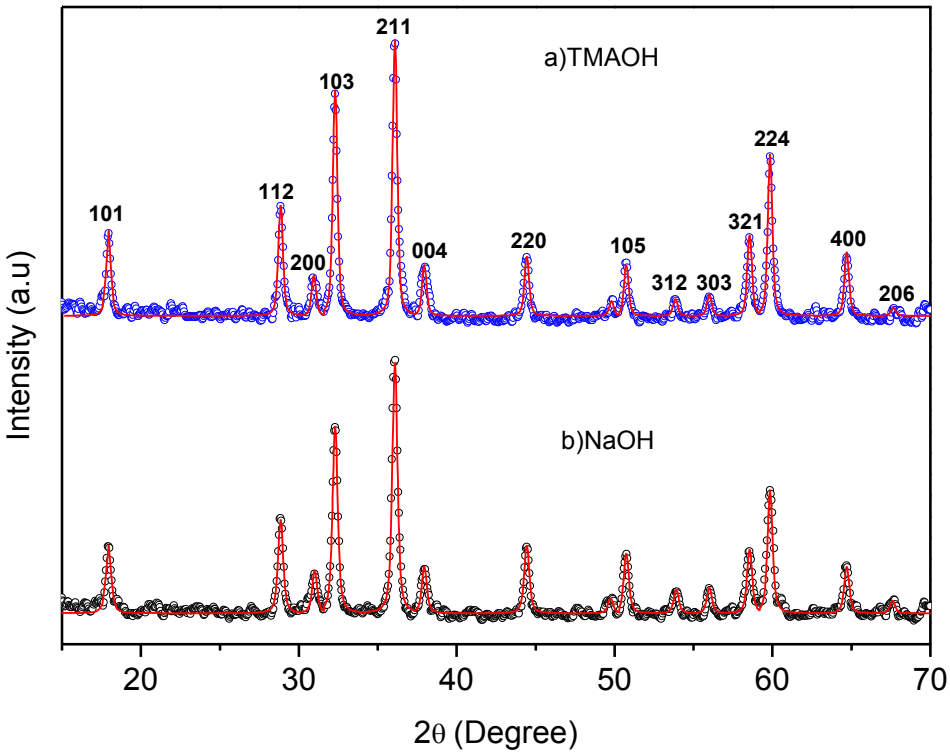

Figure 3.44 XRD pattern of as-synthesized Mn_3O_4 NPs hydrolyzed using **(a)** TMAOH, and **(b)** NaOH indexed to hausmannite Mn_3O_4.

3.2.2.1.2 FTIR analysis

FTIR analysis was performed to investigate the surface characteristics of the prepared samples and the resultant spectra are presented in Fig. 3.45. The absorption bands observed at 620 and 512 cm^{-1} are associated with the coupling between Mn-O stretching modes of tetrahedral and octahedral sites [131] together with a weak band at 1046 cm^{-1}, which can be attributed to υ_{Mn-O-H} vibration. The vibration band located at a weaker wave number, ~418 cm^{-1}, can be attributed to the vibration of manganese species (Mn^{3+}) in octahedral sites [132]. Thus, the FTIR spectrum further confirms that the product is Mn_3O_4, in consistency with reported references for Mn_3O_4. [133,134]. Two broad peaks in Fig. 3.45b at 3440 and 1638 cm^{-1} are due to the presence of a small amount of adsorbed water. Sample hydrolyzed with NaOH shows a stronger peak due to adsorbed water indicating a more hydrophilic nature of these NPs. The peak in Fig. 3.45a at 1550 cm^{-1} is due to the presence of N-H groups on the surface of the particles due to the adsorption of TMAOH used for hydrolysis.

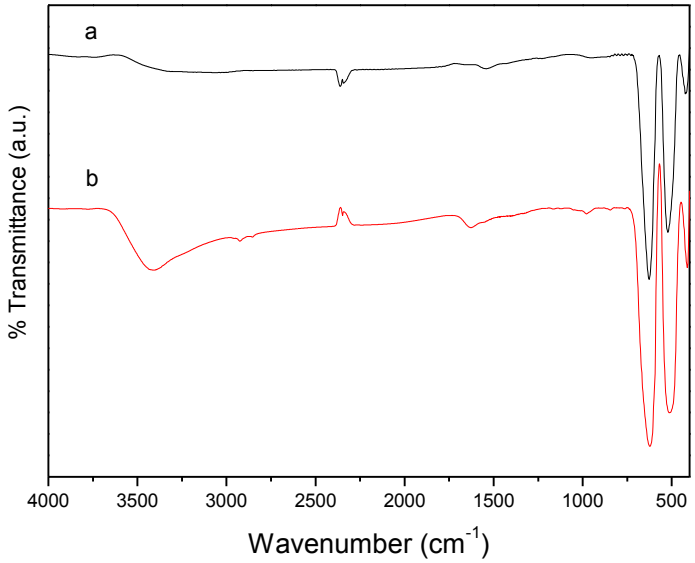

Figure 3.45 FTIR spectra of as-synthesized Mn_3O_4 NPs hydrolyzed using (**a)** TMAOH, and (**b)** NaOH

3.2.2.1.3 TEM analysis

TEM analysis was performed to investigate the morphology and size of Mn_3O_4 NPs; micrographs are presented in Fig. 3.46. NaOH-hydrolyzed samples showed spherical particles. TMAOH hydrolyzed samples exhibited particles with spherical morphology as well as particles with different polygon geometries including hexagonal. Particle size distributions were obtained from several micrographs, counting a minimum of 300 NPs. Average particle size, D_{TEM}, for samples was calculated using a log-normal fitting to the histograms obtained from several TEM micrographs as 6.8 ± 0.3 nm and 14 ± 0.43 nm for the samples hydrolyzed with NaOH and TMAOH respectively.

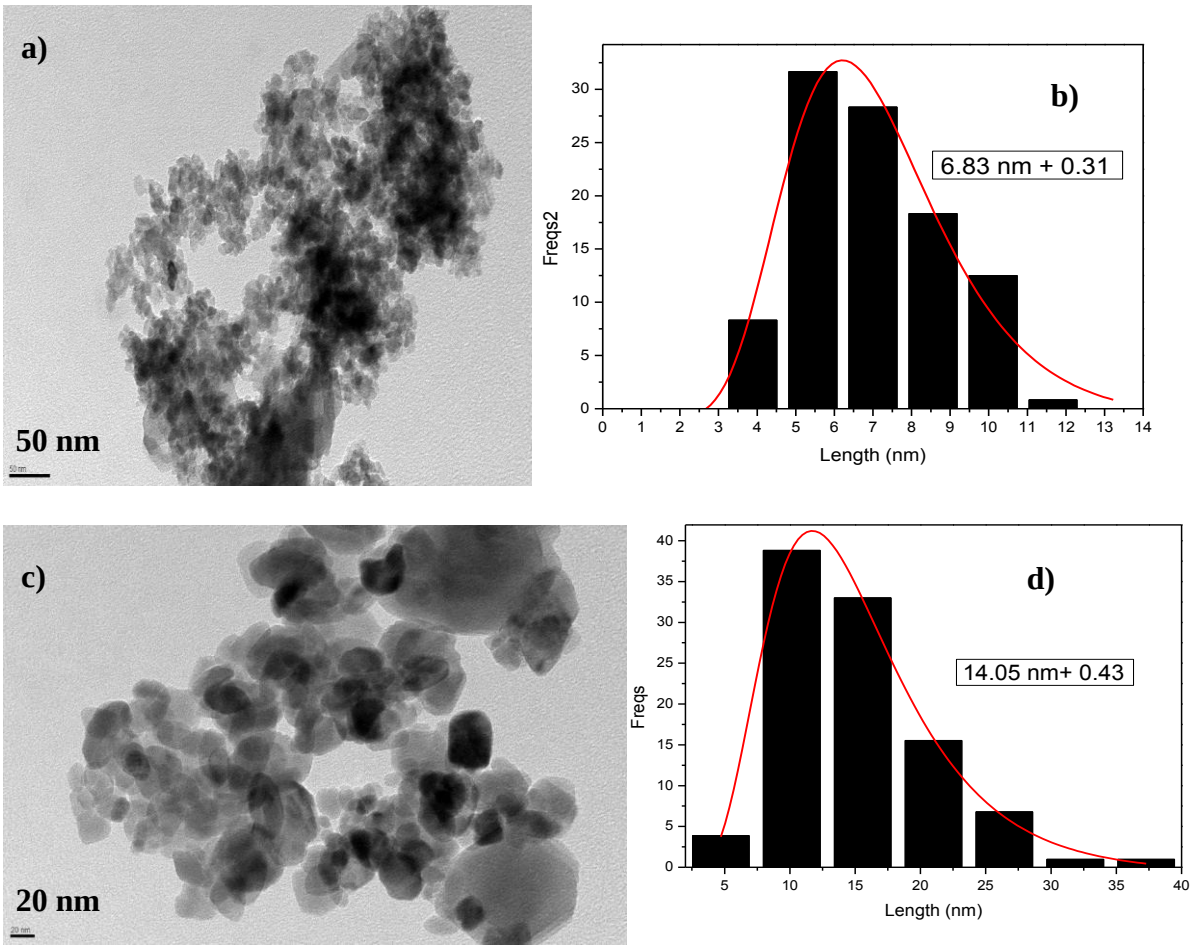

Figure 3.46 TEM micrograph and size distribution diagram of synthesized Mn_3O_4 NPs hydrolyzed using **(a,b)** NaOH and **(c,d)** TMAOH via a two-step hydrothermal method.

3.2.2.1.4 Particle Size and Zeta Potential Analysis

Particle size analyses of the two samples were performed and results are presented in Figure 3.47. Both samples show bimodal distribution with average sizes centered at ~250 nm and ~1.1 μm, which are substantially higher than the particle size determined from TEM. These observations indicate a strong aggregation of as-synthesized Mn_3O_4 NPs as there is no passivation layer on the NPs. Zeta potential analysis was performed in order to assess the dominant charges on the surface of these NPs and the results are presented in Figure 3.48. Mn_3O_4 NPs hydrolyzed by NaOH shows a point of zero charge, pzc, of 4.5 which is in agreement with the literature value reported for it [135]. However, when TMAOH is used on the surface of these NPs pzc is expected to shift to higher pH values. Our results showed that

there is a shift of pzc from 4.5 to 5-5.5 for the TMAOH hydrolyzed sample in agreement with the earlier observation [136].

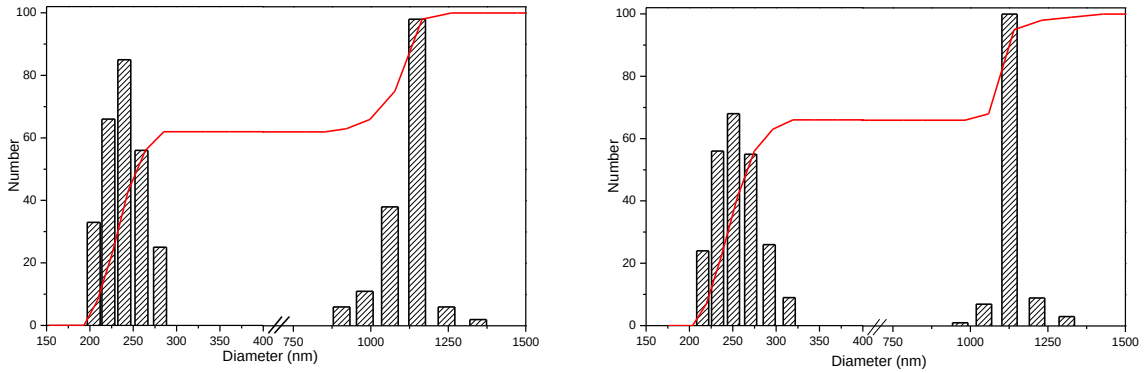

a) **b)**

Figure 3.47 Particle size analysis of as-synthesized Mn_3O_4 NPs hydrolysed using **(a)** TMAOH, and **(b)** NaOH.

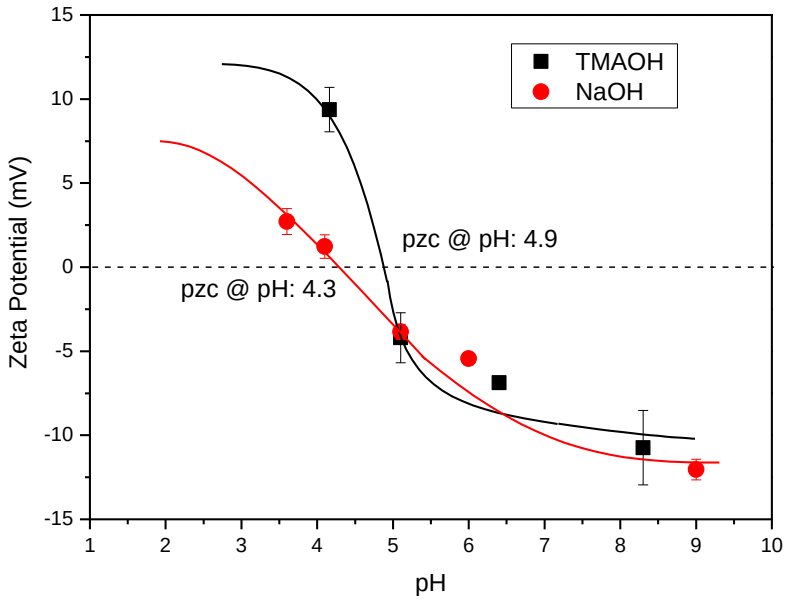

Figure 3.48 Zeta potential analysis of Mn_3O_4 NPs hydrolysed with (■) TMAOH, and (●) NaOH.

3.2.2.1.5 Thermal Analysis

Thermal gravimetric analyses (TGA) were carried out to evaluate possible compositional differences of the two samples and thermograms are presented in Figure 3.49.

Results show that the two samples, obtained from the two-step hydrothermal route, hydrolyzed using NaOH and TMAOH, show very similar thermal decomposition characteristics. There is a total loss of around ~6% for both samples. This weight loss could be due to the conversion of residual hydroxide species, not detected by the XRD, to the corresponding oxides. For the case of TMAOH hydrolyzed NPs the loss is slightly higher due to the combustion of adsorbed organic species/surfactant.

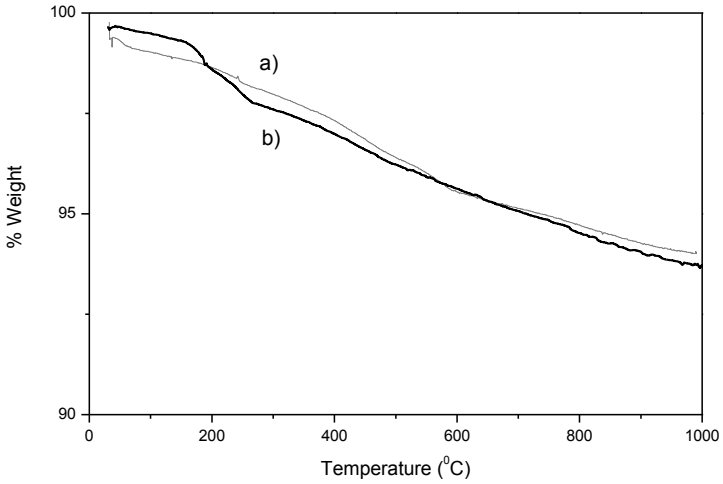

Figure 3.49 TGA thermograms of synthesized Mn_3O_4 NPs hydrolysed using **(a)** NaOH, and **(b)** TMAOH.

3.2.2.1.6 EPR Analysis

To investigate the magnetic properties of the Mn_3O_4, EPR analysis was performed and the results are shown in Figure 3.50. EPR analysis is very helpful in understanding magnetic interactions and influences of nanostructuring in order to compare and contrast with the reported results for bulk Mn_3O_4.

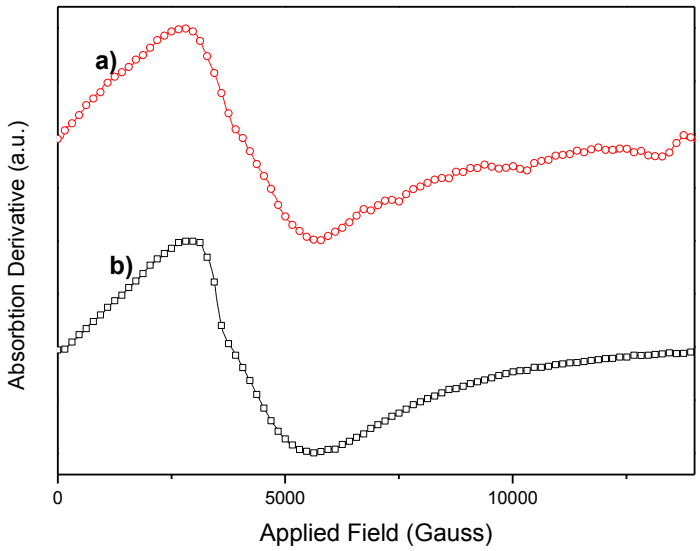

Figure 3.50 First derivative of EPR signal for samples hydrolzed with (**a)** TMAOH and (**b)** NaOH.

The hyperfine spectrum expected for Mn^{+2} and Mn^{+3} is not resolved. The broad EPR lines are observed with linewidths of 2932 and 2731 Gauss at resonance fields of 4107 and 3883 Gauss for TMAOH and NaOH hydrolyzed samples respectively. This broad line for Mn_3O_4 may be attributed to the strongly interacting Mn^{+2} ions and is explained as convolution of the different resonance fields due to the distribution of local effective fields during dipolar interactions between particles as suggested by Winkler et al. [128]. Moreover, in our study, samples have a broad range of particle sizes (6 nm for NaOH and 14 nm for TMAOH hydrolyzed sample primary particle size and ~250 nm measured hydrodynamic radius due to strong aggregation) which can cause wide range inter-particle and intra-particle interactions for smaller particles including cluster of free spins located at surface. All these effects may cause broad EPR lines. The g values are obtained as 1.71 and 1.80 for TMAOH and NaOH hydrolyzed samples respectively, which are smaller than that of bulk Mn_3O_4 (2.01). This may be caused by the exchange-coupled system with unlike spins such as canted spin at surface of particles.

3.2.2.2 Hydrothermal route with H_2O_2

3.2.2.2.1 XRD Analysis

Identification of the crystalline phases present was performed by XRD analysis and the patterns of the as-synthesized powders are shown in Fig. 3.51. All diffraction peaks were

indexed to the tetragonal hausmannite crystal structure model of Mn_3O_4 (ICDD Card no. 24-0734). The line profile, shown in Fig.1, is fitted for 14 peaks with the following Miller indices: (112), (220), (013), (211), (004), (220), (204), (015), (312), (303), (321), (224), (400), and (206). As a result a *D* of 16 ±9 nm was obtained for as-synthesized Mn_3O_4 NPs.

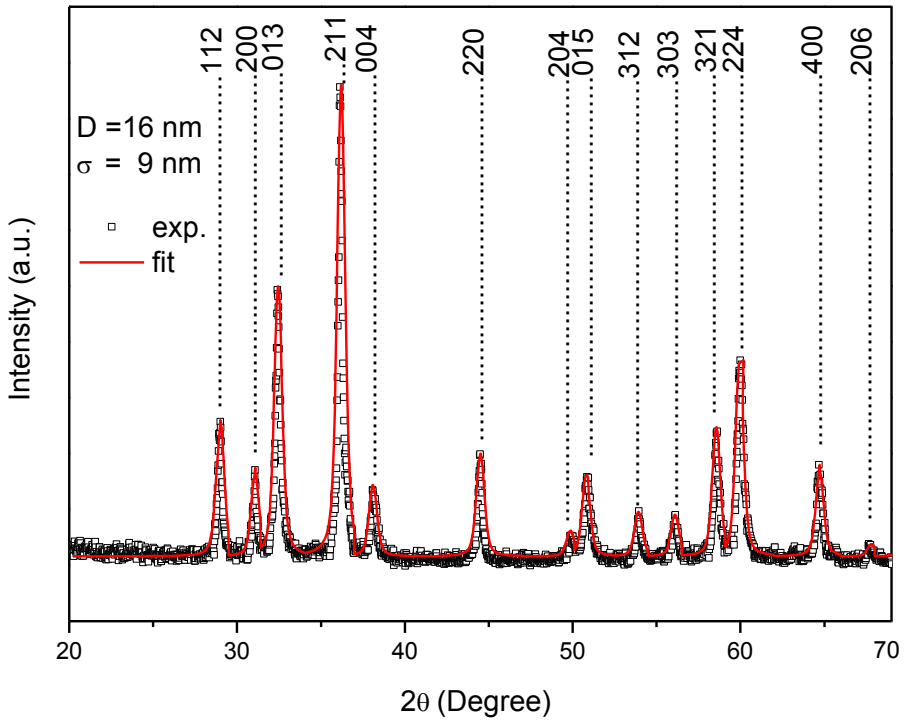

Figure 3.51 XRD pattern and line profile fitting of Mn_3O_4 NPs.

3.2.2.2.2 FTIR Analysis

FTIR analysis performed for the prepared sample and results are presented in Fig. 3.40. Two absorption bands observed at 620 and 505 cm^{-1}, are associated with the coupling between Mn-O stretching modes of tetrahedral A- and octahedral B- sites [126,127] as expected from normal spinel structure. Thus, the FTIR spectrum further confirms that the product is Mn_3O_4.

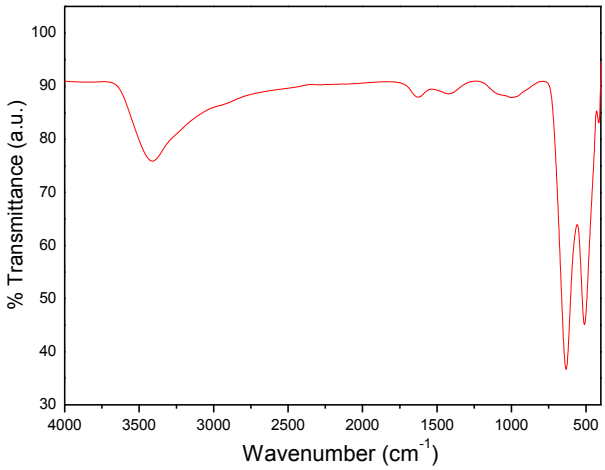

Figure 3.52 FTIR spectra of as-synthesized Mn_3O_4 NPs.

3.2.2.3 Hydrothermal route with PVP

3.2.2.3.1 XRD Analysis

A typical XRD pattern of the as-synthesized Mn_3O_4 powder is shown in Fig. 1. All diffraction peaks were indexed to the tetragonal Mn_3O_4 (which are consistent bulk value ICDD Card no. 24-0734). The line profile, shown in Fig.1, is fitted for 14 peaks with the following Miller indices: (112), (200), (013), (211), (004), (220), (204), (015), (312), (303), (224), (321), (116), and (400). As a result the average size of the crystallites, *D* 16 ± 5 nm was obtained for as-synthesized Mn_3O_4 nanocrystals.

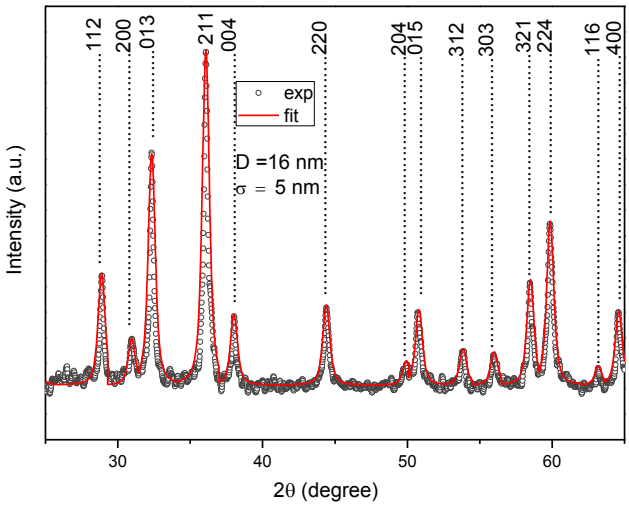

Figure 3.53 XRD pattern of PVP coated Mn_3O_4 NPs.

3.2.2.3.2 FTIR Analysis

The band at 1661 cm^{-1} is attributed to the C=O stretching of neat PVP structure (Fig.3.54a) and its shift to lower wavenumbers (lower energies) should be due to the chemical interaction between the PVP molecules and Mn_3O_4 NPs surface. This result represents a strong evidence that this interaction occurs through the C=O groups of PVP [137, 138]. The similar interaction was also observed between 2-pyrolidone and Co_3O_4 NP's [139] and L-Lysine and Fe_3O_4 NP's [116]. The broadness of the FTIR peak at around 3500 cm^{-1} also proves the existence of H-bonding among pyrrolidone molecules. In addition, FTIR spectra of the particles exhibit characteristic peaks of Mn_3O_4 at around ν_1 = 613 cm^{-1} ν_2 = 503 cm^{-1} [126,127] respectively. The band at 1384 cm^{-1} can be assigned ν_1 vibrations of CO_2 molecules that are present in the sample chamber [51].

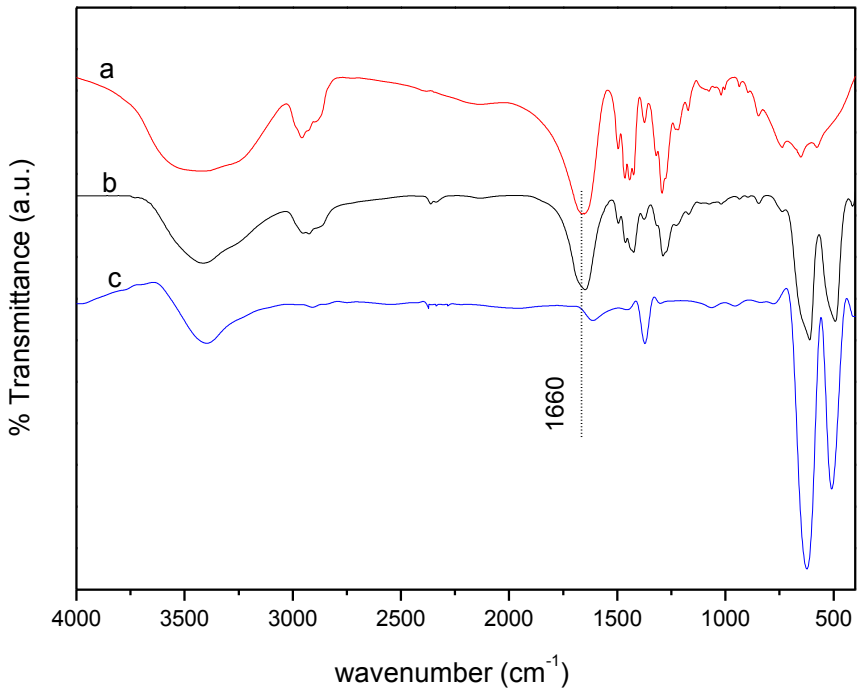

Figure 3.54 FTIR spectrum of **a)** PVP, **b)** PVP coated Mn_3O_4 NPs, and **c)** Mn_3O_4.

3.2.3 Egg-white (ovalbumin) assisted route[5]

3.2.3.1 XRD Analysis

A typical XRD pattern of the as-synthesized Mn_3O_4 powder is shown in Fig. 3.55. All diffraction peaks were indexed to the tetragonal Mn_3O_4 (which are consistent bulk value ICDD Card no. 24-0734). The lattice parameter was computed as a = 5.76(3), b = 9.47(1) Å using the d-spacing values and the respective (hkl) parameters. The average size of the crystallites, D_{XRD}, was estimated as 22 ± 10 nm from the diffraction pattern using the line profile fitting. The line profile, shown in Fig. 3.55, is fitted for 14 peaks with the following Miller indices: (101), (112), (200), (013), (211), (004), (220), (213), (204), (015), (312), (303), (321) and (224).

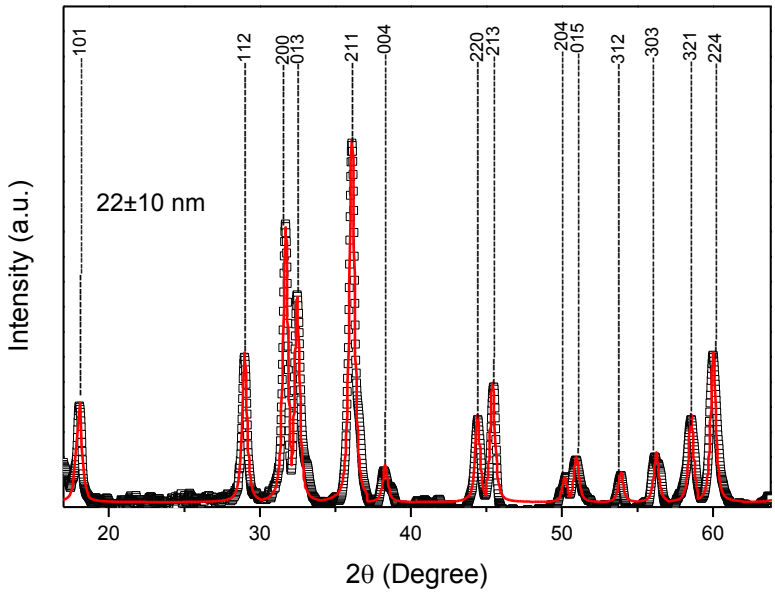

Figure 3.55 XRD pattern of Mn_3O_4 particles (obtained upon calcination of dried gel precursor at 800 ^oC) and line profile fitting.

3.2.3.2 FTIR Analysis

FTIR analysis was performed for the sample prepared by the calcination of the dried gel precursor and the spectrum is presented in Fig. 3.56. In the range of 1000 - 400 cm^{-1}, two

[5] Z. Durmus, A. Baykal, H. Kavas, M. Direkci, M.S. Toprak, **"Ovalbumin mediated synthesis of Mn_3O_4"**, Polyhedron 28 (2009) 2119–2122.

main metal-oxygen bands at ~606 cm^{-1} and 478 cm^{-1} were observed in the FT-IR spectrum which are associated with the coupling between Mn-O stretching modes of tetrahedral A- and octahedral B- sites [126,127].

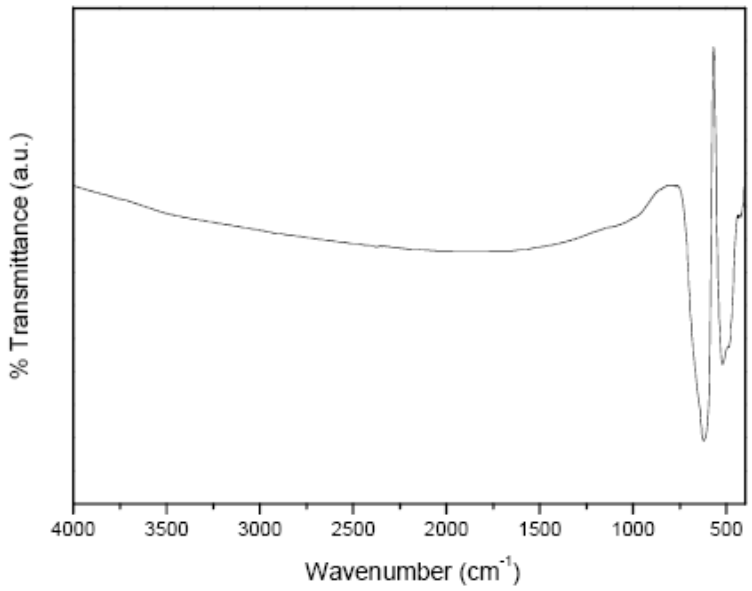

Figure 3.56 FTIR spectrum of as-synthesized Mn_3O_4 NPs upon calcination of the dried gel precursor at 800 ^oC.

3.2.3.3 Thermal Analysis

Thermal stability of the precursor powder and final powder has been analyzed using TGA. Thermograms for both samples are presented in Fig. 3.57. Calcined powder shows no weight loss, as all organic residues have been removed, that reveals the stability of obtained Mn_3O_4 NPs. Precusor powder shows an overall weight loss of ~75%. According to the differential thermogram, DTG, presented in the inset of Fig. 3.57 there is four-step weight loss (indicated with arrows) for the precursor powder, of mainly ovalbumin, matrix the first one at < 200 ^oC, a shoulder at ~240 ^oC, the most intense one at ~300 ^oC and a secondary shoulder one at ~450 ^oC. The observed thermogram perfectly matches that of pure ovalbumin reported by Kumari et al. [140] above 200 ^oC. Weight loss up to 200 ^oC is due to the adsorbed water and boiling of organic residues released from Mn salts. Weight loss around ~240 ^oC suggests that water molecules in albumin are strongly bonded to the protein molecules and

that it takes higher energies to remove them. The considerable weight loss at ~300 ^{o}C and the shoulder at ~450 ^{o}C is due to the decomposition of proteins in ovalbumin.

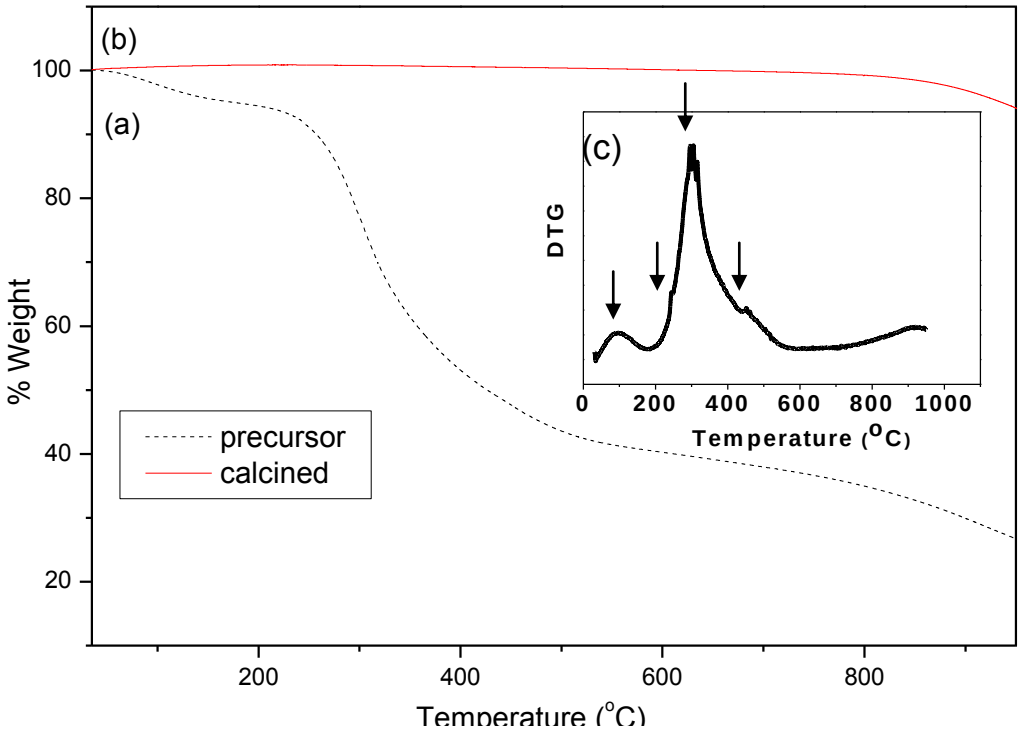

Figure 3.57 TGA thermograms of **(a)** as-made dried gel precursor; **(b)** final powder after calcination of dried gel precursor; and **(c)** differenteial thermogram, DTG, of the precursor in (a).

3.2.3.4 SEM Analysis

SEM analysis was performed to investigate morphology of synthesized Mn_3O_4 powder and micrographs are shown in Fig. 3.58. Smooth and well defined particles with sizes ranging from ~150 nm up to ~2 μm were observed in the micrographs. The particle size is much larger compared with the crystallite size obtained from XRD indicating the polycrystalline nature of the observed particle morphologies.

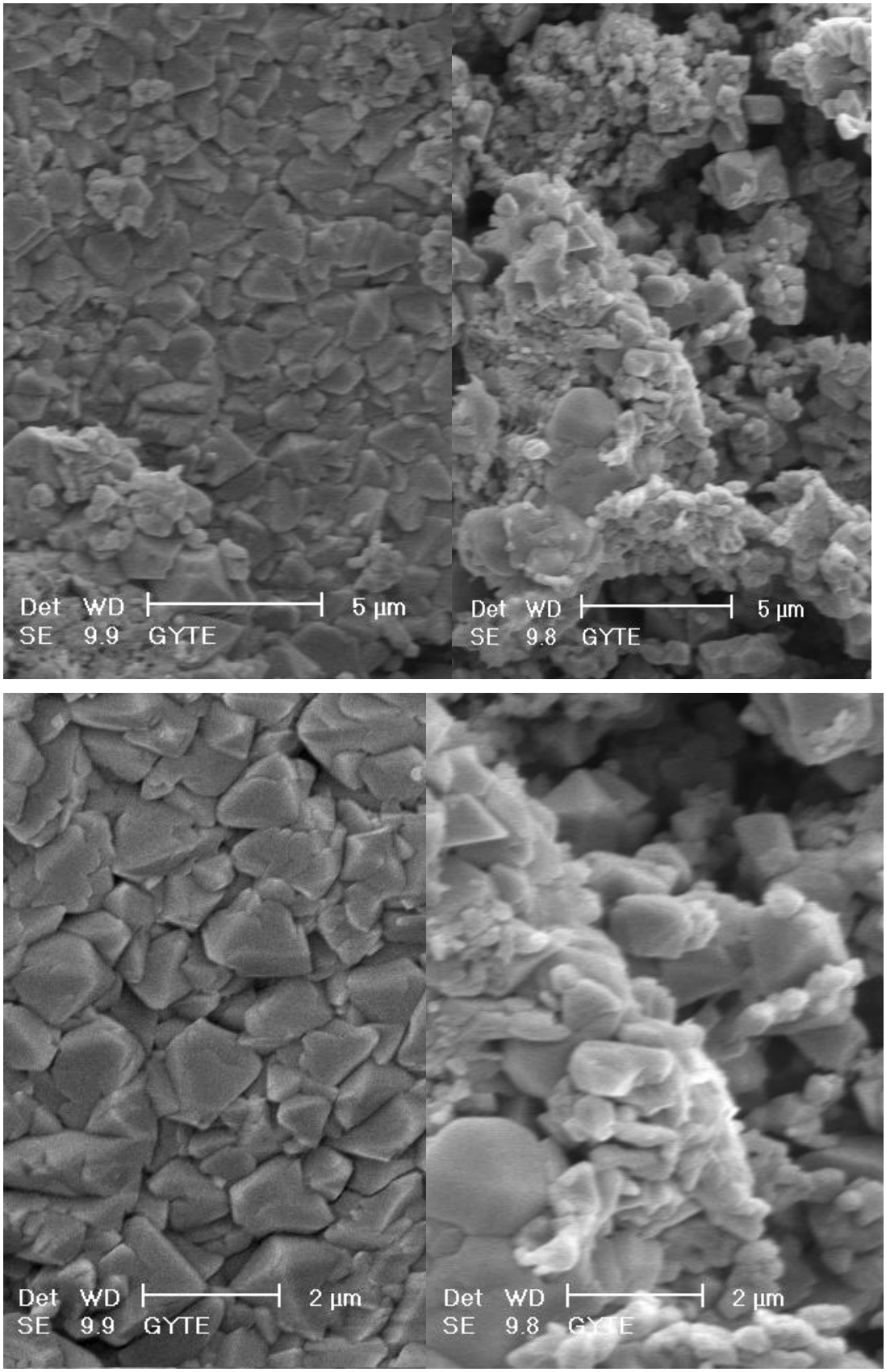

Figure 3.58 SEM micrograph of Mn_3O_4 particles obtained upon the calcination of the precursor at 600 ^oC.

3.2.3.5 TEM Analysis

Morphology of Mn_3O_4 particles were also investigated by TEM and a micrograph is presented in Fig. 3.59. which shows a strong agglomeration. Even though particles have lateral dimensions on the order of 1-2 μm levels, their high transparency under TEM reveals a sheet like morphology.

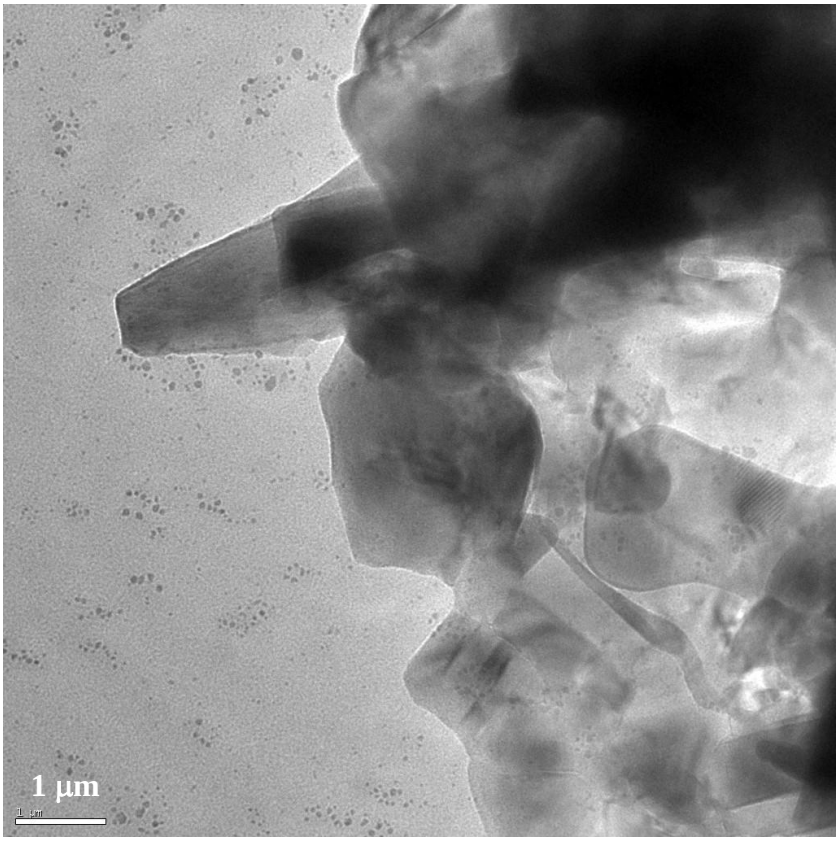

Figure 3.59 TEM micrograph of Mn_3O_4 particles obtained upon calcination of the dried gel precursor at 800 ^oC.

3.2.3.6. EPR Analysis

The magnetic properties of the as-synthesized Mn_3O_4 were measured using EPR technique in X band and the resultant spectrum is presented in Fig. 3.60. The EPR spectrum can be used to detect Mn^{2+} and Mn^{4+}, whereas Mn^{3+} is usually not detected due to the complete splitting of the energy levels (no ground state degeneracy) [141].

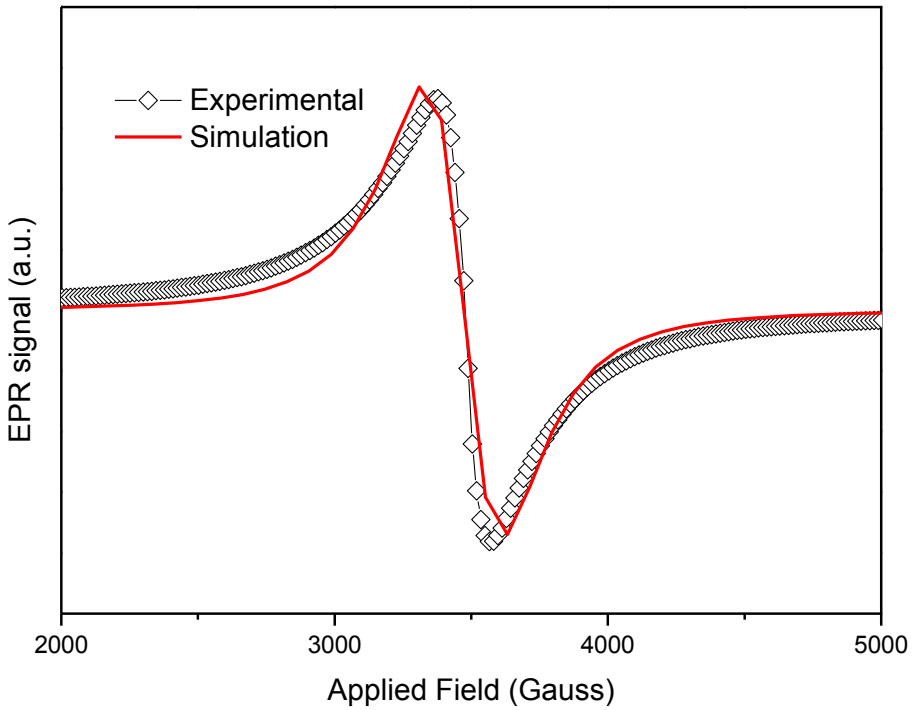

Figure 3.60 First derivative of EPR signal (◊) and simulation (-) for Mn_3O_4 particles obtained upon calcination of the dried gel precursor at 800 ^oC.

Fig. 3.60 shows room temperature EPR spectrum of Mn_3O_4 including a narrow and symmetric line with its Gaussian simulation signal. The hyperfine splitting is not observed. EPR lines have a peak to peak line-width of 195 Gauss, resonance field of 3475 Gauss and g value of 2.01. Srinivasan et al. [142] has reported on the temperature dependence of ΔH, Hr, and g parameters of Mn_3O_4 in detail. Our results are in accordance with their room temperature observations, where ΔH, Hr, and g have been reported as 405 Oe, 3170 Oe and 2.01 at 9 GHz. Huber et al.[143] suggested effective g value of the unlike spin in the exchanged-coupled system as follows (equation 1):

$$g_{eff} = \frac{g_A S_A(S_A+1)N_A + g_B S_B(S_B+1)N_B}{S_A(S_A+1)N_A + S_B(S_B+1)N_B} \qquad (1)$$

where g_A and g_B are the g values, S_A and S_B are spin moments, N_A and N_B are the relative concentrations of A and B sites, respectively. At $Mn^{+2}[Mn^{+3}]_2 O_4$, by assuming that Mn^{+2} has $g_A = 2$ and using $S_A = 5/2$ and $S_B = 2$ are spin moments, $N_A = 1$ and $N_B = 2$ and experimental g value as $g_{eff} = 2.01$, the Mn^{+3} in B site has g value 2.02 that means unquenched orbital moment resulting unsplitted EPR line [142]. EPR spectrum and exchange coupled equation reveal the absence of hyperfine splitting in the final powder.

3.2.4 Direct ultrasonic-assisted route and capping with CTAB

3.2.4.1 XRD Analysis

XRD pattern of the as-synthesized Mn_3O_4 powder is shown in Fig. 3.61. All diffraction peaks were indexed to the tetragonal hausmannite crystal structure model of Mn_3O_4 (which are consistent bulk value—ICDD Card no. 24-0734). No extra peaks of impurities indicating other forms of manganese oxides were detected. The line profile, shown in Fig.3.61, is fitted for 14 peaks (112), (200), (103), (211), (004), (220), (204), (015), (312), (303), (321), (224), (116), and (400). The average crystallite size, D and σ, were estimated as 13 ± 5 nm and 17 ± 5 nm for Mn_3O_4 and CTAB capped Mn_3O_4 samples respectively.

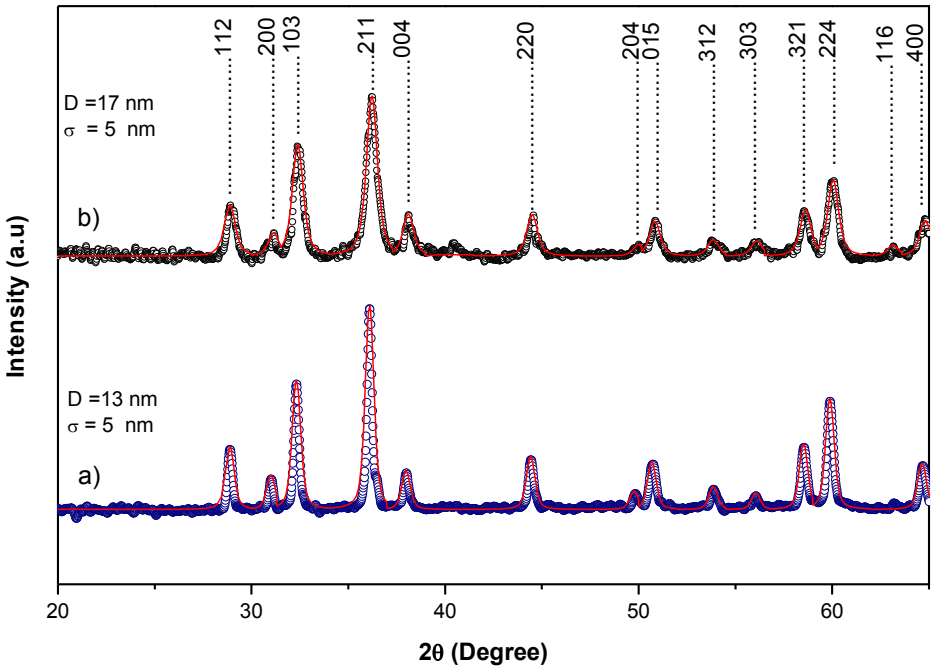

Figure 3.61 X-ray powder diffraction pattern (◌) and line profile fitting (solid line) for **a)** Mn_3O_4 and **b)** CTAB capped Mn_3O_4.

3.2.4.2 FTIR analysis

At Fig. 3.62 Mn_3O_4 two broad peaks at 3424 and 1638 cm^{-1} occur due to presence of N-H groups and a small amount of adsorbed water. The IR bands at 1047 cm^{-1} and 1440 cm^{-1} should be attributed to the absorption of the ethanol molecules on the surface of the hausmanitte particles. Two absorption bands are observed at 628 and 510 cm^{-1}, associated with the coupling between Mn-O stretching modes of tetrahedral and octahedral sites [126, 127] as expected from normal spinel structure.

FTIR data of pure CTAB and Mn_3O_4/CTAB nanocomposite (surface bound CTAB molecules) give some indications about the formation of Mn_3O_4/CTAB nanocomposite. The CH_2 symmetric and asymmetric stretching vibrations of CTAB bound on Mn_3O_4 NPs, respectively, lie at 2850 and 2917 cm^{-1}, the same as those of pure CTAB. This confirms inclusion of the surfactant molecules [144]. The unchanged frequency positions suggest that there is no intermolecular interaction enhanced due to capping effect, and the conformation methylene chains is maintained [145, 146]. The singlets at 962 cm^{-1} for pure CTAB and small peak at 1004 cm^{-1} for bond CTAB belong to C-N+ stretching bands, and the frequency shift is believed to be caused also by interactions between N-containing group and the metal surface. The change of CH_2 rocking mode from a doublet at 730 and 719 cm^{-1} for pure CTAB to a singlet at 717 cm^{-1} in the product also denotes a confinement effect of CTAB in capping structure. All these experimental observations illuminate that CTAB molecules capped the Mn_3O_4 via their headgroups.

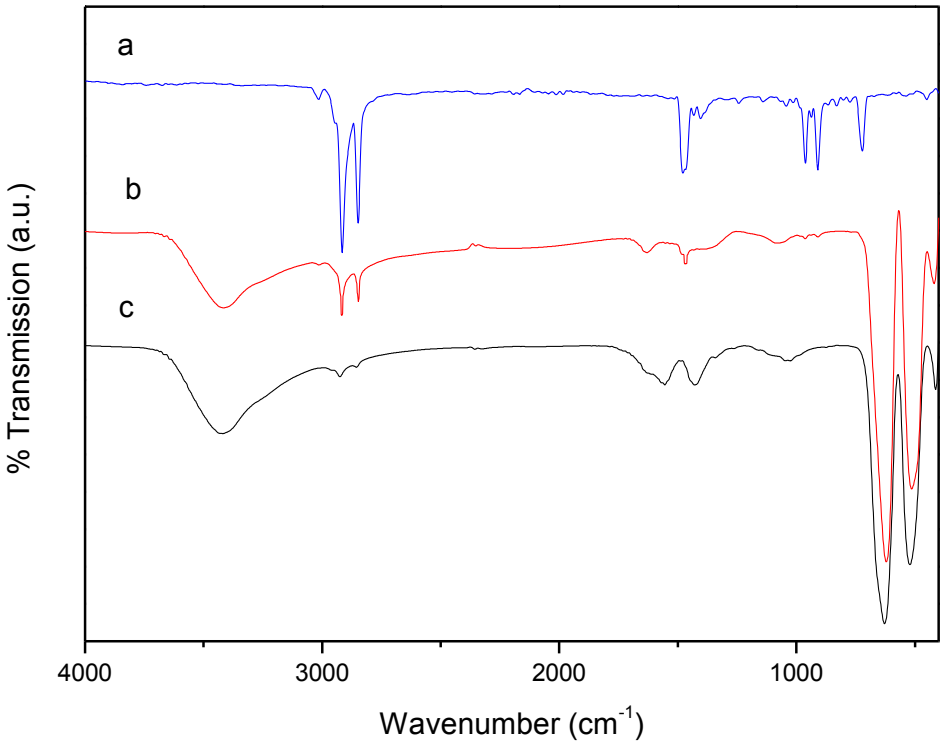

Figure 3.62 FTIR analysis of **a)** CTAB, **b)** CTAB capped Mn_3O_4, and **c)** pure Mn_3O_4.

3.2.4.3 Thermal Analysis

TGA curve of pure Mn_3O_4, CTAB-Mn_3O_4 nanocomposite and pure CTAB were presented in Fig.3.63 a, b, and c. First of all, there is very small weight change due to the moisture of pure Mn_3O_4 NPs (Fig.3.63a). Thermal decompositon of pure CTAB (Fig.3.63c) was observed in 207-316 ^oC temperature with 100 % weight loss. For nanocomposite (Fig.3.63b), between room temperature and 200 ^oC, a weight loss about 2 wt % is attributed to the evaporation of physisorbed water and lossely coordinated water in the interlayer [147a] and a weight loss of about 10 wt % in the range of 200-500 ^oC is due to the decomposition of CTAB outer layer [147b]. Therefore, it is also confirmed by TGA that the surface of Mn_3O_4 NPs were capped with CTAB.

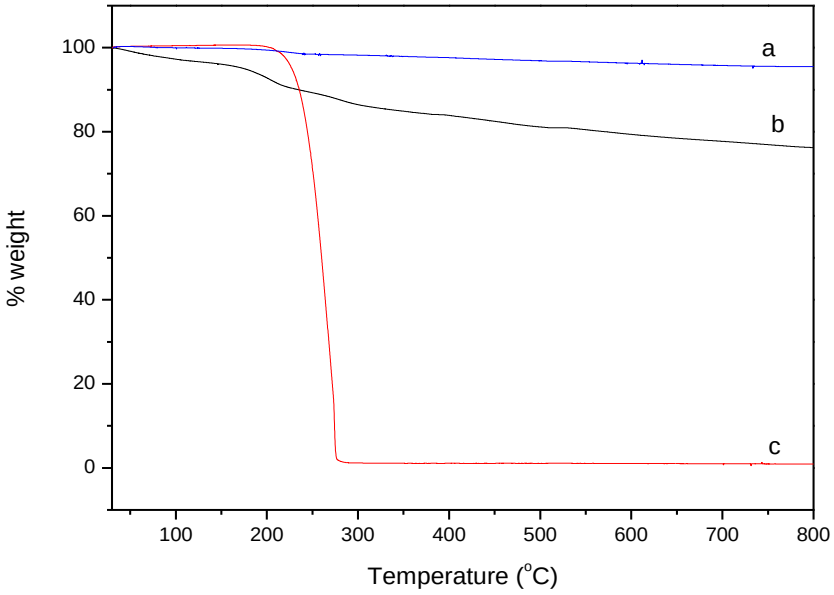

Figure 3.63 TGA thermograms of synthesized **a)** pure Mn_3O_4, **b)** CTAB capped Mn_3O_4, and **c)** CTAB.

3.2.4.4 NMR Analysis

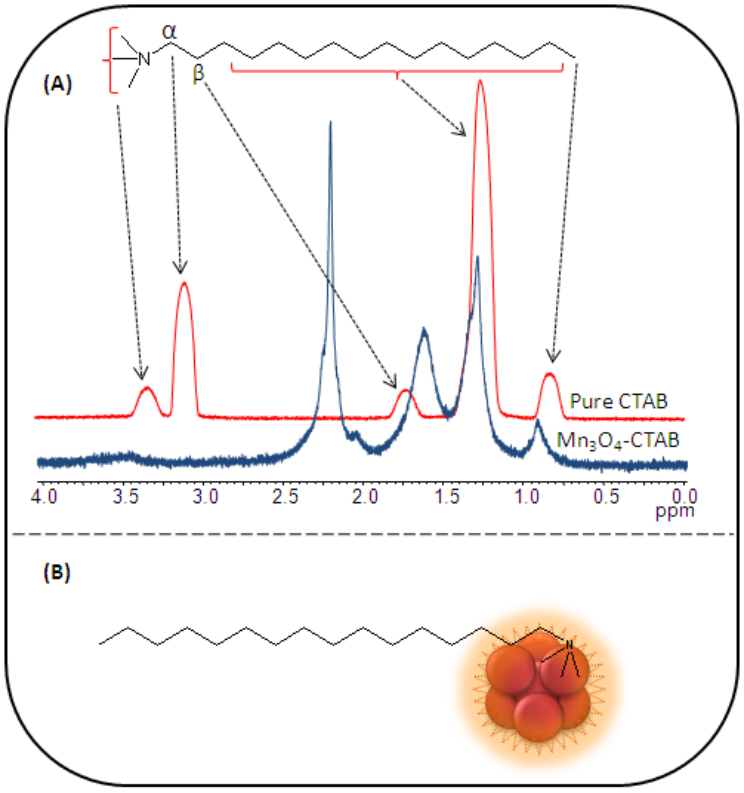

Figure 3.64 (A) H^1 NMR spectra for pure CTAB and CTAB capped Mn_3O_4 and **(B)** A model for a single CTAB capped Mn_3O_4-CTAB resulted from NMR test.

Proton NMR spectra of pure CTAB and CTAB capped Mn_3O_4 in Fig. 3.64A clearly show that the interaction and the position of CTAB on Mn_3O_4 NPs. The resonance peaks at δ 3.10 for pure CTAB and at δ 2.20 for CTAB capped Mn_3O_4 were corresponded to the methyl protons of -N-$(CH_3)_3$ group. The large chemical shift changes of these methyl protons indicate that the interaction between CTAB and Mn_3O_4 is mainly located around -N-$(CH_3)_3$ head group. Also, the peaks at δ 3.30, 1.71 for pure CTAB and at δ 2.10, 1.62 for CTAB capped Mn_3O_4 were corresponded to protons on α-CH_2 and β-CH_2 and the downfield of chemicals shift show another interaction between CTAB and Mn_3O_4, respectively. The peaks at δ 1.24 and 0.82 are the combined resonances of the other methylenes in the main chain for both spectra [148-150]. After the comparison of the chemical shifts of the pure CTAB and CTAB capped Mn_3O_4, it was concluded that the CTAB molecules were capped on the Mn_3O_4 NPs through their head groups, as shown in Fig. 3.64B.

3.2.4.5 EPR Analysis

The magnetic properties of Mn_3O_4 nanocrystals and CTAB capped ones have been studied by FMR at low temperatures. The broad EPR lines without hyperfine spectrum are observed, which are caused by the dipolar interactions between particles and their different resonant fields with distributed local effective fields. The capping can not overcome the interparticle interactions or the particles have not single crystal nature so the splitted EPR lines were not observed. The magnetic behaviour of samples were studied at two different temperature regime: high temperature regime (HT) is above 50 K up to room temperature and low temperature regime (LT) is below 50 K. The typical first derivative of absorbtion power versus applied magnetic field curves at HT region for both Mn_3O_4 and CTAB capped Mn_3O_4 samples are shown in Fig. 3.65, from which one can see that samples reach the resonance at lower fields by decreasing temperature with increasing linewitds. However, it can be seen that the applied power is not sufficient for the CTAB capped Mn_3O_4 and it is same with the power applied for Mn_3O_4 particles why it is aimed to compare the effect of caption at equivalent experimantal conditions. So the FMR spectra of capped one vanish and close to the noise signals at lower temperature and give limited information about linewidth and resonance field. The resonance field of Mn_3O_4 goes the smaller fields while the peak to peak linewidth increasing by decreasing temperature.

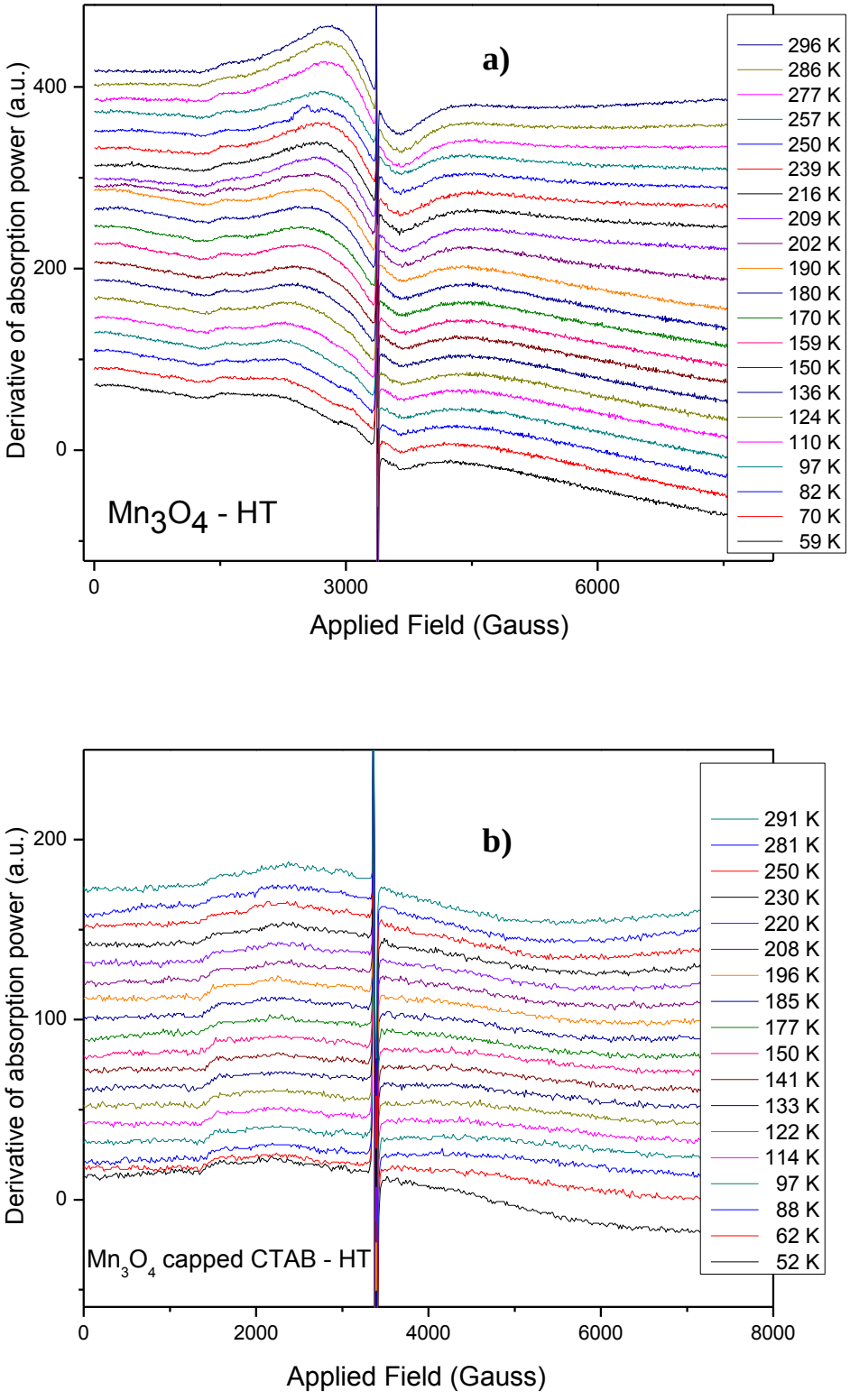

Figure 3.65 FMR spectra of **a)** Mn_3O_4 NPs at high temperature, **b)** CTAB capped Mn_3O_4 NPs at high temperature.

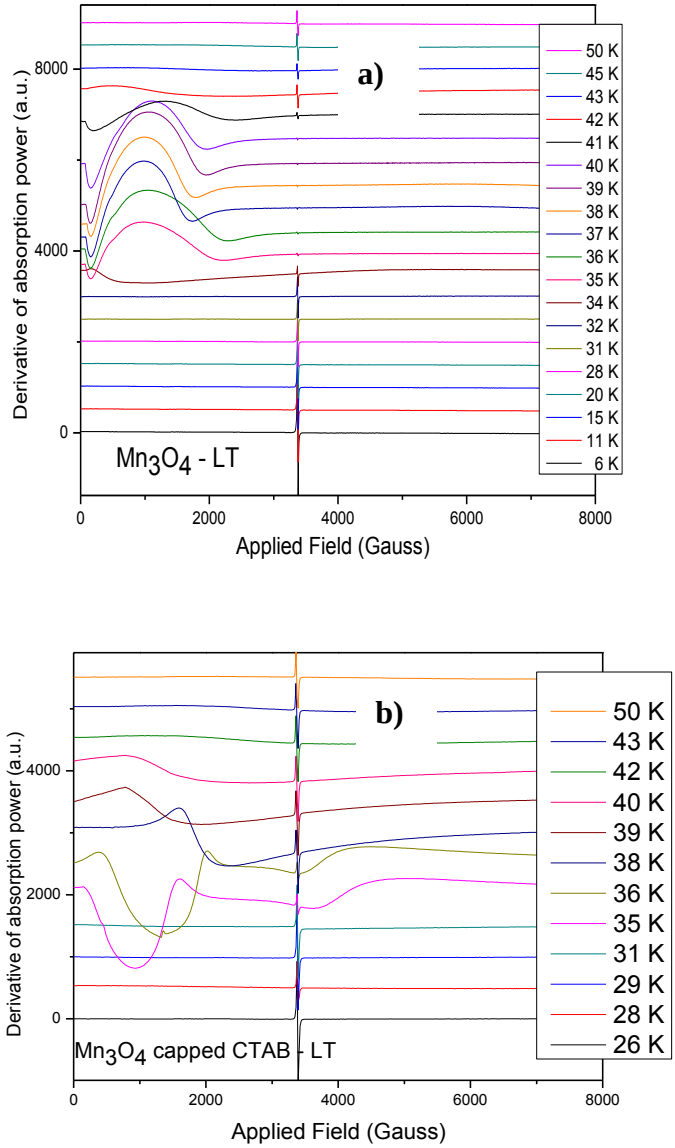

Figure 3.66 FMR spectra of **a)** Mn_3O_4 NPs at low temperature and **b)** CTAB capped Mn_3O_4 NPs at low temperature.

At temperatures lower than 50 K, the FMR specta of both Mn_3O_4 and CTAB capped Mn_3O_4 are shown in Figure 3.66 a and b. The broad and asymmetric FMR curves exist below 43 K assigned as a Tc-Cruie temperature for the Mn_3O_4 [151] There exists a broader and asymmetric second line close to the zero fields below 41 K for Mn_3O_4 and gives a more complex EPR spectrum. The main line coming from higher temperatures reaches resonance at lower fields by decreasing temperature, and also the new lines' resonance goes thorough the lower fields. These lines existing at higher and lower fields also detected in previous study [150] and were explained by favorably oriented particles with high field resonant property

while the anisotropic decreases some of particles' resonance at lower fields [151,128]. Below 37 K, convoluted EPR lines' resonance shift to the higher fields suddenly and other magnetic phase transition is occurred at this temperature. This magnetic transition was explained by Tackett et all. by spiral sutractured ordered spins of trivalent mn ions and also the vanishing line below 34 K, complex spins ordering of these ions with a net magnetic moment anti-parallel to the divalent Mn ions [152]]. These magnetic transitions can also be observed for the capped Mn_3O_4 not so clear as previous sample. It may be attributed the reducing effect of coating on applied and absorbed power of EPR signal. The double integrated EPR signal intensity of capped Mn_3O_4 is lower than that of Mn_3O_4 as shown in figure 3.66.

3.2.5 PANI/Mn_3O_4 Nanocomposites[6]

3.2.5.1 XRD Analysis

Crystallographic identification of the inorganic phase was performed by XRD analysis and the resultant diffraction pattern is presented in Fig. 3.67. XRD peaks of PANI/Mn_3O_4 nanocomposites (Fig.3.67b) are almost similar to the free PANI. But XRD powder pattern of Mn_3O_4 NPs (Fig.3.67a) presents the high crystallinity. According to Gemeay et al. this fact confirmed that a distortion in crystal structure of Mn_3O_4 has occurred during the polymerization reaction, which led to transformation of the crystalline Mn_3O_4 into the amorphous phase; therefore, the XRD peaks of PANI are predominant [153].

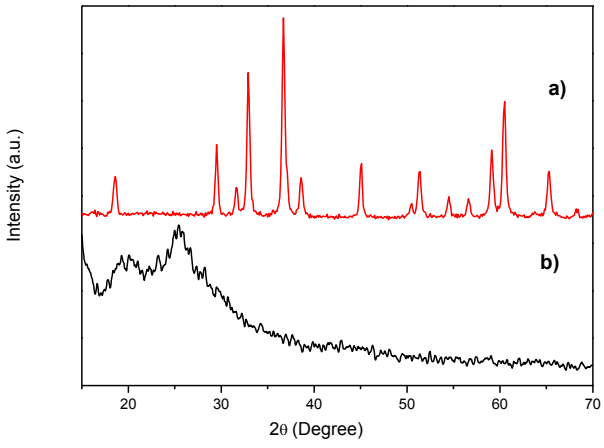

Figure 3.67 XRD powder pattern and line profile fitting for **a)** Mn_3O_4, **b)** PANI/Mn_3O_4.

[6]Z. Durmus, H. Kavas, A. Baykal, M. S. Toprak. **"Preparation and Characterization Polyaniline / Mn_3O_4 nanocomposite"**, Current Applied Physics (under view).

3.2.5.2 FTIR analysis

Fig. 3.68 shows the FTIR spectra of the Mn_3O_4, PANI/ Mn_3O_4 nanocomposite and pure polyaniline. In Fig. 3.68a two broad peaks at 3424 and 1638 cm^{-1} are due to presence adsorbed water on the surface of the product. The IR bands at 1047 cm^{-1} and 1440 cm^{-1} are attributed to the absorption of the ethanol molecules on the surface of the hausmanitte particles. Two absorption bands are observed at 628 and 510 cm^{-1}, associated with the coupling between Mn-O stretching modes of tetrahedral and octahedral sites [154,155] as expected from normal spinel structure.

Fig. 3.68b and 3.68c show the IR spectra of PANI and PANI/ Mn_3O_4 nanocomposite [156-162]. The peaks at 1564 and 1488 cm^{-1} are attributed to the characteristic C═C stretching of the quinoid and benzenoid rings, the peaks at 1303 and 1246 cm^{-1} are assigned to C—N stretching of the benzenoid ring, the broad peak at 1143 cm^{-1} which is described by MacDiarmid et al.[38] as the "electronic-like band" is associated with vibration mode of N=Q=N (Q refers to the quinonic-type rings) and the peak at 804 cm^{-1} is attributed to the out-of-plane deformation of C—H in the *p*-disubstituted benzene ring.

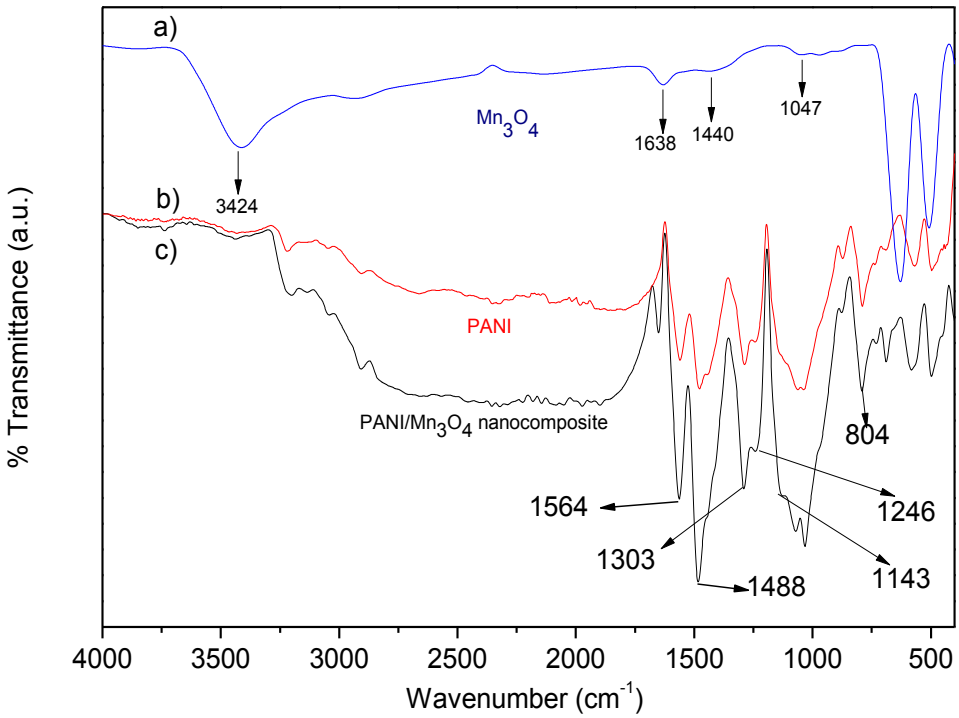

Figure 3.68 FTIR spectra of **a)** Mn_3O_4, **b)** PANI, and **c)** polyaniline/Mn_3O_4 nanocomposite.

3.2.5.3 Thermal Analysis

Thermal stability of Mn_3O_4, PANI, and PANI/Mn_3O_4 nanocomposite was analyzed by TGA and thermograms are presented in Fig. 3.69. Mn_3O_4 NPs shows no significant weight loss in the temperature interval of the measurement. Samples of Mn_3O_4, and PANI/Mn_3O_4 nanocomposite show similar trends in their stabilities, loosing weight due to adsorbed and/or crystalline water up to 200 ^oC and a continous weight loss, with a similar slope, up to 1000 ^oC due to the degradation of the polymer backbone. Weight loss have not stabilized even at the upper limit of the measurement tempeartures.

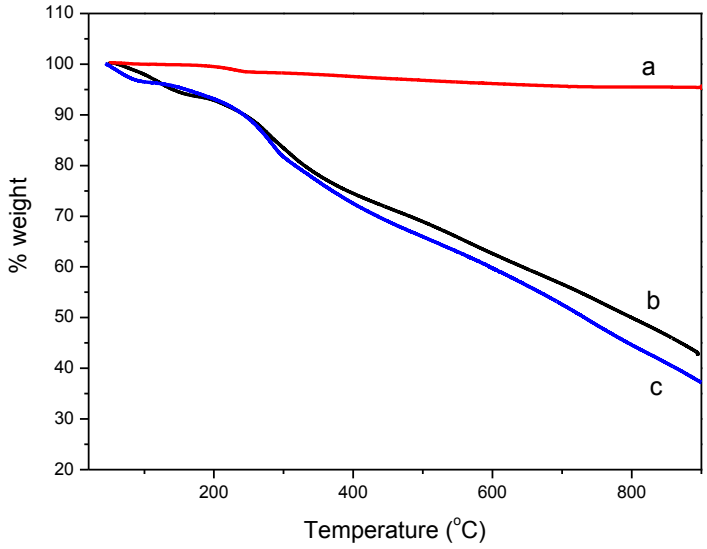

Figure 3.69. TGA thermograms of **a)** Mn_3O_4 NPs, **b)** PANI and **c)** PANI/Mn_3O_4 nanocomposite.

3.2.5.4 SEM Analysis

This image in Fig.8 indicates that Mn_3O_4 NPs exhibit a sheet-like morphology and consist of numerous flower-like aggregates with multi-leaves where each flower is made up many thin nanosheets with th ickness of ~2-3 nm assembled to form the observed architecture [163,164]. Such flower-like morphology is similar to the one described by Pan [165], which deemed that the nanosheets were spokewise, projected from a common central zone.

Figure 3.70 SEM micrograph of PANI/Mn_3O_4 nanocomposite.

3.2.5.5 Conductivity and Dielectric Measurements

3.2.5.5.1 Conductivity Measurements

Conductivity characteristics of PANI and Mn_3O_4 NPs are presented in Fig. 3.71. The total conductivity ($\sigma_{total} = \sigma_0 + \sigma(\omega)$) is sum of DC conductivity due to the band conuction and AC conductivity due to the hopping conduction mechanisms. While the former is frequency independent, the latter is frequency dependent with the relation of $\sigma(\omega) = B(T)\omega^{s(T)}$. Here the first term is temperature dependent constant and the powers of angular frequency gives information about the hopping mechanisms correletion [166]. AC conductivity of PANI is found temperature independent in the temperature range of 20-100 ^oC and increasing exponentially with increasing frequency above 0.2 MHz. At lower frequencies, it has non-varying charactersitics at all operated temperatures and frequencies. Generally it has a conductivity in the order of 10^{-5} S cm^{-1}. The conductivity of PANI base was found in the varying order of 10^{-8} – 10^{-11} S cm^{-1} and also the causes of variation was explained briefly by method of preparation [167]. Bilinova et al. [168] have studied conductivity of the partially reprotonated PANI and found it in again varying order of 10^{0} – 10^{-9} S cm^{-1}. Moreover, Zhang [169] reported that the conductivity of emeraldine salt pellets ranges from 10^{-4} to 10^{2} S cm^{-1}. By considering the effect of preperation methods [167], intrinsic properties such as; molecular weight, morphology and crystallinity, and, extrinsic properties such as; the dopants [169], the conducting PANI in such broad order between standart polymer (10^{-9} S cm^{-1}) and semiconductors (10^{0} S cm^{-1}) can be obtained. Also the varying conductivity of PANI by

pressing conditions during pellete formation such as the pressure, pressing time and the time intervals between pressing and testing, are reported in some studies [170, 171].

While Mn_3O_4 nanopartiles has temperature and frequency dependent Ac conductivity above 100 Hz and below 80 ^oC, its conductivity becomes independent of temperature and frequency at lower frequencies and higher temperatures. The temperature characteristic of Ac conductivity can be seperated into three different regions; *i*) $T \leq 30\ ^oC$, *ii*) $70\ ^oC > T > 40\ ^oC$ and *iii*) $T \geq 80\ ^oC$. At lower temperatures (region *i*), conductivity increases with increasing frequency with a small slope change at ~100 kHz. This increasing conductivity can be attributed to electronic exchange occuring between Mn^{+2} and Mn^{+3} existing in sublattice of spinel lattice. At moderate temperatures (region *ii*), there is an increasing tendency in conductivity curve between 100 and 50 kHz after which the conductivity reaches a plateu region. Lastly, conductivity of Mn_3O_4 does not change significantly at higher temperatures (region *iii*). The ionic or vacant sites charge carriers give low mobility systems such as spinel ferrites and the hopping process causes the major conduction [172,173]. Electron hopping takes place between the neighboring cations with two and three valence [174,175]. In this process, drift mobility of charge carriers increases by increasing temperature, and causes a decrease in DC resistivity. The influence of various parameters such as porosity, chemical composition, particle size [176,177] and cation distribution [178] on the conductivity of ferrites have been explained in earlier reports.

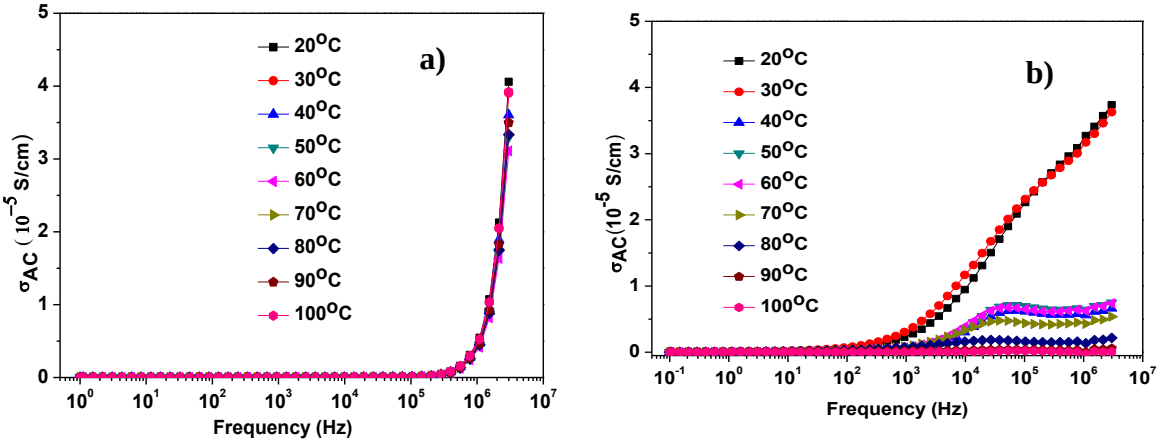

Fig. 3.71 Total conductivity of **a)** PANI and **b)** Mn_3O_4 NPs vs frequency.

Total conductivity of PANI/Mn_3O_4 nanocomposite is presented in Fig. 4.72. The PANI capped Mn_3O_4 composite has strongly temperature dependent conductivity behaviour. Above 100 kHz all conductivities increases sharply up to 1 MHz then the increase slows down at higher frequencies. The conductivity values are in the order of 10^{-3} Scm^{-1} which is

approximately 50 to 1000 times more/higher than that of uncapped Mn_3O_4 or PANI base with increasing temperature. The DC conductivity of composites inferred from plateaus region at lower frequencies and the arhenius plot of it gives activation energies of 22 meV at high temperature region and 65 meV at lower temperatures in Fig. 4.72.

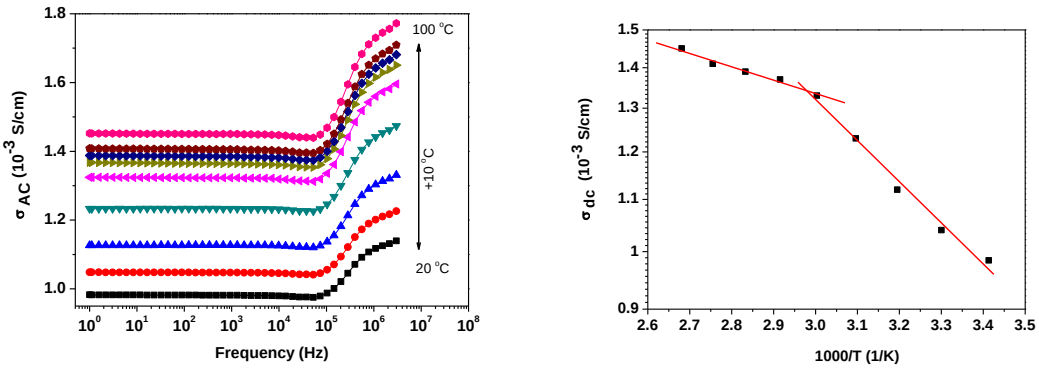

Fig. 3.72 Total conductivity of PANI/Mn_3O_4 nanocomposite.

3.2.5.5.2 Dielectric Measurements

The complex permittivity parameters $\varepsilon = \varepsilon' + i\,\varepsilon''$, were measured to determine the frequency and temperature dependency of stored (ε') and dissipated energies (ε'') by Mn_3O_4 and PANI/Mn_3O_4 presented in Fig. 3.73 and 3.74. Both ε' and ε'' decreases by increasing frequency and decreasing temperature. Koop's theory which is based on the Maxwell–Wagner model for the homogeneous double structure [172] is generally used to explain the dielectric characteristic of semiconductor like spinel structures such as ferrites. In Double structure model, the highly conducting grains are separated by relatively poor conducting grain boundaries and are found to be more effective at higher frequencies, while grains are more effective at lower frequencies [179]. The conductivity difference between grains and grain boundaries means different resistance causing the accumulation of charge carriers in separated boundaries and increase in dielectric constants. The polarization in Mn_3O_4 is through a mechanism similar to the conduction process by electron exchange between Mn^{2+} and Mn^{3+}, the local displacement of electrons in the direction of the applied field occurs and these electrons determine the polarization. With increasing frequency, the polarization decreases and reaches to a constant value due to the electron exchange between Mn^{2+} and Mn^{3+} cannot follow the alternating field. Previously, the large value of dielectric constant at lower frequency was attributed to the predominance of species like Mn^{2+} ions, oxygen vacancies, and grain boundary defects as being in ferrites [173]. The decrease in

dielectric constant with frequency is natural because of the fact that any species contributing to polarizability is found to show lagging behind the applied field at higher and higher frequencies [174].

The dielectric constants increase with increasing temperature as seen in semiconductors. Thermal energy convert the bound charges to the charge carriers, and increasing charge carrier concentration always gives easy alignment of dipoles in the applied AC electrical field and so increase in dielectric constants. Also by increasing the temperature the mobility of the charge carriers increases.

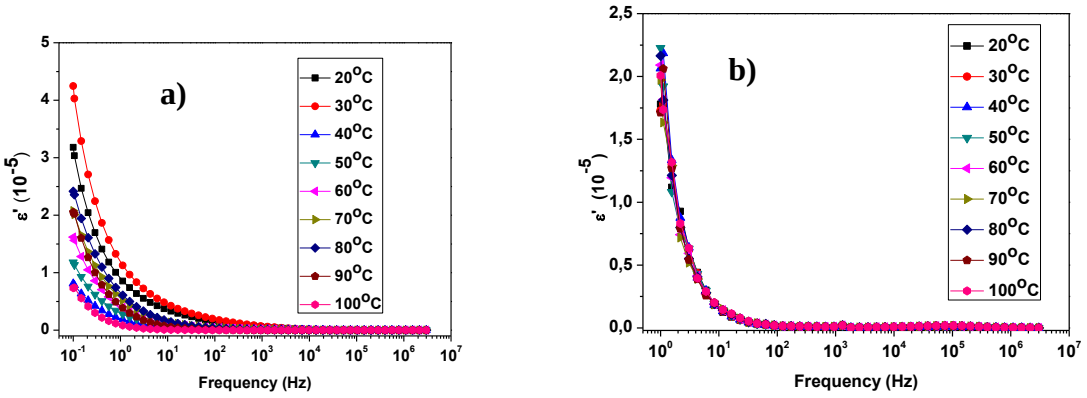

Figure 3.73 Real part of permitivity as a function of frequency at various temperatures for **a)** Mn_3O_4 NPs and **b)** PANI/Mn_3O_4 nanocomposite.

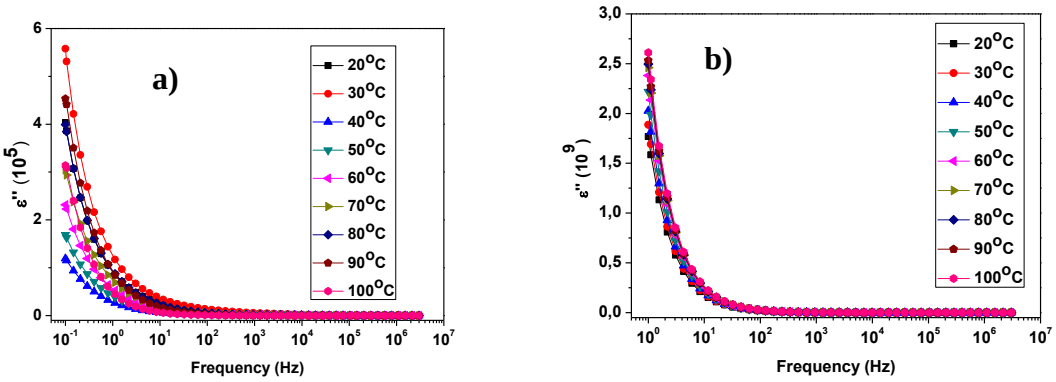

Figure 3.74 Imaginary part of permitivity as a function of frequency at various temperatures for **a)** Mn_3O_4 and **b)** PANI/Mn_3O_4 nanocomposite.

3.3 Co_3O_4 analysis

3.3.1 Egg-white (ovalbumin) assisted route[7]

3.3.1.1 XRD Analysis

XRD analysis was performed on the obtained powder and revealed that the only phase observed was Co_3O_4 spinel oxide with ICDD card no of 42-1467. No secondary phases or impurities were observed. (Fig.3.75). The sharpness of XRD peaks reveal high crystallinity of the NPs. The line profile, shown in Fig.1, was fitted for 8 peaks (111), (220), (311), (222), (400), (422), (511), (440) and the average crystallite size, D_{XRD}, was calculated as 45 ± 8 nm.

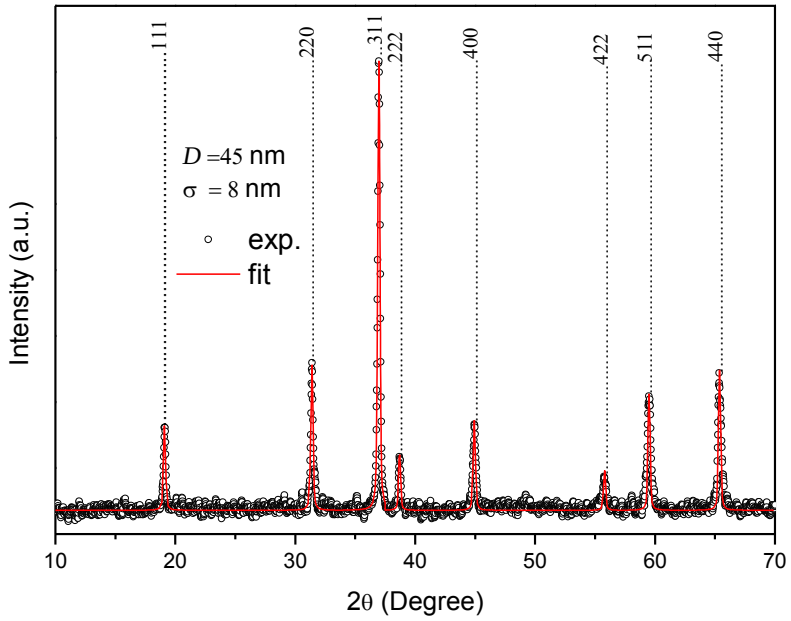

Figure 3.75 X-ray powder diffraction pattern (○) and line profile fitting (solid line) for the powder obtained after calcination of the dried gel precursor at 800 ^oC for 3 h.

Taking into account the cubic symmetry of the Co_3O_4, the lattice constant for each peak of each sample was calculated by using the formula: $a = d_{hkl} (h^2 + k^2 + l^2)^{1/2}$, where h, k, and l are miller indices for the same crystal-lattice planes. To determine the exact lattice parameter for each composition, Nelson-Riley method was used. The Nelson-Riley function $F(\theta)$ is given as $F(\theta) = 1/2[(\cos^2\theta / \sin\theta) + \cos^2\theta / \theta]$. The values of lattice constant a_o of all the

[7]T.O. Ahmadov, Z. Durmus, A. Baykal, H. Kavas, "**A simple approach for the synthesis of Co_3O_4 nanocrystals**", Inorganic Materials (under review).

peaks for each sample was plotted against *F(θ)* (not given). Then using a least square fit method exact lattice constant a_o was determined. The point where the least square fit straight line cuts the *y*-axis (where *F(θ) = 0*) is the actual lattice parameter of the composition which is obtained as a_o = 8.083(±4) Å.

3.3.1.2. FTIR analysis

The formation of the spinel Co_3O_4 structure was further supported by FT-IR spectrum presented in Fig. 3.76. The intensive broadband at ~3450 cm^{-1} and the less intensive band at ~1620 cm^{-1} are assigned to O–H stretching vibration interacting through H bonds. Traces of adsorbed or atmospheric CO_2 are evidenced by the very small absorption peak around 2340 cm^{-1}. In the range of 1000–100 cm^{-1}, two main metal–oxygen bands at ~662 cm^{-1} (ν_1) and ~570 cm^{-1} (ν_2) were observed in the FT-IR spectra given in Fig.3.76. These two bands are usually assigned to vibration of ions in the crystal lattices. The band at ~662 cm^{-1} corresponds to intrinsic stretching vibrations of the metal at the tetrahedral site (Co↔O), whereas the band at ~397 cm^{-1} is assigned to octahedral-metal stretching (Co↔O) [180,181].

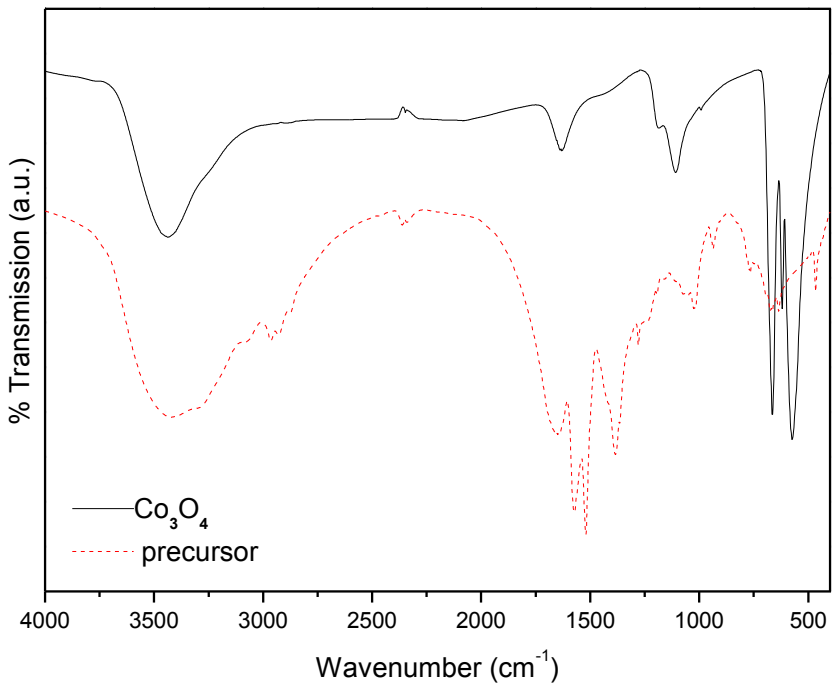

Figure 3.76 FTIR spectrum of **a)** precursor **b)** Co_3O_4 NPs obtained after calcination of the dried gel precursor at 800 ^oC for 3 h.

3.3.1.3 SEM Analysis

SEM analysis was performed in order to investigate the morphology of formed particles and understand the influence of the protein matrix on the shape of formations. Fig. 3.77 shows the SEM micrographs of Co_3O_4 particles synthesized by egg-white at different magnifications. Various particle morphologies including octahedron, truncated octahedron, tetrahedron, flake like and spheroidal were observed. These morphologies makes proper average size estimation rather difficult, however, a broad distribution of particles with sizes ranging from 20 nm up to several micrometers are present. Very smooth surfaces of polyhedra and particles with flake morphology suggest a strong passivation of some crystalline faces by the protein matrix thus resulting in anisotropic growth due to the inhibition of growth in some crystal directions.

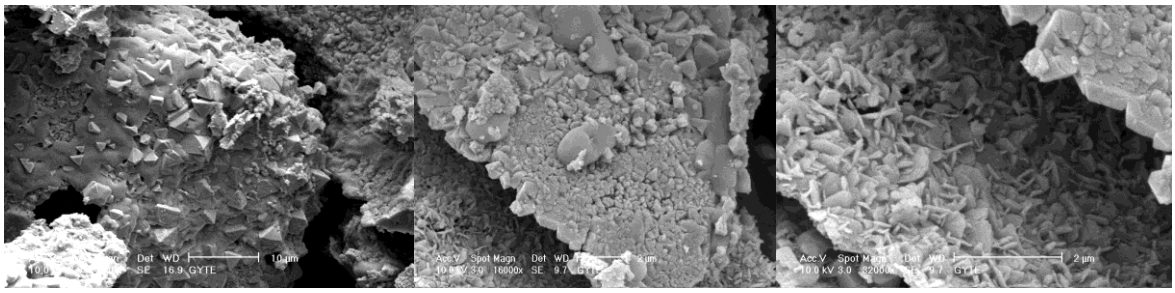

Figure 3.77 SEM micrographs of Co_3O_4 NPs powder at different magnifications obtained after calcination of the dried gel precursor at 800 ^oC for 3 h.

1.3.1.4 Thermal Analysis

Thermal stability of the precursor powder and final powder has been analyzed using TGA. Thermograms for both samples are presented in Fig. 3.78. Calcined powder shows no weight loss up to ~850 ^oC after which it looses about 5% weight. This could be due to very stable residual organometallic/organic compounds that decompose at such elevated temperatures. Precusor powder shows an overall weight loss of ~90%. According to the differential thermogram, DTG, there is four-step weight loss (indicated with arrows) for the precursor powder, of mainly ovalbumine, matrix the first one at < 200 ^oC, a shoulder at ~240 ^oC, the most intense one at ~300 ^oC and the last one at ~850 ^oC. The observed thermogram perfectly matches that of pure ovalbumin reported by Kumari et al. [140] above 200 ^oC. Weight loss up to 200 ^oC is due to the adsorbed water and boiling of organic residues released from Co salts. Weight loss around ~240 ^oC suggests that water molecules in albumin are

strongly bonded to the protein molecules and that it takes higher energies to remove them. The considerable weight loss at ~300 ^{o}C is due to the decomposition of protein matrix and the last one at ~850 ^{o}C is due to the decomposition of Co_3O_4 powder to CoO and oxygen gas [182].

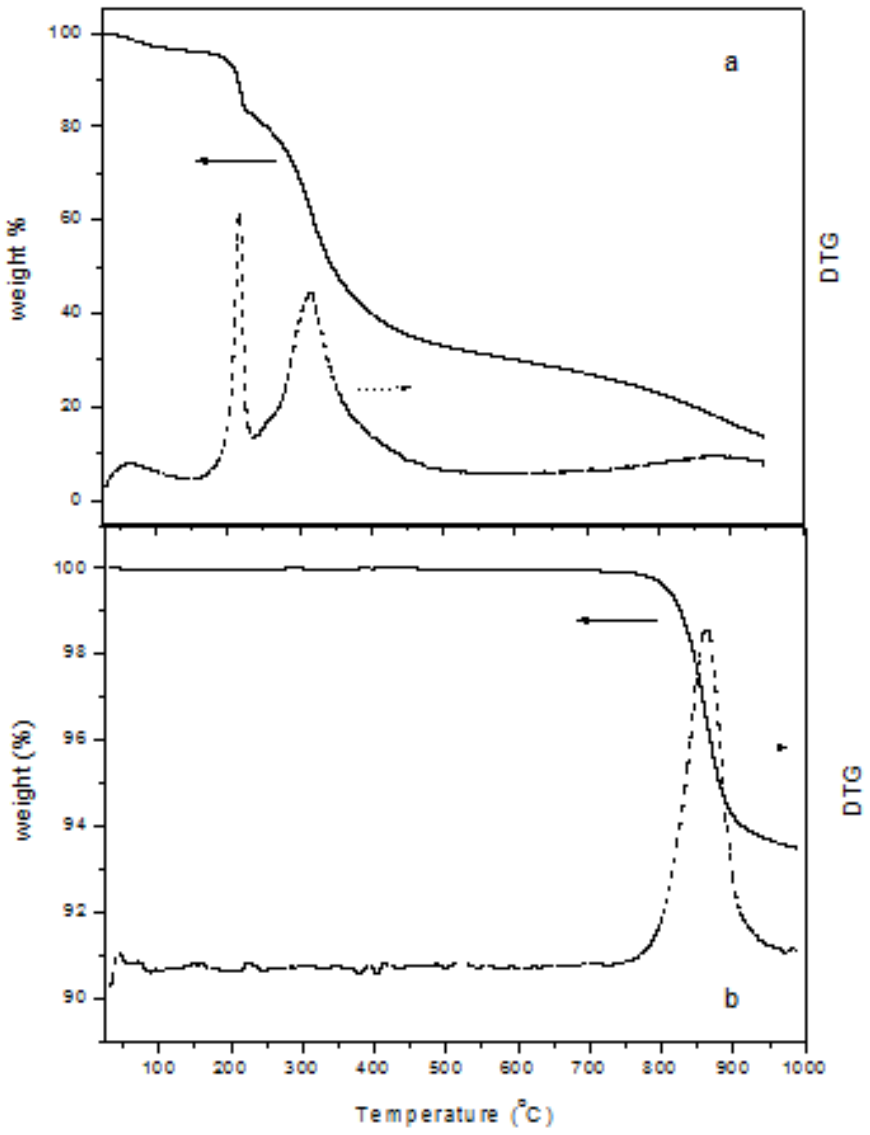

Figure 3.78 TGA thermograms and differential thermograms, DTG, of **(a)** as-made dried gel precursor; and **(b)** final powder after calcination of dried gel precursor at 800 ^{o}C for 3 h.

3.3.1.5 EPR Analysis

The room temperature EPR spectra of Co_3O_4 particles show a broad single signal with nonsymetric lineshape similar to those in study of Dutta et al. [184] in which the nano and bulk Co_3O_4 are compared. The EPR parameters; resonance field -H_{Res}, peak to peak line-

width -ΔH_{PP}, *g* factor and *A*/*B* ratio are obtained as 3185 G, 2160 G, 2.18 and 1.02 from Fig. 3.79 The *A*/*B* is the ratio of the height of the positive to the negative peak of the EPR resonance and is nearly unity, indicating that the spins are free electron type. The obtained EPR parameters and resonance Lorentzian line shape obtained by fitting are closer to the outputs of Co_3O_4 with 17 nm crystallite size reported by Dutta et al.[183]. Our results are also in good agreement with Venkateswara et al. [184] that reported linewidths of 3500 and 3350 Gauss (g values of 2.1678 and 2.3002) for Co_3O_4 NPs with 7-18 nm synthesized by urea-based combustion method.

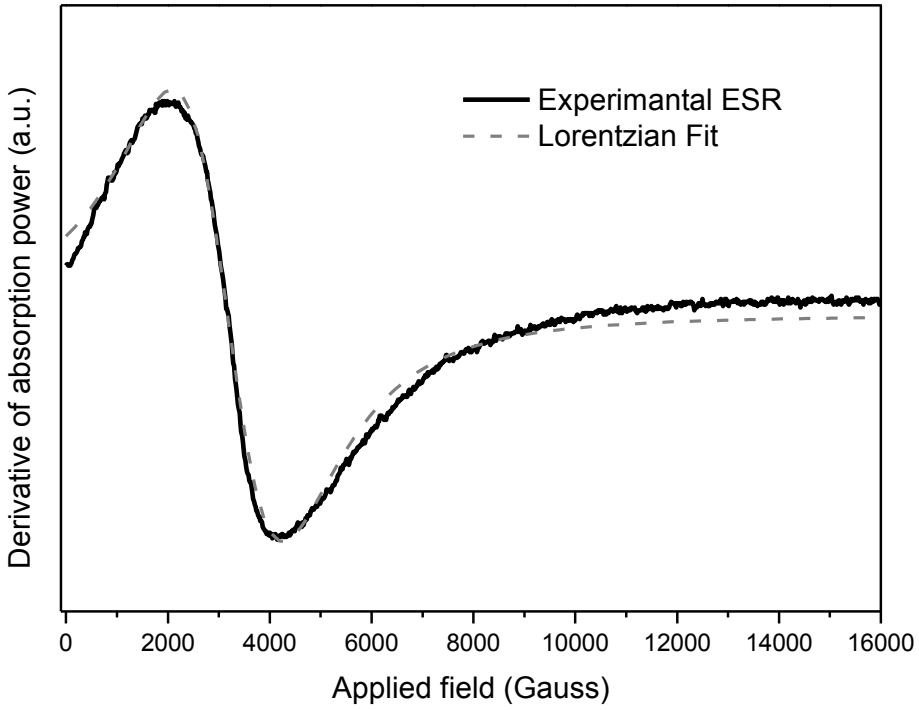

Figure 3.79 First derivative of EPR signal for Co_3O_4 NPs obtained upon calcination of the dried gel precursor at 800 ^oC.

3.3.2. Hydrothermal route with PVP

3.3.2.1 XRD Analysis

XRD analysis was performed on the obtained powder and revealed that the only phase observed was Co_3O_4 spinel oxide with ICDD card no of 42-1467. The mean size of the

crystallites was estimated from the powder diffraction pattern by performing line profile, shown in Fig.3.80, was fitted for 7 peaks (220), (311), (222), (400), (422), (511), (440) and the average crystallite size, *D* and σ, were estimated as 19 ± 4 nm.

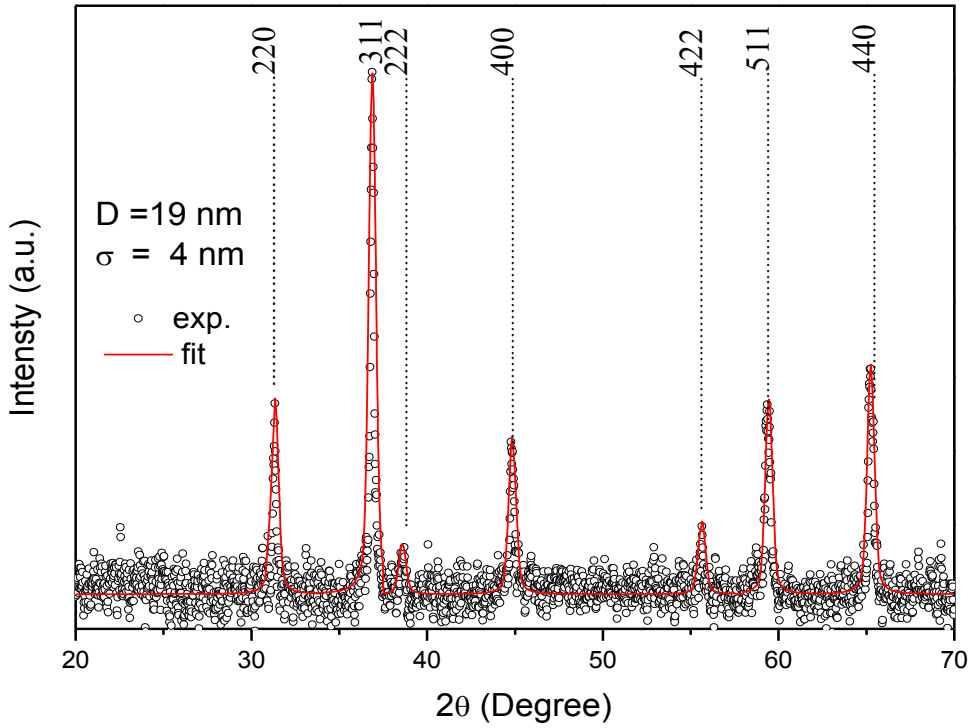

Figure 3.80 X-ray powder diffraction pattern (◌) and line profile fitting (solid line) for the PVP coated Co_3O_4 NPs.

3.3.2.2 FTIR Analysis

The band at 1661 cm-1 is attributed to the C=O stretching of pure PVP structure (Fig.3.81a) and its shift to lower wavenumbers (lower energies) should be due to the chemical interaction between the PVP molecules and Co_3O_4 NPs surface. This result represents a strong evidence that this interaction occurs through the C=O groups of PVP [137, 138]. The similar interaction was also observed between 2-pyrolidone and Co_3O_4 NP's [139] and L-Lysine and Fe_3O_4 NP's [116]. The broadness of the FTIR peak at around 3500 cm^{-1} also proves the existence of H-bonding among pyrrolidone molecules. In addition, FTIR spectra of the particles exhibit characteristic peaks of Co_3O_4 at around ν_1 = 666 cm^{-1} ν_2 = 572 cm^{-1} respectively [181,164,51].

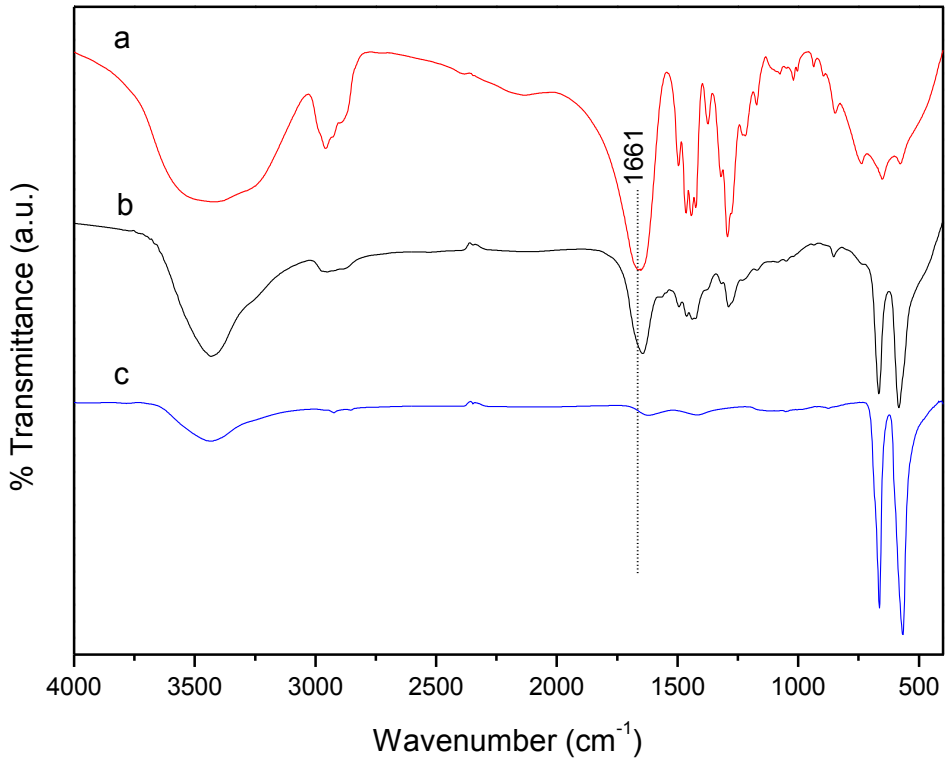

Figure 3.81 FTIR spectra of **a)** PVP, **b)** PVP coated Co_3O_4 NPs and **c)** pure Co_3O_4 NPs.

CHAPTER 4

CONCLUSION

In this study, we synthesized iron oxide NPs coated with L-lysine, in only one step by in situ formation of iron oxide NPs via a co-precipitation route in the presence of aminoacids as ligand. The presence of L-lysine on the surface of iron oxide NPs and the chemical nature of the bonds between the aminoacids and iron oxide were confirmed by FTIR and zeta potential analysis. Frequency (1Hz-3MHz) and temperature (290K-420K) dependant AC conductivity measurements resulted in AC activation energies between 0.048 - 0.041 eV for uncoated and 0.050 - 0.044 eV for LCIO NPs. The DC conductivity of sample increases with increasing temperature and the same follows simple hopping type conductivity. Temperature dependant DC resistivity measurements of iron oxide and LCIO at high temperatures resulted in the DC activation energies of 0.22 eV and 0.43 eV respectively. Besides magnetic transitions around 70 ^{o}C, the higher activation energy values for LCIO is the result of the insulating coating of L-lysine.

PVTri-Fe_3O_4 nanocomposites with conducting and magnetic characteristics were synthesized by wet chemical processes for the first time. PVTri has been synthesized in a separate process and was then coated/adsorbed on sonochemically synthesized magnetite NPs. Crystallite size was calculated for magnetite by x-ray line profile fitting as 12 ± 6 nm. FTIR and TGA analysis confirm the adsorption/coating of PVTri on magnetite NPs. SEM micrographs revealed that Fe_3O_4 NPs are slightly aggregated upon PVTri coating. Impedance and permittivity measurements revealed sharply reduced dielectric loss in these nanocomposites making these materials suitable candidates for applications as inductive and capacitive materials as well as microwave absorbers.

Mn_3O_4 NPs have been successfully synthesized by a novel method using an ionic liquid, [BMIM]OH at room temperature. The ionic liquid [BMIM]OH plays an important role on the reaction as the assisted agent and electric conductor media. This route could be considered as a novel, environmental friendly, fast and precise method to prepare nanostructured Mn_3O_4 and similar oxide systems. As-synthesized NPs were characterized

using FT-IR, XRD, and TEM techniques. Phase purity was confirmed by XRD and a crystallite size of 45 ± 11 nm was obtained by x-ray profile fitting. TEM analysis revealed various morphologies and particle sizes which clearly indicates the polycrystalline nature of observed NPs. Long-range interactions as indicated by the ESR measurements might be due to the wide range of particle sizes and morphologies observed.

To the best of our knowledge, this is the first report on the synthesis of Mn_3O_4 NPs by using only $Mn(CH_3COO)_2$ as the starting material. XRD analysis confirmed the structure as tetragonal hausmannite crystal structure model of Mn_3O_4. TEM images showed that spheroid Mn_3O_4 nanostructures obtained by this method have average particle size of 6 nm and 14 nm for NaOH and TMAOH hydrolyzed samples respectively. Particle size analysis indicated a strong aggregation and showed bimodal distribution with average radius of ~250 nm and 1.1 μm for both samples. FT-IR analyses confirm structures of Mn_3O_4 NPs as spinel oxide. Zeta potential analysis revealed adsorbed TMAOH species on the surface of Mn_3O_4 NPs hydrolyzed using TMAOH. ESR analyses resulted in broader lines and smaller g values than bulk Mn_3O_4 NPs, probably due to the exchange-coupled system with unlike spins such as canted spin at surface of high-surface-disordered NPs.

A novel, environment friendly route utilizing freshly extracted ovalbumin, and Mn^{2+} and Mn^{3+} salts, has been successfully used for the synthesis of Mn_3O_4 nanocrystals. High pH value of ovalbumin-water mixture self-regulated the pH for hydrolysis of metal ions. Water soluble ovalbumin proteins formed a gel and served as a matrix for entrapment of Mn^{2+} and Mn^{3+} ions. The dried gel precursors decomposed into nanocrystalline Mn_3O_4 upon calcinations. Crystallite size was estimated as 22±10 nm by XRD line profile fitting and particle size observed from SEM is in the range of 150 nm-2 μm. This discrepancy indicated polycrystalline nature of synthesized NPs. EPR analysis showed a narrow and symmetric line indicating the absence of hyperfine splitting. Presented synthetic route is simple, cost effective, cheap, and environmentally friendly that can be applied for the synthesis of other oxide systems.

Ultrasonically synthesized Mn_3O_4 (without using any base) was capped with PANI by in-situ polymerization successfully. This route is an alternative low temperature high yield process for bulk production of the title material. SEM analysis revealed nanosheet morphology with layer thickness of 2-3 nm. Results showed that PANI is succesfully coated on NPs surface and overall conductivity of nanocomposite is approximately 50 to 1000 times higher than that of uncapped Mn_3O_4 or PANI base with increasing temperature.

A novel, environment friendly route utilizing freshly extracted ovalbumin, and Co^{2+} and Co^{3+} salts, has been successfully used for the synthesis of Co_3O_4 nanocrystals. Ovalbumin-water mixture self-regulated the pH in the basic region for hydrolysis of metal ions, which did not require any additional base for hydrolysis. A gel formed where water soluble ovalbumin proteins served as a matrix for entrapment of Co^{2+} and Co^{3+} ions. Upon heat treatment, the dried gel precursors decompose into nanocrystalline Co_3O_4. A crystallite size of 45±8 nm was obtained by XRD line profile fitting and particle size estimated from the SEM is in the range 20 nm–2 μm. This reveals polycrystalline nature of synthesized particles. EPR analysis of Co_3O_4 shows a broad single signal with nonsymmetrical line shape. EPR results show a very good fit to literature reports for NPs in the size range of 8-17 nm. The ratio of the height of the positive to the negative peak of the EPR resonance and is nearly unity, indicating that the spins are free electron type. Even though the overall particle size distribution is quite wide magnetic measurements confirm nanocrystalline nature of the particles obtained. Presented synthetic route is simple, cost effective, and environmentally friendly that can be applied for the synthesis of various oxide systems.

REFERENCES

[1] R.P. Feynman, Eng. Sci. 23 (1960) 22.

[2] B. Bhushan, *Handbook of Nanotechnology*, edited, Springer, Berlin, 2004.

[3] R.J. Tackett *Multifunctional Magnetic Nanoparticles*, PhD Thesis, Wayne State University, 2008.

[4] E.K. Drexler, *Engines of Creation: The Coming Era of Nanotechnology*, Doubleday: New York, 1987.

[5] M. Wilson, *Nanotechnology: Basic Science and Emerging Technologies*, CRC Press, Boca Raton: Florida, 2002.

[6] E. Regis, M. Chimsky, *Nano: The Emerging Science of Nanotechnology*, Vol. 1. Boston, 1996.

[7] B.C. Crandall, J. Lewis, *Nanotechnology: Research and Perspectives*, MIT Press, Cambridge: Massachusetts, 1992.

[8] K.J. Klabunde, *Nanoscale Materials in Chemistry*, Wiley- Interscience, New York, 2001.

[9] A.J. Bard, *Integrated Chemical Systems: A Chemical Approach to Nanotechnology*. Wiley, New York, 1994.

[10] S. Kawata, *Nano-Optics*, Springer- Verlag, New York, 2002.

[11] M. Grundmann, *Nano-Optoelectronics: Concepts, Physics, and Devices*, Springer-Verlag, New York, 2002.

[12] H.S. Nalwa, *Handbook of Nanostructured Materials and Nanotechnology*, Academic Press, San Diego, 1999.

[13] S. Mitura, *Nanomaterials*, Elsevier Science, New York, 2000.

[14] H.S. Nalwa, *Nanostructured Materials and Nanotechnology*, Academic Press, San Diego, 2001.

[15] B. Bhushan, *Fundamentals of Tribology and Bridging the Gap between the Macro and Micro/Nanoscales*, Kluwer Academic, 2001.

[16] N.J. DiNardo, *Nanoscale Characterization of Surfaces and Interface,* VCH, Weinheim, 1994.

[17] Z.L. Wang, *Characterization of Nanophase Materials*, Wiley, New York, 2000.

[18] M.A. Reed and T. Lee, *Molecular Nanoelectronics,* American Science Publishers, Stevenson Ranch, California, 2003.

[19] R.A. Freitas, Jr., *Nanomedicine,* Landes Bioscience, 1999.

[20] D. Robinson, *Nanotechnology in Medicine and the Biosciences*, Gordon & Breach, 1996.

[21] M.C. Roco, W.S. Bainbridge, *Societal Implications of Nanoscience and Nanotechnology*, Kluwer Academic, 2002.

[22] L. Vayssieres, A. Manthiram, *Encylopedia of Nanoscience and Nanotecnology*, 8 (2004) 147.

[23] http://cohesion.rice.edu/centersandinst/cnst/cnst.cfm?doc_id=1209
Richard E. Smalley Institute

[24] http://www.fhi-berlin.mpg.de/~hermann/Balsac/BalsacPictures/PdC6H6CO.gif
Max Planck Institute

[25] T. Teranishi; M. Miyake, *Encylopedia of Nanoscience and Nanotecnology,* 5 (2004) 421.

[26] http://www.phys.uu.nl/~koole/ Rolf Koole, Ornstein Laboratorium.

[27] X. Feng, M.Z. Hu, *Encylopedia of Nanoscience and Nanotecnology* 1 (2004) 687.

[28] M.C. Roco, in *Nanostructured Materials; Vol. 3* (G. M. Chow and N. J. Noskova, Eds.), 3rd ed., 71–92. Kluwer Academic, Boston, 1998.

[29] E.L. Hu and D.T. Shaw, in *Nanostructure Science and Technology* (R. W. Siegel, E. Hu, and M. C. Roco, Eds.), 16–47. Kluwer Academic, Boston, 1999.

[30] http://www.chem.toronto.edu/staff/GAO/flashed/book.htm. University of Toronto.

[31] Y. Suyama, A. Kato, J. Am. Ceram. Soc. 59 (1976) 146.

[32] S. Morooka, T. Tasutake, A. Kobata, K. Ikemizu, Y. Kato, Int. Chem. Eng. 29 (1989) 119.

[33] H.D. Jang, J. Jeong, J.Aerosol Sci. Technol. 23 (1995) 553.

[34] M.L. Panchula, J.Y. Ying, Nanostruct. Mater. 9 (1997) 161.

[35] K. Kimura, in *Fine Particles: Synthesis, Characterization, and Mechanisms of Growth*, 92nd ed., 513–550. 2000.

[36] H. Schmidt, C. Lesniak, T. Schlestel, in *Fine Particles and Technology* (E. Pelizzetti, Ed.), 3rd ed., 623–642. Kluwer Academic, Boston, 1996.

[37] S.A. Bruno, E.I. Du Pont de Nemours and Company, USA, 1992.

[38] S. Mann, Nature 499 (1993) 365.

[39] L. Addadi, S. Weiner, Angew. Chem. , Int. Ed. Engl. 31 (1992) 153.

[40] R.J.P. Williams, Trans. R. Soc. Lond. B 304 (1984) 411.

[41] D.W. Johnson, Jr., in *Advances in Ceramics: Ceramic Powder Science*, 21, 3–19. American Ceramic Society, 1987.

[42] A. Goossens, J. Schoonman, Eur. J. Solid State Inorg. Chem. 32 (1995) 779.

[43] H.J. Arpe, *Silicon Compounds, Inorganic to Stains, Microscopic*, Vol. A24 (B. Elvers, Ed.). VCH, New York, 1993.

[44] F. Iskandar, *Encylopedia of Nanoscience and Nanotecnology* 8 (2004) 262.

[45] M.A. Willard, L.K. Kurihara, E.E. Carpenter, S. Calvin, V.G. Harris, *Encylopedia of Nanoscience and Nanotecnology* 1 (2004) 820.

[46] R. Massart, Compt. Rend. Series C 1 (1980) 291.

[47] F. A. Tourinho, R. Franck, R. Massart, J. Mater. Sci. 25 (1990) 3249.

[48] F. Tourinho, R. Franck, R. Massart, R. Perzynski, Prog. Colloid Polym. Sci. 79 (1989) 128.

[49] E. Auzans, D. Zins, E. Blums, R. Massart, J. Mater. Sci. 34 (1999) 1253.

[50] D. Zins, V. Cabuil, R. Massart, J. Mol. Liq. 83 (1999) 217.

[51] T. Ozkaya, *Synthesis and Characterization of M_3O_4 (M: Fe, Mn, Co) Magnetic Nanoparticles*, Master Thesis, Fatih Univ. Istanbul-Turkey, 2008.

[52] W.J. Dawson, Am. Ceram. Soc. Bull. 67 (1988) 1673.

[53] D.Chen, X.Jiao, J. Am. Ceram. Soc. 83 (2000) 2637.

[54] S. Komarneni, Q. H. Li, R. Roy, J.Mater. Chem. 4 (1994) 1903.

[55] A. Baykal, N. Kasapoğlu, Y. Köseoğlu, A.C. Başaran, H. Kavas, M.S. Toprak Cent. Eur. J. Chem. 6 (2008) 125.

[56] J.A.L. Pérez, M.A.L. Quintela, J. Mira, J. Rivas, and S.W. Charles, J. Phys. Chem. B 101 (1997) 8045.

[57] J. Fang, J. Wang, L.M. Gan, S.C. Ng, J. Ding, X. Liu, J. Am. Ceram. Soc. 83 (2000) 1049.

[58] K.S. Suslickand, G. J. Price, Ann. Rev. Mater. 29 (1999) 295.

[59] A. Askarinejad, A. Morsali, Ultrason. Sonochem. (2008) doi:10.1016/j.ultsonch.2008.05.015

[60] M.T. Reetz, W. Helbig, S.A. Quaiser, in *Active Metals*, (A. Fürstner, Ed.), p. 279. VCH, Weinheim, 1996.

[61] M.T. Reetz, W. Helbig, S. Quaiser, U.S. Patents, 5, 620, 564, 1997, and 5, 925, 463, 1999.

[62] M.A. Winter, Ph.D. Thesis, Verlag Mainz, Aachen, 1998.

[63] N.Poudyal, Synthesis And Characterization of Magnetic Nanoparticles, Master Thesis, The Universty of Texas At Arlington, 2005.

[64] J.I. Taylor, C.D. Hurst, C.D. M.J. Davies, M.J.N. Sachsinger, I.J. Bruce, Journal of Chromatography A 890 (2000) 159.

[65] S. Mornet, A. Vekris, J. Bonnet, E. Duguet, F. Grasset, J.H. Choy, J. Portier, Materials Letters 42 (2000) 183.

[66] G.A. Johnson, G.P Cofer, S.L. Gewalt, L.W. Hedlund, Magn Reson Q 9 (1993) 1.

[67] C.C. Berry, A.S.G. Curtis, J. Phys. D: Appl. Phys. 36 (2003) R198.

[68] Z. Mohammadi, *In Situ Synthesis of Iron Oxide within Polyvinylamine Nanoparticles*, Master Thesis, University of Kansas, 2008.

[69] H. Otsuka, Y. Nagasaki, K. Kataoka, Advanced Drug Delivery Reviews 55 (2003) 403.

[70] A. Chilkoti, M.R. Dreher, D.E. Meyer, Advanced Drug Delivery Reviews, 54 (2002) 1093.

[71] C.Chouly, D. Pouliquen, I. Lucet, J. J. Jeune, P. Jallet, Journal of Microencapsulation, 13 (1996) 245.

[72] J.Chatterjee, Y. Haik, C.J. Chen, Journal of Magnetism and Magnetic Materials, 257 (2003) 113.

[73] http://en.wikipedia.org/wiki/Magnetic_resonance_imaging.

[74] D.G. Mitchell, M.S. Cohen, *MRI principles* W.B. Saunders Company, 1998.

[75] C. Sun, O. Veiseh, D. Lee, N. Bhattarai, J. Gunn, C. Fang, R. Ellenbogen, J. Olson, M. Zhang, Small 4 (2008) 372.

[76] C.A. Ross, Annual Review of Material Research, 31 (2001) 203.

[77] S. Okamoto, O. Kitkami, N. Kickuchi, T. Miyazaki, Y. Shimada, Physical Review B 67 (2003) 094422.

[78] Y. Shi, J. Ding H. Yin, Journal of Alloys and Compounds 303 (2002) 290.

[79] Y. Kim, D. Kim, C. S. Lee, Physica B 337 (2003) 42.

[80] C.N. Chinnasamy, M. Senoue, B. Jeyadevan, O. P. Perez, K. Shinoda, K. Tohji, Journal of colloid and interface Science 263 (2003) 80.

[81] H. Zeng, J. Li, J.P. Liu, Z.L. Wang, S. Sun, Nature, 420 (2002) 395.

[82] H. Zeng, S. Sun, J. Li, Z.L. Wang, J.P. Liu, Applied Physics Letters 85 (2004) 792.

[83] http://www.carolina.com/physics/aboutferro.asp

[84] M.A. Willard, L.K. Kulrihara, E.E. Carpenter, S. Calvin, V.G. Harris, International Material Reviews 49 (2004) 125.

[85] http://www.zarm.uni-bremen.de/2forschung/ferro/basic_info/applic/index.htm. Zarm Center of Applied Space Technology.

[86] S.H. Gee, Y.K. Hong, D.W. Erickson, M.H. Park, J.C. Sur, Journal of Applied Physics 93 (2003) 7560.

[87] http://www.msm.cam.ac.uk/doitpoms/tlplib/ferromagnetic/printall.php, University of Cambrige.

[88] K.G. Ong, C.A. Grimes, *Encylopedia of Nanoscience and Nanotecnology* 5 (2004) 9.

[89] J. Mathon, J. Phys. C: Solid State Phys**.** 2 (1969) 1647.

[90] http://www.ruf.rice.edu/~natelson/research.html. Douglas Natelson Assoc. Prof.

[91] a) http://commons.wikimedia.org/wiki/File:Spinel.GIF b) N. Kasapoglu, *Synthesis, Characterization and ESR Studies of Magnetic Spinel Compounds*, Master Thesis, Fatih University, 2007.

[92] T. Wejrzanowski, R. Pielaszek, A. Opalińska, H. Matysiak, W. Lojkowski, K.J. Kurzydlowski, Appl. Surf. Sci. 253 (2006) 204.

[93] R. Pielaszek, *Appl. Crystallography Proceedings of the XIX Conference*, 43 Krakow, Poland, 2003.

[94] B.C. Ranu, S. Banerjee, Organic Letters 7 (2005) 3049.

[95] S. Wei, Y. Zhu, Y. Zhang, J. Xu, Reactive and Functional Polymers 66 (2007) 1272.

[96] R.A. Nyquist, R.O. Kagel, *Infrared Spectra of Inorg.Comp.* New York, Academic Press, 1971.

[97] N. Hanh, O.K. Quy, N.P. Thuy, L.D. Tung, L. Spinu, Physica B 327 (2003) 382.

[98] L.J. Kirwan, P.D. Fawell, W.V. Bronswijk, Langmuir 19 (2003) 5802.

[99] M. Nara, H. Torii, M. Tasumi, J. Phys. Chem. 100 (1996) 19812.

[100] J.Y. Park, E.S. Choi, M.J. Baek, G.H. Lee, Materials Letters 63 (2009) 379.

[101] J.A. Kieft, K. Nakamoto, J. Inorg. Nucl. Chem. 29 (1967) 2561.

[102] S. Dutta, S.K. Manik, M. Pal, S.K. Pradhan, C.P.D. Brahma, J. Magn. Magn. Mater. 288 (2005) 301.

[103] H. Watanabe, N. Tsuya, *Science reports of the Research Institutes*, Tohoku University. Ser. A, Physics, Chemistry and Metallurgy 2 (1950) 29.

[104] N.F. Mott, E.A. Davis, *Electronic Processes in Non-crystalline Material*, Oxford Press, London 1979.

[105] S.S. Ata-Allah, M. Kaiser, Journal of Alloys and Compounds doi:10.1016/j.jallcom.2008.03.117

[106] S. Mahalakshmi, K.S. Manja, Journal of Alloys and Compounds 457 (2008) 522.

[107] S. Ghataka, M. Sinhab, A.K. Meikapa, S.K. Pradhan, Physica E 40 (2008) 2686.

[108] Y.T. Tao, J. Am. Chem. Soc. 115 (1993) 4350.

[109] S.J. Ahn, D.H. Son, K Kim, J. Mol. Struct. 324 (1994) 223.

[110] G. Kataby, M. Cojocaru, R. Prozorov, A. Gedanken, Langmuir 15 (1999) 1703.

[111] L. Zhang, R. He, H. Gu, Applied Surface Sci. 253 (2006) 2611.

[112] K.V.P.M. Shafi, A.Ulman, X.X.Yan, N.Ynag, C.Estournes, H.White, M.Rafailovich, Langmuir 17 (2001) 5093.

[113] M. Kartal, S.K. Kayahan, A. Bozkurt, L. Toppare, Talanta 77 (2008) 659.

[114] S.Ü.Çelik, A.Aslan, A.Bozkurt, Solid State Ionics 179 (2008) 683.

[115] M. Takafuji, S. Ide, H. Ihara, Z. Xu, Chem. Mater. 16 (2004) 1977.

[116] Z. Durmus, H. Kavas, M.S. Toprak, A. Baykal, T.G. Altıncekic¸ A. Aslan, A. Bozkurt, S. Cosgun, J. Alloys Compd. (2009) doi:10.1016/j.jallcom.2009.04.103.

[117] A.M.M. Farea, S. Kumar, K.M. Batoo, J. Alloys Compd. 464 (2008) 361.

[118] J.C. Maxwell, *Electric and Magnetism*, Oxford University Press, NewYork, 1973.

[119] I.H. Gul, A.Z. Abbasi, F. Amin, M. Anis-ur-Rehman, A. Maqsood, J. Magn. Magn. Mater. 311 (2007) 494.

[120] G.C. Psarras, Composites A 37 (2006) 1545.

[121] E.J.W. Verway, P.W. Haayman, Physica 8 (1941) 979.

[122] C.V. Chanmal, J.P. Jog, Express Polymer Letters 2 (2008) 294.

[123] V.L. Kozhevnikov, I.A. Leonidov, M.V. Patrakeev, E.B. Mitberg, Journal of Solid State Chemistry 158 (2000) 320.

[124] A.M. Abdeen, O.M. Hemedaa, E.E. Assemb, M.M. El-Sehly, Journal of Magn. and Magn. Mater. 238 (2002) 75. [125] D. Zou, C. Xu, H. Luo, L. Wang,, T. Ying Materials Letters 62 (2008) 1976.

[126] W. Wang, C. Xu, G. Wang, Y. Liu, C. Zheng, Adv Mater. 14 (2002) 840.

[127] N. Gupta, A. Verna, S.C. Kashyap, D.C. Dube, J. Magn. Magn. Mater. 308 (2007) 342.

[128] E. Winkler, R.D. Zysler, D. Fiorani, Physical Review B 70 (2004) 174406.

[129] T. Ozkaya, A. Baykal, H. Kavas, Y. Koseoglu, M.S. Toprak, Physica B 403 (2008) 3764.

[130] S.K. Tripathy, M. Christy, N. Park, E. Suh, S. Anand, Y. Yu, Materials Letters 62 (2008) 1006.

[131] W. Wang, C. Xu, G. Wang, Y. Liu, C. Zheng, Adv. Mater. 14 (2002) 837.

[132] M. Ishii, M. Nakahira, Solid State Commun. 11 (1972) 209.

[133] Z. Weixin, W. Cheng, Z. Xiaoming, X. Yi, Q. Yitai, Solid State Ionics 117 (1999) 331.

[134] J.M. Boyero, E.L. Fernández, J.M. Gallardo-Amores, R.C. Ruano, V.E. Sánchez, E.B. Pérez, Int. J. Inorg. Mater. 3 (2001) 889.

[135] T. Morimoto, H. Nakahata, S. Kittaka, Bulletin of the Chemical Society of Japan 51 (1978) 3387.

[136] B. Baroli, M.G. Ennas, F. Loffredo, M. Isola, R. Pinna, M.A. Lo´pez-Quintela, Journal of Investigative Dermatolo*gy* 127 (2007) 1701.

[137] G.G. Couto, J.J. Klein, W.H. Schreiner, D.H. Mosca, A.J.A. Oliveira, A.J.G. Zarbin, Journal of Colloid and Interface Science 311 (2007) 461.

[138] Z.J. Zhang, X.Y. Chen, B.N. Wang, C.W. Shi, Journal of Crystal Growth, 310 (2008) 5453.

[139] T. Özkaya, A. Baykal, M.S. Toprak, Cent. Eur. J. Chem. 6 (2008) 465.

[140] T. Sri Devi Kumari, R. Kannan, T.P. Kumar, Ceramic International, doi:10.1016/j.ceramint.2008.08.020.

[141] W.S. Kijlstra, E.K. Poels, A. Bliek, B.M. Weckhuysen, R.A. Schoonheydt, J. Phys. Chem. B 101 (1997) 309.

[142] G. Srinivasan, M.S. Seehra, Phys. Rev. B 28 (1983) 1.

[143] D.L. Huber, Phys. Rev. B 12 (1975) 31.

[144] K.M.S. Khalil, App. Surface Science 255 (2008) 2874.

[145] Z.M. Sui, X. Chen, L.Y. Wang, L.M. Xu, W.C. Zhuang, Y.C. Chai, C.J. Yang, Physica E 33 (2006) 308.

[146] X.Du, W. Miao, Y. Liang, J. Phys. Chem. B 109 (2005) 7428.

[147] a) X. Ma, F.Xu, L. Chen, Z. Zhang, Y. Du, Y. Xie, Journal of Crytsal Growth 280 (2005) 118. b) Z.M. Sui, X.Chen, L.Y. Wang, L.M. Xu, W.C. Zhuang, Y.C. Chai, C.J. Yang, Physica E 33 (2008) 308.

[148] R.H. Terrill, J. Am. Chem. Soc. 117 (1995) 12537.

[149] P.J. Kreke, Langmuir 12 (1996) 699.

[150] Z.M. Sui, X. Chen, L.Y. Wang, L.M. Xu, W.C. Zhuang, Y.C. Chai, C.J. Yang, Physica E 33 (2006) 308.

[151] Srinivasan G, M.S. Seehra, Physical review B (condensed matter), 28 (1983) 1.

[152] R. Tackett, G.Lawes, B.C. Melot, M. Grossman, E.S. Toberer. R. Seshadri, Phys. Rev. B 76 (2007) 024409.

[153] A.H. Gemeay, R.G. El-Sharkawy, I.A. Mansour, A.B. Zaki, Journal of Colloid and Interface Science 308 (2007) 385.

[154] W. Wang, C. Xu, G. Wang, Y. Liu, C. Zheng, Adv. Mater. 14 (2002) 837.

[155] N. Gupta, A. Verna, S.C. Kashyap, D.C. Dube, J. Magn. Magn. Mater. 308 (2007) 137.

[156] X. Li , G. Wang, Materials Chemistry and Physics 102 (2007) 140.

[157] H. Qiu, M. Wan, J. Polym. Science Part A, Polym. Chem. 39 (2001) 3485.

[158] Y. He, X. Yu, Mater. Lett. 61 (2007) 2071.

[159] K.C. Chang, G.W. Jang, C.W. Peng, C.Y. Lin, J.C. Shieh, J.M. Yeh, Electrochim. Acta 52 (2007) 5191.

[160] X. Li, X. Li, G. Wang, Mater. Chem. Phys. 102 (2007) 140.

[161] J. Jianga, L.H. Ai, D.B. Qin, H. Liu, L.C. Li. Synthetic Metals 159 (2009) 695.

[162] S. Quillard, G. Louarn, S. Lefrant, A.G. Mac Diarmid, Phys. Rev. B 50 (1994) 12496.

[163] W.Zhao, X. Song, Z. Yin, C. Fan, G. Chen, S. Sun, Mater. Res. Bull. (2008) doi:10.1016/j.materresbull.2007.11.013.

[164] T.Ozkaya, A. Baykal, M.S. Toprak, Y. Koseoğlu, Z. Durmuş, J. Magn. Magn. Mater. 321 (2009) 2145.

[165] A.L. Pan, R.C. Yu, S.S.Xie, Z.B.Zhang, C.Q. Jin, B.S. Zhou, J. Cryst. Growth 282 (2005) 165.

[166] S.R. Elliott, Adv. Phys. 36 (1987) 135.

[167] J. Stejskal, R. G. Gilbert, Pure Appl. Chem. 74 (2002) 857.

[168] N.V. Blinova, J. Stejskal, M. Trchová, J. Prokeš, Polymer International 57 (2008) 66.

[169] D. Zhang, Polymer Testing 26 (2007) 9.

[170] J. Huang, R.B. Kaner, J. Am. Chem. Soc. 126 (2004) 51.

[171] W. Li, H.L. Wang, J. Am. Chem. Soc. 126 (2004) 2278.

[172] A.M.M. Farea, S. Kumar, K.M. Batoo, Journal of Alloys and Compounds 464 (2008) 361.

[173] R. Skomski, *Simple Models of Magnetism*, NewYork, Oxford University Press 2008.

[174] I.H. Gul, A.Z. Abbasi, F. Amin, M. Anis-ur-Rehman, A. Maqsood, J. Magn. Magn. Mater. 311 (2007) 494.

[175] B. Ramesh, D. Ravinder, Materials Letters 62 (2008) 2043.

[176] Y. Fukuda, S. Nagatab, K. Echizenya, J. Magn. Magn. Mater. 279 (2004) 325.

[177] V.L.G. Uitert, Proc. IRE 44 (1956) 1294.

[178] R.K. Puri, V. Sayen, Proc. ICF-5, India (1989) 245.

[179] K.M. Batoo, S. Kumar, C.G. Lee, Current Applied Physics 9 (2009) 1397.

[180] F. Kurtulus, H. Güler, Inorg. Mat. 41 (2005) 5564.

[181] T. Ozkaya, A. Baykal, Y. Koseoğlu, H. Kavas, Cent. Eur. J. Chem. 7 (2009) 410.

[182] A. Malecki, J. Tareen, J. Doumerc, L. Rabardel, J. Launay, J. of Solid State Chem. (1985) 49.

[183] P. Dutta, M.S. Seehra, S. Thota and J. Kumar J. Phys: Condens. Matter 20 (2008) 015218.

[184] K. V. Rao, C.S. Sunandana, Solid State Communications 148 (2008) 32.